AN EXPLORATORY EXPERIMENTAL AND ANALYTICAL STUDY OF SEPARATING TWO PARALLEL LIFTING STAGES OF A REUSABLE LAUNCH VEHICLE AT MACH NUMBERS OF 3 AND 6

A Thesis

Presented to

the Faculty of the School of Engineering and Applied Science

Univeristy of Virginia

In Partial Fulfillment

of the Requirements for the Degree

Master of Aerospace Engineering

---

by

John P. Decker

May 1968

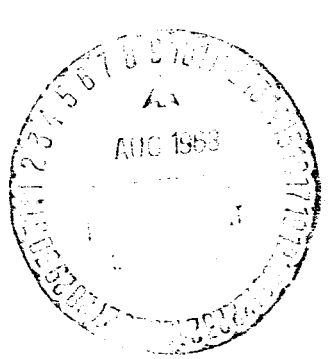

APPROVAL SHEET

This thesis is submitted in partial fulfillment of

the requirements for the degree of

Master of Aerospace Engineering

_____

Author

Approved:

_____

Faculty Adviser

_____

Dean, School of Engineering and
Applied Science

May 1968

ACKNOWLEDGMENTS

The author is indebted to the National Aeronautics and Space Administration for permission to use material obtained from a research project at the Langley Research Center in this thesis. Particular thanks are due Mr. P. Kenneth Pierpont for his guidance during the investigation and to Mr. Joseph Gera who wrote the computer program to study the motion of the vehicles during a staging maneuver.

The author is also grateful to Dr. George B. Matthews for his comments and suggestions in preparing this thesis.

TABLE OF CONTENTS

LIST OF TABLES

LIST OF FIGURES

FIGURE PAGE

FIGURE PAGE

LIST OF SYMBOLS

A	planform area of pitch controls, ft^2
c	reference length (see Table I); for the first stage it is equal to the mean aerodynamic chord, for the second stage it denotes the body length, ft
C_A	axial-force coefficient, $\frac{\text{Measured axial force}}{\frac{k}{2} p_s M^2 S}$
C_m	pitching-moment coefficient, $\frac{\text{Measured pitching moment}}{\frac{k}{2} p_s M^2 Sc}$
C_N	normal-force coefficient, $\frac{\text{Measured normal force}}{\frac{k}{2} p_s M^2 S}$
C_{m_q}	damping in pitch, $\frac{\partial C_m}{\partial\left(\frac{qc}{2V}\right)}$
$C_{m_{\dot{w}}}$	rate of change of pitching-moment coefficient due to acceleration along Z-axis, $\frac{\partial C_m}{\partial \dot{w}}$, $(sec)^2/ft$
C_{N_q}	rotary stability derivative, $\frac{\partial C_N}{\partial\left(\frac{qc}{2V}\right)}$
C_{N_α}	normal-force slope, $\frac{\partial C_N}{\partial \alpha}$, per deg
C_T	thrust coefficient, $\frac{\text{Thrust force}}{\frac{k}{2} p_s M^2 S}$
d	distance between the centers of mass, ft

d_T	perpendicular distance from center of mass to the line of thrust, ft
F	resultant force, $(F_x^2 + F_y^2 + F_z^2)^{1/2}$, lb
F_x, F_y, F_z	components of resultant force along X, Y, Z axes, lb
F'	resultant aerodynamic force, $(F_x'^2 + F_y'^2 + F_z'^2)^{1/2}$, lb
F_x', F_y', F_z'	components of resultant aerodynamic force along X, Y, Z axes, lb
g	acceleration due to gravity, ft/sec^2
G	resultant external moment, $(M_x^2 + M_y^2 + M_z^2)^{1/2}$, ft-lb
h	altitude, $h = -z'$, ft
H	resultant angular momentum, $(H_x^2 + H_y^2 + H_z^2)^{1/2}$, slug-ft^2/sec
H_x, H_y, H_z	components of the resultant angular momentum about the X, Y, Z axes, slug-ft^2/sec
i	incidence angle, $i = \alpha_2 - \alpha_1$, deg
$\bar{i}, \bar{j}, \bar{k}$	unit coordinate vectors
I_{xx}, I_{yy}, I_{zz}	mass moments of inertia about X, Y, Z axes, slug-ft^2
I_{xy}	product of inertia, $\int xy\, dm$, slug-ft^2
I_{xz}	product of inertia, $\int xz\, dm$, slug-ft^2
I_{yz}	product of inertia, $\int yz\, dm$, slug-ft^2
k	ratio of specific heats
l	body length, ft

m	mass, slugs
M	Mach number
M_x, M_y, M_z	components of resultant moment about X, Y, Z axes, ft-lb
p, q, r	components of resultant angular velocity about X, Y, Z axes, rad/sec
p_s	static pressure, lb/ft^2
s	distance from the moment reference center to an element of mass, $(x^2 + y^2 + z^2)^{1/2}$, ft
S	reference area (see Table I), ft^2
t	time, sec
u, v, w	components of the resultant velocity along body axes, ft/sec
V	resultant velocity of an element of mass, ft/sec
V_c	resultant velocity, $(u^2 + v^2 + w^2)^{1/2}$, ft/sec
W	weight, lb
x, y, z	coordinate along body axes, ft
x', y', z'	coordinate along earth-fixed axes, ft
α	angle of attack, deg
γ	flight-path angle, $\gamma = \theta - \alpha$, deg
δ_e	resultant pitch control deflection (positive when trailing edge is down) $\frac{(\delta_e \text{right} + \delta_e \text{left})}{2}$
ϵ	angle between X-axis and thrust line, deg
ρ	atmospheric density, $slugs/ft^3$
ψ, θ, ϕ	angles of yaw, pitch, and roll, respectively, deg

ω	resultant angular velocity, $(p^2 + q^2 + r^2)^{1/2}$, rad/sec
Δt	time increment, sec
$\Delta x, \Delta z$	separation variables (positive when center of gravity of second stage is ahead and above center of gravity of first stage), ft
$\dot{}$ (dot)	denotes first derivative with respect to time
$\bar{}$ (bar)	denotes a vector

The subscripts "1" and "2" indicate whether the physical quantity represented by the principal symbol refers to stage 1 or stage 2.

ABSTRACT

An exploratory study has been made of the stage separation of parallel staged reusable launch vehicles. Static longitudinal aerodynamic data were obtained for both stages of a representative two-stage rocket-powered reusable launch vehicle concept when the stages were in close proximity to each other. The effects of vertical spacing, longitudinal spacing, and incidence angle were determined at Mach numbers of 3 and 6. Using the wind-tunnel data together with estimates of the dynamic derivatives obtained for similar type vehicles and also the vehicle and initial trajectory input data, the implication of the interferences on the individual vehicle dynamics was obtained at Mach numbers of 3 and 6 by numerically integrating the equations of motion for both vehicle stages.

CHAPTER I

INTRODUCTION

During the past several years, interest in the potential of the recovery and reuse of launch vehicles has resulted in a number of studies of various types of recoverable systems. The spectrum of concepts has varied from recoverable ballistic to winged reusable air-breathing vehicles. The latter type and most of those which employ aerodynamic lift during the ascent trajectory would probably utilize multiple stages which are arranged in parallel for launch. If staging must occur within the sensible atmosphere, aerodynamic interferences between the two vehicles may result in significant effects on the behavior of each vehicle during the staging maneuver. The author has therefore undertaken an exploratory investigation to ascertain these interferences and to interpret their influence on the staging maneuver. The present paper is an initial attempt at exploring the complex problem of separating parallel arranged stages of a reusable launch vehicle system.

In order to provide meaningful information on the magnitude and character of the staging problem it is necessary to obtain aerodynamic test data on each of the two vehicles at conditions which might occur during staging and then to estimate the effects of these forces and moments on the relative motion of the two vehicles. For the present investigation, which is primarily exploratory, static longitudinal data were obtained on two representative stages of a reusable launch vehicle system for a range of vehicle positions and attitudes to obtain some

understanding of the aerodynamic interference phenomena. These data were then used in numerically integrating the equations of motion of both vehicles to determine the relative behavior of both stages during a staging maneuver.

The experimental aerodynamic data were obtained for a model of a representative rocket-powered two-stage launch vehicle system. The first stage was a simplified wind-body configuration combination, whereas the second stage was a lifting body. The measured data consisted of static longitudinal aerodynamic forces and moments which were obtained simultaneously for each stage with strain-gage balances mounted on separate stings. Vertical and longitudinal spacing, as well as incidence angle, were varied for a range of angles of attack at Mach numbers of 3 and 6. The test results are used to illustrate the effect of these variables on the longitudinal stability of the two stages when in close proximity to each other.

The analysis of the staging maneuver was made using the coupled linearized longitudinal equations of motion for both stages in order to calculate their relative behavior and the influence of aerodynamic interference. In these equations the general load terms were replaced by the experimental aerodynamic data and by estimates of the damping derivatives obtained for similar type vehicles at interference-free conditions. For selected values of stage characteristics and initial conditions the equations were solved numerically. Typical results are presented to show some of the effects of vehicle parameters as they influence the safe separation or collision of the two stages.

CHAPTER II

APPARATUS AND TESTS

Tunnel

The wind-tunnel investigation was conducted in the 2-foot hypersonic facility at the National Aeronautics and Space Administration's Langley Research Center. The 2-foot hypersonic facility, described in reference 1, is a continuous, closed-circuit ejector type wind tunnel. The tunnel has a 24-inch by 24-inch by 54-inch test section and provides for testing in the Mach number range of 3 to 6 at approximate Reynolds numbers between 2.0×10^6 and 0.5×10^6. The air supply for the tunnel is obtained from two 100,000 CFM compressors connected in parallel and operated at a pressure ratio of 4, and a 10,000 CFM auxiliary compressor feeding the main nozzle of the tunnel. The stagnation temperature of the tunnel is controlled by a 1,000-horsepower nichrome-tube-type heater located just upstream of the nozzle. A schematic drawing of the main test section is presented in Figure 1. The two-dimensional nozzle, diffuser, and ejector are individually supported on screw jacks and can be moved in the vertical direction. Thus, adjustments are available to set the desired tunnel conditions by proper positioning of the various tunnel components. A silica gel drying system is located in the circuit to monitor the flow into the test section at a dewpoint of -15° F or less, which is adequate to insure no moisture condensation shocks which would adversely affect the consistency of the test results.

Models

Details of the launch vehicle configuration selected for the present study are shown in Figure 2. The launch vehicle consisted of a simplified wing-body first stage with a lifting-body second stage. The second stage was placed on top of the first stage, with the flat bottom parallel with the first-stage wing upper surface. The longitudinal location of the second stage was such that its moment reference center was behind the first-stage moment reference center in the normal carrying position, that is, $\frac{\Delta x}{l_1} = -0.051$. Photographs of the two-stage system prior to staging and at staging conditions are shown in Figure 3.

The first stage consisted of a semicylindrical fuselage with an ogival forebody and delta wing. The wing had 65° leading-edge sweep while the airfoil section was a half-diamond section that had a maximum thickness of 4 percent of the local chord at the 40-percent chord station. The wing was flat on the upper surface, thereby giving the wing negative camber. No longitudinal or vertical control surfaces were provided on first stage for the present tests.

The second-stage vehicle was a lifting body with cross-sectional shape progressions along the X-axis shown in Figure 2c. The second stage had essentially a flat bottom and was provided with vertical stabilizing surfaces. Pitch controls were provided on the second stage which consisted of upper and lower surface flaps located near the base of the body (see Fig. 2c). The ratio of the planform area of the pitch controls to the total planform area was 0.113 for the upper surface controls and 0.187 for the lower surface controls.

Support Mechanism

Separate sting supports were provided for the first and second stage, with the vertical movement between the stages being provided by the support system to which the stings were attached (see Fig. 4). Longitudinal movement and incidence angle between the stages were provided using spacers and sting adapters on the upper sting support. The complete support apparatus was attached to an arc strut which varied the angle of attack of the vehicles.

Tests

The wind-tunnel tests were conducted at nominal Mach numbers of 3.0 and 6.0. Position variables Δx and Δz, as well as the relative incidence angle, i, were varied for an angle-of-attack range of approximately -9° to 12° (see Fig. 5). The geometric variables Δx, Δz, and i were systematically varied to obtain the aerodynamic data needed as input to the two-body trajectory simulation computer program.

Static aerodynamic force and moment data were simultaneously obtained for the first and second stages by use of individual internal six-component strain-gage balances. No composite configurations, that is, with the first stage and second stage connected, were tested.

All data were obtained with the model smooth; that is, no boundary-layer transition strips were used. At the Reynolds numbers of these tests laminar flow may be expected to exist over almost the entire length of the models. Individual vehicle angles of attack were corrected for balance and sting deflection under load. No base drag corrections were

made for either stage. The average test conditions and Reynolds number variations were as follows:

Mach Number	Stagnation pressure	Stagnation temperature	Reynolds number per foot
3	0.5 atm	560° R	0.8×10^{6}
6	3.0 atm	760° R	1.0×10^{6}

CHAPTER III

METHOD OF ANALYSIS

The separation maneuver of two parallel stages is illustrated schematically in Figure 6. At release, the second stage would be at an initial spacing distance and attitude with respect to the first stage. A trapeze or similar mechanism could be employed to achieve the desired release conditions. Potential problems that may arise during the staging sequence are illustrated by the lower two sketches of Figure 6. The divergence of the center of gravities alone would not imply safe separation since the second stage may rotate into the first stage. Consequently, realistic analysis can only be accomplished if the separation maneuver is regarded as the motion of two finite rigid bodies.

Two parallel lifting stages, separating from each other aerodynamically, represent a complex dynamic system. For the complete description of this system, not less than 12 degrees of freedom must be taken into account. While this is possible, at least theoretically, the final accuracy of the analysis will depend on the precise analytical representation of the aerodynamic forces and moments. Accordingly, the general motion of the dynamic system must be restricted to cases for which the approximate behavior of the static aerodynamic coefficients is presently known or can easily be determined experimentally.

It was assumed that the controls of both vehicle stages were fixed and that the separation maneuver takes place above a flat non-rotating earth. Consequently, the equations needed to study the

motion of either stage are those which are derived in the Appendix, equations (A-27), (A-28), (A-29), and (A-30). These equations can be simplified considerably in the case of longitudinal (symmetric) motion where it is assumed that the launch vehicle is flying with no sideslip and with wings level and that separation of the two stages takes place in the common plane of symmetry. With these restrictions, the equations necessary to study the motion of either stage become

$$\begin{aligned} m(\dot{u} + wq) &= F'_X - mg \sin\theta \\ m(\dot{w} - uq) &= F'_Z + mg \cos\theta \\ I_{yy}\dot{q} &= M_y \\ \dot{\theta} &= q \\ \dot{x}' &= u \cos\theta + w \sin\theta \\ \dot{z}' &= -u \sin\theta + w \cos\theta \end{aligned} \tag{1}$$

The above set of six equations is completely general for symmetric vehicles and valid even for large disturbances. However, in the development of the expressions for the force and moment terms, the following assumptions are made:

1. During separation the effects of speed changes on the aerodynamic force coefficients are neglected.

2. The axial-force coefficient of either stage is not affected by the proximity of the other stage.

3. Cross coupling between the two stages takes place only through the normal-force and pitching-moment coefficients.

With the above assumptions, the force and moment terms may be expressed as

$$F_X' = \frac{1}{2}\rho V_c^2 S(C_T \cos\epsilon - C_A)$$

$$F_Z' = \frac{1}{2}\rho V_c^2 S\left(C_T \sin\epsilon - C_N + \frac{c}{2V_c} C_{N_q} q\right) \tag{2}$$

$$M_y = \frac{1}{2}\rho V_c^2 Sc\left(\frac{d_T}{c} C_T + C_m + \frac{c}{2V_c} C_{m_q} q + C_{m_{\dot{w}}} \dot{w}\right)$$

In the above equations the rotational stability derivatives C_{N_q} and C_{m_q}, and the derivative $C_{m_{\dot{w}}}$ were assumed to be constants for each stage during the separation maneuver. However, the influence of these derivatives on the separation maneuver can be investigated by varying the magnitude of these quantities in the numerical analysis. Orientation of the thrust vector is specified by ϵ, the angle between the X-axis and the thrust vector, and d_T, the perpendicular distance from the center of gravity to the thrust line. These quantities, as well as the thrust coefficient C_T, are constant for each stage. The static aerodynamic coefficients, C_A, C_N, and C_m represent the experimental data measured on each stage and are defined separately as follows:

$$
\begin{aligned}
C_{A,1} &= C_{A,1}(\alpha_1) \\
C_{A,2} &= C_{A,2}(\alpha_2) \\
C_{N,1} &= C_{N,1}(\alpha_1,\alpha_2,\Delta x,\Delta z) \\
C_{N,2} &= C_{N,2}(\alpha_1,\alpha_2,\Delta x,\Delta z) \\
C_{m,1} &= C_{m,1}(\alpha_1,\alpha_2,\Delta x,\Delta z) \\
C_{m,2} &= C_{m,2}(\alpha_1,\alpha_2,\Delta x,\Delta z)
\end{aligned}
\tag{3}
$$

The separation variables α_1, α_2, Δx, and Δz are illustrated in Figure 5.

The equations of motion were integrated numerically on a digital computer. The values of the aerodynamic coefficients were obtained by linear interpolation between the discrete points of the tabular functions at each integration step. The atmospheric density, ρ, in equation (2) corresponds to that given by the U.S. Standard Atmosphere 1962, at each height (Ref. 2).

In interpreting the numerical solutions of the present analysis, it should be pointed out that in addition to the assumptions previously discussed, equations (2) contain another source of potential error. Ideally, the unaccelerated flight of a single body can be completely simulated in the wind tunnel, whereas the separating flight of two parallel stages is impossible to simulate either kinematically or dynamically with fixed models in the test section. Thus, the direct use of the measured coefficients in equations (2) involves the error due to the wind-tunnel simulation technique where the static data are obtained for $\gamma_1 = \gamma_2$ and $(V_c)_1 = (V_c)_2$. This error is lessened by using the

instantaneous velocity of each stage in equations (3); however, even though the flight-path angle of each vehicle is varying during the separation maneuver the procedure does not take into account the effects of different flight-path angles on the static aerodynamic coefficients nor any scaling or Reynolds number effects.

CHAPTER IV

RESULTS AND DISCUSSION

The results have been divided into two principal parts. These two parts consist of the experimental results obtained for the two stages in close proximity and the numerical results obtained by integrating the equations of motion for each of the two stages during a staging maneuver. Since the aerodynamic interferences that occur when two bodies are in close proximity represent potential stability and control problems for both vehicle stages, the experimental results are used to discuss the implication of these interferences on the stability characteristics of the stages when in close proximity, while the numerical results are used to discuss the potential effects on the vehicle behavior of the aerodynamic interference.

Experimental Results

The basic longitudinal aerodynamic characteristics of the first and second stages at different vertical and longitudinal spacings, incidence angles, and Mach numbers are presented in Figures 7 to 10. For reference, the interference-free data, or the data at a very large separation distance $\left(\frac{\Delta z}{l_1} = \infty\right)$, are also shown on these Figures.

First stage.- For the first stage at $M = 3$, $i = 0^\circ$, and $\frac{\Delta x}{l_1} = -0.051$ (Fig. 7a) the static stability level, that is, the slope of the pitching-moment curve did not change appreciably with vertical spacing. However, there is a large positive increment in $C_{m,1}$ due to

the interference and a significant change in the angle for trim. Also, for the maximum vertical spacing tested, large interferences are still present because the curve at $\frac{\Delta z}{l_1} = 0.224$ has not approached the interference-free curve $\left(\frac{\Delta z}{l_1} = \infty\right)$. Figure 7a also shows that there are large negative increments in $C_{N,1}$ due to the interferences with no appreciable change in $(C_{N_\alpha})_1$. Increasing i from 0° to 10° at $M = 3$ and $\frac{\Delta x}{l_1} = -0.051$ (Figs. 7a, 7b, and 7c) caused a large positive increment in $C_{m,1}$ and a large negative increment in $C_{N,1}$. (Compare $C_{m,1}$ and $C_{N,1}$ at $\frac{\Delta z}{l_1} = 0.127$, for example.)

At the other longitudinal spacing, $\frac{\Delta x}{l_1} = 0.160$, and $i = 0^\circ$ (Fig. 7d) not only did the magnitude of $C_{m,1}$ vary with vertical spacing, but also the stability level decreased with increasing vertical spacing such that at $\frac{\Delta z}{l_1} = 0.199$ and 0.224, the first stage is statically unstable for α_1 less than about 2°. Figure 7d also shows that in comparison to the interference free curve, both $(C_{N_\alpha})_1$ and the magnitude of $C_{N,1}$ at α_1 greater than about -8° decreased due to the presence of the second stage. However, increasing the vertical spacing did not appreciably change either $(C_{N_\alpha})_1$ or $C_{N,1}$. Increasing i at $\frac{\Delta x}{l_1} = 0.160$ (Figs. 7d, 7e, and 7f) caused further decreases in the stability level, magnitude of $C_{m,1}$ and magnitude of $C_{N,1}$ as compared to the interference-free curves.

At $M = 6$, $i = 0^\circ$, and $\frac{\Delta x}{l_1} = -0.051$ Figure 8a shows that both the magnitude of $C_{m,1}$ and stability level of the first stage varied with vertical spacing. This is in contrast to the data at $M = 3$ (Fig. 7a) where only the magnitude of $C_{m,1}$ was shown to vary with

vertical spacing. Also in contrast to the data at $M = 3$ the data at the largest vertical spacing tested, $\frac{\Delta z}{l_1} = 0.224$, at $M = 6$ (Fig. 8a) indicates that the first stage is approaching interference-free conditions since both the normal-force and pitching-moment curves are approaching the interference-free curves. However, at this vertical spacing and also at $\frac{\Delta z}{l_1} = 0.199$, the first stage has pitch-up tendencies at α_1 greater than 3°. Increasing i from 0° to 10° (Figs. 8a, 8b, and 8c) at $M = 6$ and $\frac{\Delta x}{l_1} = -0.051$ caused positive increments in $C_{m,1}$ and a degradation of the static stability at all vertical spacings. Figures 8a, 8b, and 8c also show that the presence of the second stage caused negative increments in $C_{N,1}$ with some localized changes in $(C_{N_\alpha})_1$ as compared to interference-free conditions.

At the other longitudinal spacing, $\frac{\Delta x}{l_1} = 0.160$, and $M = 6$ (Figs. 8d, 8e, and 8f), the first stage was statically unstable at the smaller vertical spacings for α_1 less than about 2°. These same figures also show that the magnitude of $C_{m,1}$, $C_{N,1}$, and $(C_{N_\alpha})_1$ varied with vertical spacing.

Second stage.- For the second stage at $M = 3$, $i = 0^\circ$, and $\frac{\Delta x}{l_1} = -0.051$ (Fig. 9a), both the stability level and magnitude of $C_{m,1}$ varied with vertical spacing. At $\frac{\Delta z}{l_1}$ less than 0.175, the second stage was approximately neutrally stable or statically unstable at all α_1. Coupled with these changes in stability and magnitude of $C_{m,2}$ are changes in both $C_{N,2}$ and $(C_{N_\alpha})_2$. Increasing i from 0° to 10° at $M = 3$ and $\frac{\Delta x}{l_1} = -0.051$ (Figs. 9a, 9b, and 9c) caused the second-stage stability level to decrease and produced large negative increments in

the magnitude of $C_{m,2}$ as well as large positive increments in $C_{N,2}$. Comparison of these data (Figs. 9a, 9b, 9c) with the corresponding data for the first stage (Figs. 7a, 7b, and 7c) indicates that increasing i would tend to cause the first stage to nose up but away from the second stage, while the second stage would tend to nose down but away from the first stage.

Increasing $\frac{\Delta x}{l_1}$ from -0.051 to 0.160 for the second stage at M = 3 (Figs. 9d, 9e, and 9f) caused the vehicle to become statically stable at almost all vertical spacings, incidence angles, and α_1. However, the presence of the first stage caused increments in both $C_{m,2}$ and $C_{N,2}$ with the increments becoming larger with increasing i.

Comparison of the data for the second stage at M = 3 (Fig. 9) with the data at M = 6 (Fig. 10) at similar geometric conditions, indicates that the results at both Mach numbers are very similar. However, increasing the Mach number from 3 to 6 decreased the actual magnitude of the force and moment coefficients.

Because of the large interference increments found for the second stage, an investigation was made to determine the control effectiveness of the second stage at interference-free conditions. Figure 11 presents this control effectiveness data for control deflections of 0° and $\pm 25^\circ$. Comparison of this data with the data in Figures 9 and 10 indicates that there appears to be no reasonable control deflection which could overcome all of the large pitching-moment increments shown for the second stage when in proximity to the first stage. Furthermore, the control

effectiveness of the second stage may degrade due to the interferences or when in proximity to the first stage.

Comments on interference increments.- Further analysis of the data shown in Figures 7 to 10, along with schlieren data, has led to two major conclusions as to the source of the behavior of the force and moment coefficients as compared to their interference-free values. These can be illustrated in Figure 12. The first conclusion is that the effects on the first stage are caused by the impingement on the first stage of the bow shock wave generated by the second stage. Consequently, the changes in forces and moments previously shown for the first stage, are approximately proportional to the strength of this shock wave and the area affected. The second conclusion is that the effects on the second stage are caused by the flow field from the first stage to which must be added the effects of the first reflection of this bow shock wave. Furthermore, not only are the static aerodynamic data for both stages dependent on the relative position and attitude of the second stage and Mach number; but the data are also dependent on the relative sizes of the two stages, since the flow field of the first stage and the strength of the bow shock wave generated by the second stage are direct functions of the size of the two vehicles. The relative size of the two vehicles depends on the take-off mode of the launch vehicle (vertical versus horizontal), mission requirements, and the choice of propulsion systems for the launch vehicle.

Numerical Results

When the equations of motion (eq. (1)) for each stage are coupled through the aerodynamic coefficients, the result is a system of 12 simultaneous ordinary linear differential equations with 12 initial conditions. Since the initial time is conveniently chosen to be the moment of release, not all 12 initial conditions are independent. For instance, at release both stages are still flying together; consequently the initial velocities, both in magnitude and direction, must be the same. The initial spacing distance places similar requirements on the initial location and angular orientation of the two stages.

The equations of motion were integrated numerically on a digital computer. The static aerodynamic inputs into the program consisted of the normal-force and pitching-moment coefficients for the two stages at different relative positions and attitudes when the stages were in close proximity to each other. The axial-force data used was that which was obtained at interference-free conditions for each stage. The dynamic derivatives C_{N_q}, C_{m_q}, and $C_{m_{\dot{w}}}$ were estimated for each stage from data for similar type configurations such as the XB-70 for the first stage and the HL-10 for the second stage. However, as will be illustrated later, safe separation trajectories were not obtainable with these values and larger values had to be selected to achieve safe separation. Vehicle input data consisted of the masses of the individual stages, m_1 and m_2, and the pitch moments of inertia, $(I_{yy})_1$ and $(I_{yy})_2$. Other vehicle input data consisted of the initial geometric quantities describing the initial position and attitude of the second stage with

respect to the first stage, namely, i, Δx, and Δz. Quantities characteristic of the trajectory flown by the launch vehicle at staging conditions were also treated as inputs and included the altitude, h, pitch velocity, q, flight-path angle, γ, velocity, V_c, and angle of attack, α_1.

For the numerical integration the size of the computing interval was carefully selected. This selection was accomplished by the use of two different integration techniques for each of which the size of the computing interval was systematically varied. Comparison of the solutions obtained in this manner indicated that a Δt of 0.005 seconds resulted in a negligible error in the numerical results.

The computer time involved in obtaining solutions puts practical limits on the number of variables and vehicle characteristics which can be investigated. Accordingly, for the present analysis, staging was assumed to occur in climbing flight; and Mach numbers of 3 and 6 were selected for the analysis. The Mach number 3 condition could correspond either to an abort or to a normal mission staging condition, while the Mach 6 condition would probably be a mission staging condition only. These considerations led to the selection of a number of fixed vehicle characteristics and initial conditions given in Table II.

A typical altitude Mach number ascent trajectory plot, shown only for Mach numbers less than 8, is illustrated in Figure 13 and indicates where abort and mission staging conditions might be required. Typical reusable launch vehicles employing air-breathing engines only would probably stage at the lower altitudes and resulting higher dynamic

pressures, whereas rocket-powered vehicles would stage at the higher altitudes and lower dynamic pressures. Normal mission staging could occur, depending on the vehicle concept, anywhere above a Mach number of about 3; while abort staging could occur at any Mach number below mission staging. Abort separation for either rocket or air-breathing type vehicles would likely occur at the higher dynamic pressures.

Example solutions.- Figure 14 illustrates typical numerical results at $M = 3$ for two particular choices of the initial conditions and the damping in pitch characteristics. The vehicles were assumed to have safely separated when the vehicles were one first-stage body length apart and to have collided when the extremities of the vehicles touched each other. The main points of this Figure are that (1) the time required for the vehicles to collide or separate was of the order of 3 seconds, a very short time for aerodynamic controls to be effective (probably of the order of 2 seconds at these speeds and altitudes); (2) the net change in the initial and final velocities of either stage during the separation maneuver would amount to a net Mach number change of about 0.10 and would have a negligible effect on the static aerodynamic coefficients, thus justifying assumption 1 in Chapter III; (3) the difference between γ_1 and γ_2 which was a maximum of 1.75° for the safe separation case, could introduce some errors in the calculations (since the static aerodynamic coefficients were obtained for $\gamma_1 = \gamma_2$) and could affect whether the vehicles would collide or safely separate.

As has been previously implied, no attempt was made in the present study to investigate the effect of all important vehicle characteristics, initial conditions, and damping characteristics either separately or in all reasonable combinations. Instead, attention was given to some of the least accurately known damping variables, namely $(C_{m_q})_1$ and $(C_{m_q})_2$, and to some of the initial conditions which have obvious bearing on successful separation. Included in the latter category were the initial relative attitude, dynamic pressure, and vertical thrusting. The damping variables $(C_{m_q})_1$ and $(C_{m_q})_2$ are difficult to obtain either analytically or experimentally at these high Mach numbers even for the interference-free condition. Since the static aerodynamic data indicated large changes in the pitching-moment characteristics for both vehicle stages when they were in close proximity, it can only be expected that C_{m_q} would also vary during the separation maneuver. The manner in which C_{m_q} varies when the vehicles are in close proximity is beyond the scope of the present investigation and consequently, as was mentioned previously, C_{m_q} was held constant during the separation maneuver.

Effect of dynamic derivatives.- Figure 15a shows the effect of the dynamic derivatives at $M = 3$ and $h = 70{,}000$ feet where $(C_{m_q})_1$ is plotted against $(C_{m_q})_2$. Indicated in this Figure are the regions where the two vehicles collided, an approximate region where they are safely separated, and a region of uncertainty as to whether the two vehicles would collide or separate. Also indicated in this Figure are the best current estimates of the interference-free values of C_{m_q} for both the first and second stages. These values are one or more orders of

magnitude smaller than the values needed to achieve safe separation at these conditions. Figure 15b indicates similar results at $M = 6$ and $h = 110{,}000$ feet. Although the magnitude of $C_{m_{\dot{w}}}$ and C_{N_q} for both the first and second stage have not been perturbed in this analysis, it can be expected that similar figures would be generated for these quantities at both Mach numbers.

Effect of initial attitude.- For the purpose of illustrating some of the other important variables that may need to be considered to achieve safe separation, Figure 16 shows the type of results that can be generated by selecting a value of C_{m_q} which lies in the safe separation region for both the first and second stage at $M = 3$ and 6 (square symbol, Fig. 15). Here the incidence angle and the angle of attack of the first stage have been varied at $M = 3$ (Fig. 16a) and $M = 6$ (Fig. 16b). Again, the regions of collision, uncertainty, and safe separation are shown. Similar results are again illustrated at both Mach numbers.

Effect of dynamic pressure.- Figure 17 shows the effect of varying the dynamic pressure or altitude for the separation maneuver by taking a suitable safe separation value of i and α_1 (circular symbol, Fig. 16). The distance between the centers of gravity of the two stages in 2 seconds after release has been plotted against dynamic pressure. The dynamic pressure range is for altitudes above and below the nominal altitude for a rocket-powered vehicle at $M = 3$ and 6. Two curves are presented; one is for the condition in which no thrust was used in the calculations and the other is for the conditions in which a hypothetical

vertical downward thrust corresponding to a thrust-to-weight ratio of 0.1 has been applied to the first stage. Using either vertical or longitudinal thrust would present plume-body interactions which, in these calculations, have not been evaluated. For the no-thrust condition at $M = 3$ (Fig. 17a) and zero dynamic pressure, the position and attitude of the vehicles do not change; and separation does not occur. Safe separation can be expected only at the higher dynamic pressures for the no-thrust condition. For the vertical-thrust condition at $M = 3$, safe separation could result at low dynamic pressures but as the dynamic pressure increases, there is a region of collision. At the higher dynamic pressures, safe separation would also be predicted.

At $M = 6$ (Fig. 17b) safe separation was achieved for all conditions except at the extremely low dynamic pressures using no vertical thrust. However, the values of C_{m_q} required for both the first and second stage to achieve safe separation are much larger than the best current estimates of the interference-free values.

Figures 15, 16, and 17 have indicated some of the potential problems associated with parallel stage separation. These results have indicated that evaluating the potential of any parallel staged system will require a critical trajectory analysis of the two vehicles when in close proximity to determine the constraints under which safe separation of the two vehicles may be achievable.

CHAPTER V

CONCLUDING REMARKS

An exploratory study has been made of the stage separation of parallel staged reusable launch vehicles. Static longitudinal aerodynamic data were obtained for both stages of a representative two-stage rocket-powered reusable launch vehicle concept when the stages were in close proximity to each other. The effects of vertical spacing, longitudinal spacing, and incidence angle were determined at Mach numbers of 3 and 6. Using the wind-tunnel data together with estimates of the dynamic derivatives obtained for similar type vehicles and also the vehicle and initial trajectory input data, the implication of the interferences on the individual vehicle dynamics was obtained at Mach numbers of 3 and 6 by numerically integrating the equations of motion for both vehicle stages.

The experimental results indicated that for the first stage, the proximity of the second stage produced large positive increments in the pitching-moment coefficient coupled with large negative increments in the normal-force coefficient. Increasing the incidence angle of the second stage resulted in further positive increments in the pitching-moment coefficient and further negative increments in the normal-force coefficient. In general, the presence of the second stage caused the first-stage static stability level to decrease and at some of the geometric conditions tested, the first stage was statically unstable.

For the second stage, the proximity of the first stage generally resulted in large negative increments in the pitching coefficient and large positive increments in the normal-force coefficient. Increasing the incidence angle resulted in further negative increments in the pitching-moment coefficients and further positive increments in the normal-force coefficients. The presence of the first stage generally caused the second stage to become unstable at almost all geometric conditions tested.

From control effectiveness data obtained for the second stage at interference-free conditions, there appears to be no aerodynamic control surface of reasonable dimensions which could overcome the large pitching-moment increments.

The observed changes in forces and moments were primarily caused for the first stage by the bow shock wave generated by the second stage. For the second stage, the changes in forces and moments were primarily caused by the flow field from the first stage to which must be added the effects of the first reflection of the bow shock wave generated by the second stage.

The static aerodynamic data for both stages were found to be dependent on the relative position and attitude of the second stage, the flight Mach number, and the relative sizes of the two stages. The relative sizes of the two stages depend on the take-off mode of the launch vehicle (vertical versus horizontal), mission requirements, and the choice of propulsion system for the launch vehicle.

The numerical results indicated that safe separation is strongly dependent on the dynamic derivatives, the initial attitude of the two stages, and the dynamic pressure at staging. Perhaps the most significant result observed is that to achieve safe separation in the sensible atmosphere, the damping in pitch values required are one or more orders of magnitude larger than the best estimates for their interference-free values. However, to realistically assess the impact of the dynamic derivatives, dynamic derivative data are strongly needed for these types of vehicles at high supersonic and hypersonic Mach numbers; at interference-free conditions as well as when the vehicles are in close proximity to each other.

These results have indicated that a potentially hazardous situation could be expected in separating parallel-arranged stages. However, to evaluate the potential of safely separating any given system will require critical trajectory analysis of the system under consideration to determine the constraints for which safe separation may be achievable. Furthermore, other avenues of approach such as trajectory shaping, vehicle shaping, various thrusting maneuvers (including attitude control thrust), stability augmentation, and other auxiliary devices need to be considered.

The experimental technique and method of analysis used in the present study are applicable to the separation of external stores from aircraft flying at high supersonic or hypersonic speeds. There are, however, two limitations which might present some difficulties. The first of these is that the experimental aerodynamic data cannot be

obtained, at present, if any lateral motion occurs during the separation maneuver; therefore, it was assumed that the separation of both vehicles takes place in the common plane of symmetry. The second of these limitations is that, even though the flight-path angle of each vehicle is varying during the separation maneuver, the procedure does not take into account the effects of different flight-path angles on the aerodynamic coefficients; the aerodynamic coefficient data are obtained for the condition of flight-path angles of both vehicles equal to each other.

REFERENCES

1. Stokes, George M.: Description of a 2-Foot Hypersonic Facility at the Langley Research Center. NASA TN D-939, 1961.
2. U.S. Standard Atmosphere, 1962; Government Printing Office, Washington 25, D.C.
3. Etkin, Bernard: Dynamics of Flight. John Wiley and Sons, Inc., New York, 1959.

TABLE I.- GEOMETRIC CHARACTERISTICS OF MODELS

AND REFERENCE DIMENSIONS

First stage:

Body length	23.760 inches
Overall length	23.760 inches
Aspect ratio	1.865
Span	13.802 inches
Total wing area	102.135 inches^2
Reference area	102.135 inches^2
Root chord	14.800 inches
Tip chord	0
Mean aerodynamic chord	9.867 inches
Reference length	9.867 inches

Second stage:

Body length	11.465 inches
Overall length	13.706 inches
Aspect ratio	0.678
Span	6.050 inches
Planform area less vertical fins	53.980 inches^2
Reference area	53.980 inches^2
Reference length	11.465 inches

TABLE II.- VEHICLE CHARACTERISTICS AND INITIAL CONDITIONS

First stage:

W	345,000 pounds
I_{yy}	11.00×10^6 slugs-ft^2
c	78.11 feet
S	6,401 feet^2
$C_{m_{\dot{w}}}$	0
C_{m_q}	variable
C_{N_q}	0
γ_1	26°

Second stage:

W	303,000 pounds
I_{yy}	1.75×10^6 slugs-ft^2
c	90.76 feet
S	3,383 feet^2
$C_{m_{\dot{w}}}$	0
C_{m_q}	variable
C_{N_q}	0
$\frac{\Delta x}{l_1}$	-0.051
$\frac{\Delta z}{l_1}$	0.127
γ_2	26°

APPENDIX

DERIVATION OF THE RIGID-BODY EQUATIONS OF MOTION FOR AN AIRCRAFT WITH THE CONTROLS FIXED

In the interest of completeness, the rigid-body equations are derived from first principles. The method is similar to the approach used by Etkin (Ref. 3).

Let δm (Fig. A-1) be an element of mass of the airplane and have a velocity $\bar{v}$ relative to space-fixed axes. Let $\delta\bar{F}$ be the resultant force which acts upon it.

$$\delta\bar{F} = \delta m \frac{d\bar{v}}{dt} \tag{A-1}$$

Summing all elements of the airplane gives

$$\sum \delta\bar{F} = \sum \delta m \frac{d\bar{v}}{dt} = \frac{d}{dt} \sum \bar{v}\, \delta m \tag{A-2}$$

where

$$\bar{v} = \bar{v}_c + \frac{d\bar{s}}{dt} \tag{A-3}$$

First, look at the term $\sum \bar{v}\, \delta m$

$$\sum \bar{v}\, \delta m = \sum \left(\bar{v}_c + \frac{d\bar{s}}{dt}\right) \delta m = m\bar{v}_c + \frac{d}{dt} \sum \bar{s}\, \delta m$$

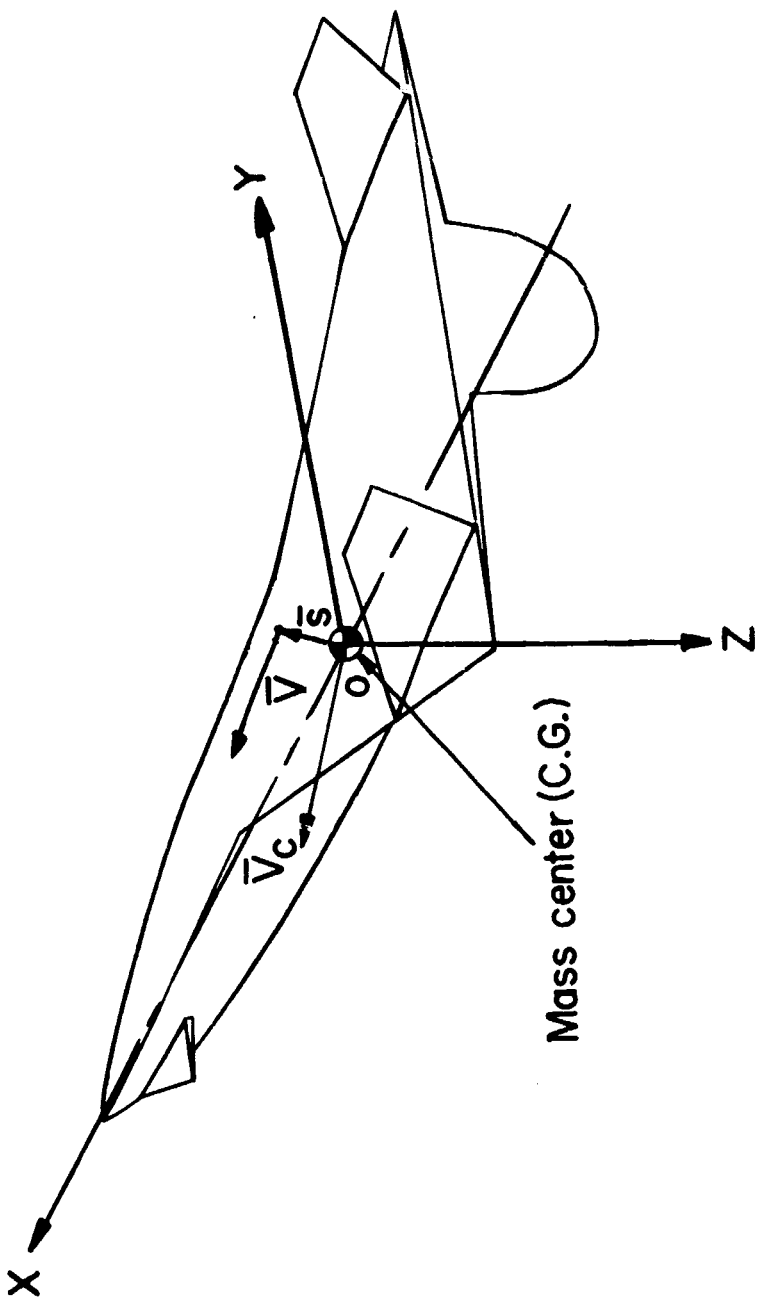

Figure A-1.

Since the equations are being written for a coordinate system at the mass center, $\int \bar{s}\,\delta m = 0$. Therefore,

$$\int \bar{v}\,\delta m = m\bar{v}_c \tag{A-4}$$

Substituting equation (A-4) into (A-2) gives

$$\int \delta\bar{F} = \bar{F} = \frac{d}{dt}(m\bar{v}_c)$$

or

$$\bar{F} = m\frac{d\bar{v}_c}{dt} \tag{A-5}$$

It is now desired to obtain an equation for the moments about the mass center. The moment of momentum of δm is, by definition,

$$\delta\bar{H} = \bar{s} \times \bar{v}\,\delta m$$

Consider

$$\frac{d}{dt}(\delta\bar{H}) = \frac{d}{dt}(\bar{s} \times \bar{v})\delta m = \frac{d\bar{s}}{dt} \times \bar{v}\,\delta m + \bar{s} \times \frac{d\bar{v}}{dt}\,\delta m \tag{A-6}$$

From equation (A-3)

$$\frac{d\bar{s}}{dt} = \bar{v} - \bar{v}_c$$

Also,

$$\bar{s} \times \frac{d\bar{v}}{dt}\,\delta m = \bar{s} \times \delta\bar{F} = \delta\bar{G}$$

Therefore, equation (A-6) now becomes

$$\delta\bar{G} = \frac{d}{dt}(\delta\bar{H}) - (\bar{v} - \bar{v}_c) \times \bar{v}\,\delta m$$

or

$$\delta\bar{G} = \frac{d}{dt}(\delta\bar{H}) + \bar{v}_c \times \bar{v}\,\delta m \tag{A-7}$$

Equation (A-7) is now summed for all elements

$$\sum \delta\bar{G} = \frac{d}{dt}\sum (\delta\bar{H}) + \bar{v}_c \times \sum \bar{v}\,\delta m = \frac{d}{dt}\sum (\delta\bar{H}) + \bar{v}_c \times m\bar{v}_c$$

or

$$\sum \delta\bar{G} = \frac{d}{dt}\sum (\delta\bar{H}) \tag{A-8}$$

Now, $\sum \delta\bar{G}$ = the resultant external moment about center of gravity while $\sum \delta\bar{H}$ = the angular momentum of the airplane about center of gravity. Consequently, equation (A-8) becomes

$$\bar{G} = \frac{d\bar{H}}{dt} \tag{A-9}$$

It is necessary now to evaluate the angular momentum $\bar{H}$.

$$\bar{H} \equiv \sum \delta\bar{H} = \sum (\bar{s} \times \bar{v})\delta m$$

Let the angular velocity of the airplane be

$$\bar{\omega} = p\bar{i} + q\bar{j} + r\bar{k} \tag{A-10}$$

The derivative of a vector $\bar{E}$, referred to a frame of reference rotating with angular velocity $\bar{\omega}$ can be shown to be given by the following equation:

$$\frac{d\bar{E}}{dt} = \left[\frac{d\bar{E}}{dt}\right]_{\text{Moving system}} + \bar{\omega} \times \bar{E} \tag{A-11}$$

Consequently, the velocity of a point in a rotating rigid body is given by

$$\frac{d\bar{s}}{dt} = \left[\frac{d\bar{s}}{dt}\right]_{\text{Moving system}} + \bar{\omega} \times \bar{s}$$

or

$$\bar{v} = \bar{v}_c + \bar{\omega} \times \bar{s} \tag{A-12}$$

Therefore,

$$\bar{H} = \sum (\bar{s} \times \bar{v})\delta m = \sum (\bar{s} \times (\bar{v}_c + \bar{\omega} \times \bar{s})\delta m$$

$$\bar{H} = \sum \bar{s} \times \bar{v}_c \, \delta m + \sum \bar{s} \times (\bar{\omega} \times \bar{s}) \delta m \qquad \text{(A-13)}$$

Now, since $\sum \bar{s} \, \delta m = 0$, the expression

$$\sum \bar{s} \times \bar{v}_c \, \delta m = \sum \bar{s} \, \delta m \times \bar{v}_c = 0$$

The second term on the right-hand side of equation (A-13) becomes

$$\sum s \times (\bar{\omega} \times \bar{s}) \delta m = \sum \left[\bar{\omega}(s^2) - \bar{s}(\bar{\omega} \cdot \bar{s}) \right] \delta m$$

Consequently, equation (A-13) reduces to

$$\bar{H} = \bar{\omega} \sum s^2 \delta m - \sum \bar{s}(\bar{\omega} \cdot \bar{s}) \delta m \qquad \text{(A-14)}$$

With $\bar{s} = x\bar{i} + y\bar{j} + z\bar{k}$ and $\bar{H} = H_x\bar{i} + H_y\bar{j} + H_z\bar{k}$, equation (A-14) can be broken down into its scalar components which are as follows:

$$H_x = p \sum (x^2 + y^2 + z^2) \delta m - \sum (px^2 + qxy + rxz) \delta m$$

$$H_y = q \sum (x^2 + y^2 + z^2) \delta m - \sum (pxy + qy^2 + ryz) \delta m$$

$$H_z = r \sum (x^2 + y^2 + z^2) \delta m - \sum (pxy + qyz + rz^2) \delta m$$

or

$$H_x = p \sum (y^2 + z^2)\delta m - \sum (qxy + rxz)\delta m$$

$$H_y = q \sum (x^2 + z^2)\delta m - \sum (pxy + ryz)\delta m \qquad \text{(A-15)}$$

$$H_z = r \sum (x^2 + y^2)\delta m - \sum (pxz + qyz)\delta m$$

Now

$$I_{xx} \equiv \sum (y^2 + z^2)\delta m$$

$$I_{yy} \equiv \sum (x^2 + z^2)\delta m$$

$$I_{zz} \equiv \sum (x^2 + y^2)\delta m$$

$$I_{xy} \equiv \sum xy\ \delta m$$

$$I_{xz} \equiv \sum xz\ \delta m$$

$$I_{yz} \equiv \sum yz\ \delta m$$

Therefore, equations (A-15) can be written as

$$H_x = I_{xx}p - I_{xy}q - I_{xz}r$$

$$H_y = -I_{xy}p + I_{yy}q - I_{yz}r \tag{A-16}$$

$$H_z = -I_{xz}p - I_{yz}q + I_{zz}r$$

The vector equations of motion (eqs. (A-5) and (A-9)) then become, when referred to the coordinate system fixed to the airplane (X,Y,Z):

$$\bar{F} = m\left[\frac{d\bar{v}_c}{dt}\right]_{\text{Moving system}} + m(\bar{\omega} \times \bar{v}_c) \tag{A-17}$$

$$\bar{G} = \left[\frac{d\bar{H}}{dt}\right]_{\text{Moving system}} + \bar{\omega} \times \bar{H} \tag{A-18}$$

where

$$\bar{F} = F_x\bar{i} + F_y\bar{j} + F_z\bar{k}$$

$$\bar{G} = M_x\bar{i} + M_y\bar{j} + M_z\bar{k}$$

$$\bar{H} = H_x\bar{i} + H_y\bar{j} + H_z\bar{k}$$

$$\bar{\omega} = p\bar{i} + q\bar{j} + r\bar{k}$$

$$\bar{v}_c = u\bar{i} + v\bar{j} + w\bar{k}$$

Equations (A-17) and (A-18) have the scalar components:

$$F_x = m(\dot{u} + qw - rv)$$

$$F_y = m(\dot{v} + ru - pw) \qquad \text{(A-19)}$$

$$F_z = m(\dot{w} + pv - qu)$$

$$M_x = \dot{H}_x + qH_z - rH_y$$

$$M_y = \dot{H}_y + rH_x - pH_z \qquad \text{(A-20)}$$

$$M_z = \dot{H}_z + pH_y - qH_x$$

Since the frame of reference for the equations of motion is fixed to the airplane and moves with it, the position and orientation of the airplane cannot be described relative to it. For this purpose Euler's Angles are used to describe motion of the airplane. The Eulerian angles are defined as the three successive angles of rotation needed to carry out the transformation from a given cartesian coordinate system to another. The following three rotations for the Euler's Angles will be used (see Fig. A-2):

(a) A rotation ψ about Z_1-axis.

(b) A rotation θ about Y_2-axis.

(c) A rotation ϕ about X_3-axis.

To obtain the necessary transformation matrix, a rotation about Z_1-axis is done first. The transformation matrix is as follows:

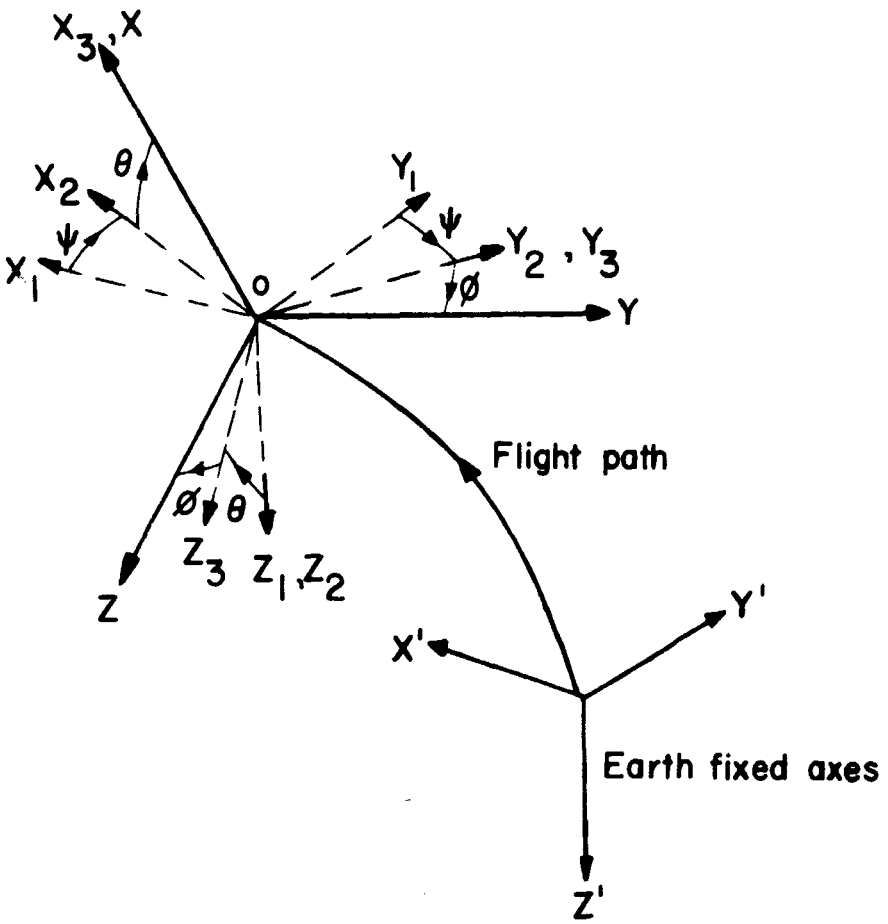

Figure A-2

$$A = \begin{bmatrix} \cos\psi & -\sin\psi & 0 \\ \sin\psi & \cos\psi & 0 \\ 0 & 0 & 1 \end{bmatrix}$$

Secondly, rotate about the Y_2-axis. The transformation matrix is as follows:

$$B = \begin{bmatrix} \cos\theta & 0 & \sin\theta \\ 0 & 1 & 0 \\ -\sin\theta & 0 & \cos\theta \end{bmatrix}$$

Thirdly, rotate about the X_3 - axis. The transformation matrix is as follows:

$$C = \begin{bmatrix} 1 & 0 & 0 \\ 0 & \cos\phi & -\sin\phi \\ 0 & \sin\phi & \cos\phi \end{bmatrix}$$

The product matrix $D = ABC$ then is as follows, where D = the transformation matrix from body coordinates to space coordinates,

$$D = ABC = \begin{bmatrix} \cos\psi\cos\theta & \sin\theta\sin\phi\cos\psi - \sin\psi\cos\phi & \cos\psi\cos\phi\sin\theta + \sin\psi\sin\phi \\ +\sin\psi\cos\theta & +\sin\psi\sin\phi\sin\theta + \cos\psi\cos\phi & +\sin\psi\cos\phi\sin\theta - \sin\phi\cos\psi \\ -\sin\theta & \sin\phi\cos\theta & \cos\theta\cos\phi \end{bmatrix}$$

(A-21)

Consequently, to obtain the transformation from space coordinates to body coordinates, we use the transformation matrix D

$$[x'] = [D][x]$$

where $[x']$ refers to the space coordinate system and $[x]$ refers to the body coordinate system. To obtain the coordinates of the flight path

relative to a fixed frame of reference as shown in Figure A-2, use the transformation matrix D.

If the velocity matrix in the fixed frame is

$$\begin{bmatrix} u' \\ v' \\ w' \end{bmatrix} = \begin{bmatrix} \frac{dx'}{dt} \\ \frac{dy'}{dt} \\ \frac{dz'}{dt} \end{bmatrix}$$

the relationship between the body coordinate system and fixed coordinate system is found as follows:

$$\begin{bmatrix} \frac{dx'}{dt} \\ \frac{dy'}{dt} \\ \frac{dz'}{dt} \end{bmatrix} = [D] \begin{bmatrix} u \\ v \\ w \end{bmatrix}$$

where u, v, w are the components of the velocity vector in the body coordinate system, or

$$\left.\begin{aligned}
\frac{dx'}{dt} &= u\cos\theta\cos\psi + v(\sin\theta\sin\phi\cos\psi - \sin\psi\cos\phi) \\
&\quad + w(\cos\psi\cos\phi\sin\theta + \sin\psi\sin\phi) \\
\frac{dy'}{dt} &= u\sin\psi\cos\theta + v(\sin\psi\sin\phi\sin\theta + \cos\psi\cos\phi) \\
&\quad + w(\sin\psi\cos\phi\sin\theta - \sin\phi\cos\psi) \\
\frac{dz'}{dt} &= -u\sin\theta + v\sin\phi\cos\theta + w\cos\theta\cos\phi
\end{aligned}\right\} \qquad \text{(A-22)}$$

It is now desired to express the orientation of the airplane in terms of the angular velocity components $(\dot{\psi},\dot{\theta},\dot{\phi})$. From the rotations used previously, we have

$$\begin{aligned}
\omega_\phi &= \dot{\phi} = \text{angular velocity about X-axis} \\
\omega_\theta &= \dot{\theta} = \text{angular velocity about } Y_2\text{-axis} \\
\omega_\psi &= \dot{\psi} = \text{angular velocity about } Z_1\text{-axis}
\end{aligned} \qquad \text{(A-23)}$$

In vector notation,

$$\bar{\omega} = \bar{i}\dot{\phi} + \bar{j}_3\dot{\theta} + \bar{k}_2\dot{\psi}$$

In the body axes coordinate system (X,Y,Z) (see Fig. A-2),

$$\bar{\omega} = p\bar{i} + q\bar{j} + r\bar{k}$$

If the components of $\bar{\omega}$ given by equation (A-23) are projected onto the X,Y,Z axes, or body axes, the following relations are obtained in matrix notation

$$(\omega_{\psi})_{body} = [D]^{-1}\begin{bmatrix}0\\0\\\dot{\psi}\end{bmatrix} = \begin{bmatrix}-\dot{\psi}\sin\theta\\ \dot{\psi}\sin\phi\cos\theta\\ \dot{\psi}\cos\theta\cos\phi\end{bmatrix}$$

$$(\omega_{\theta})_{body} = [C][B]\begin{bmatrix}0\\\dot{\theta}\\0\end{bmatrix} = \begin{bmatrix}0\\ \dot{\theta}\cos\theta\\ -\dot{\theta}\sin\phi\end{bmatrix}$$

$$(\omega_{\phi})_{body} = \begin{bmatrix}\dot{\phi}\\0\\0\end{bmatrix}$$

Consequently,

$$[\omega] = \begin{bmatrix}p\\q\\r\end{bmatrix} = (\omega_{\psi})_{body} + (\omega_{\theta})_{body} + (\omega_{\phi})_{body}$$

or

$$\begin{aligned} p &= \dot{\phi} - \sin\theta\,\dot{\psi} \\ q &= \dot{\theta}\cos\phi + \dot{\psi}\sin\phi\cos\theta \\ r &= \dot{\psi}\cos\theta\cos\phi - \dot{\theta}\sin\phi \end{aligned} \qquad \text{(A-24)}$$

For the problem at hand, the body axis system was chosen, in which case the X-axis is fixed to a longitudinal reference line in

the airplane. The airplane was assumed to have exact symmetry about the selected axis system. In this case,

$$I_{yz} = I_{xy} = 0 \tag{A-25}$$

With the aerodynamic forces (including propulsive forces) denoted by F'_x, F'_y, F'_z, the resultant external forces are (see Fig. A-3):

$$\begin{aligned} F_x &= F'_x - mg \sin\theta \\ F_y &= F'_y + mg \cos\theta \sin\phi \\ F_z &= F'_z + mg \cos\theta \cos\phi \end{aligned} \tag{A-26}$$

The kinematical and dynamical equations derived in the foregoing are now collected.

Substituting equations (A-19) into (A-26) and solving for $\dot{u}$, $\dot{v}$, $\dot{w}$, the following equations are obtained

$$\begin{aligned} \dot{u} &= rv - qw - g \sin\theta + \frac{1}{m} F'_x \\ \dot{v} &= pw - ru + g \cos\theta \sin\phi + \frac{1}{m} F'_y \\ \dot{w} &= qu - pv + g \cos\theta \cos\phi + \frac{1}{m} F'_z \end{aligned} \tag{A-27}$$

Substituting equations (A-16) into (A-20) and solving for $\dot{p}$, $\dot{q}$, $\dot{r}$, the following equations are obtained

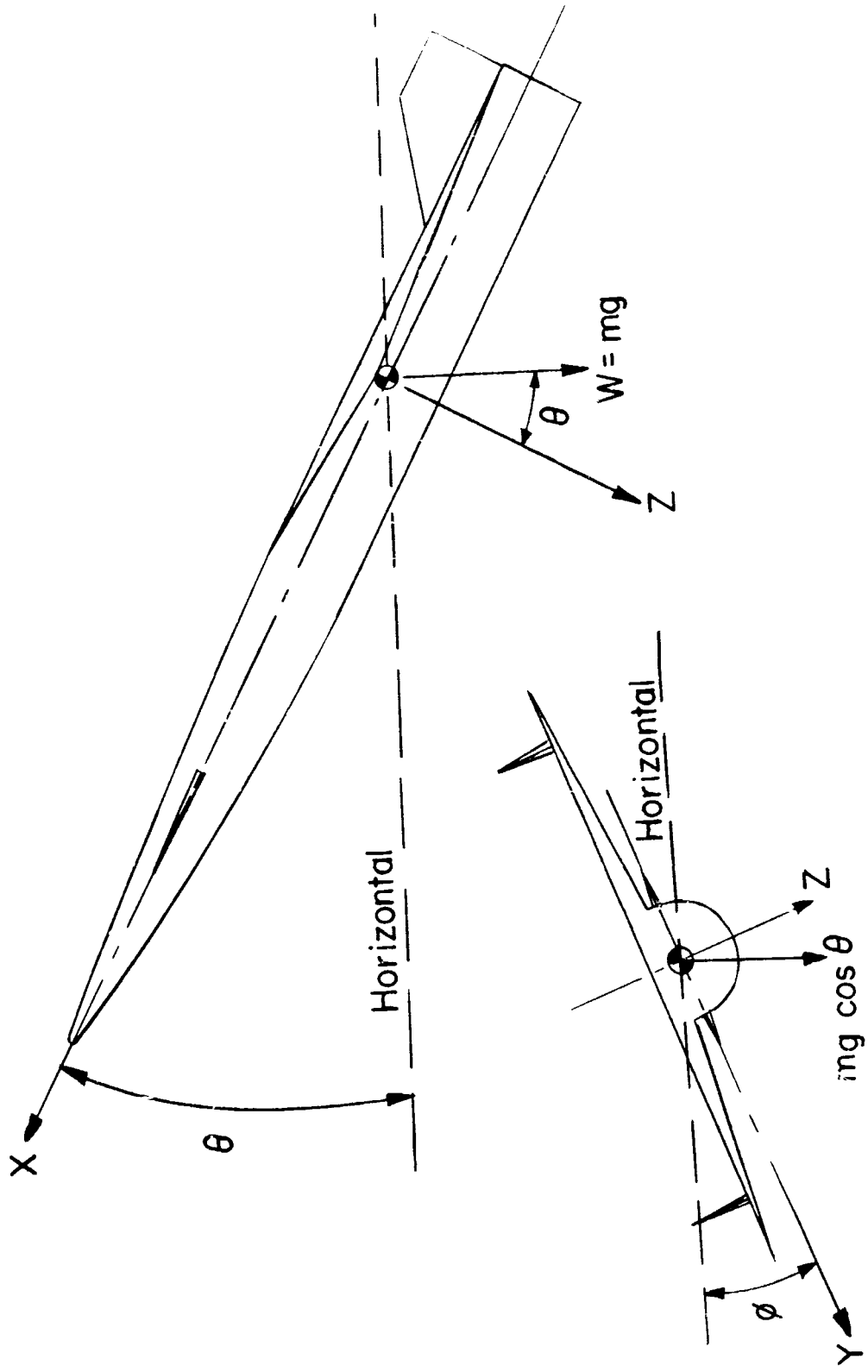

Figure A-3.

$$\dot{p} = (A_1)pq - (A_2)qr + (A_3)M_x + (A_4)M_z$$

$$\dot{q} = (A_5)pr - (A_6)(r^2 - p^2) + (A_7)M_y \qquad \text{(A-28)}$$

$$\dot{r} = (A_8)pq - (A_1)qr + (A_4)M_x + (A_9)M_z$$

where

$$A_1 = I_{xx}I_{zz} - I_{xz}^2$$

$$A_2 = I_{xz}(I_{xx} - I_{yy} + I_{zz})$$

$$A_3 = I_{xx}^2 - I_{xx}I_{yy} + I_{xy}^2$$

$$A_4 = I_{zz}^2 - I_{zz}I_{yy} + I_{xz}^2$$

$$A_5 = \frac{(I_{zz} - I_{xx})}{I_{yy}}$$

$$A_6 = \frac{I_{xz}}{I_{yy}}$$

$$A_7 = \frac{1}{I_{yy}}$$

$$A_8 = \frac{A_3}{A_1}$$

$$A_9 = \frac{I_{xx}}{A_1}$$

The equations used to describe the angular positions of the airplane are equations (A-24) - solved for $\dot{\theta}$, $\dot{\phi}$, and $\dot{\psi}$:

$$\dot{\theta} = q \cos \phi - r \sin \phi$$

$$\dot{\phi} = p + q \sin \phi \tan \theta + r \cos \phi \tan \theta \qquad \text{(A-29)}$$

$$\dot{\psi} = (q \sin \phi + r \cos \phi)\sec \theta$$

The position of the center of gravity of the airplane referenced in earth-fixed coordinate system is given by equations (A-22):

$$\left.\begin{aligned}
\dot{x}' &= u \cos \theta \cos \psi + v(\sin \phi \sin \theta \cos \psi - \sin \psi \cos \phi) \\
&\quad + w(\cos \psi \cos \phi \sin \theta + \sin \psi \sin \phi) \\
\dot{y}' &= u \sin \psi \cos \theta + v(\sin \psi \sin \phi \sin \theta + \cos \psi \cos \phi) \\
&\quad + w(\sin \psi \cos \phi \sin \theta - \sin \phi \cos \psi) \\
\dot{z}' &= u \sin \theta + v \sin \phi \cos \theta + w \cos \theta \cos \phi
\end{aligned}\right\} \qquad \text{(A-30)}$$

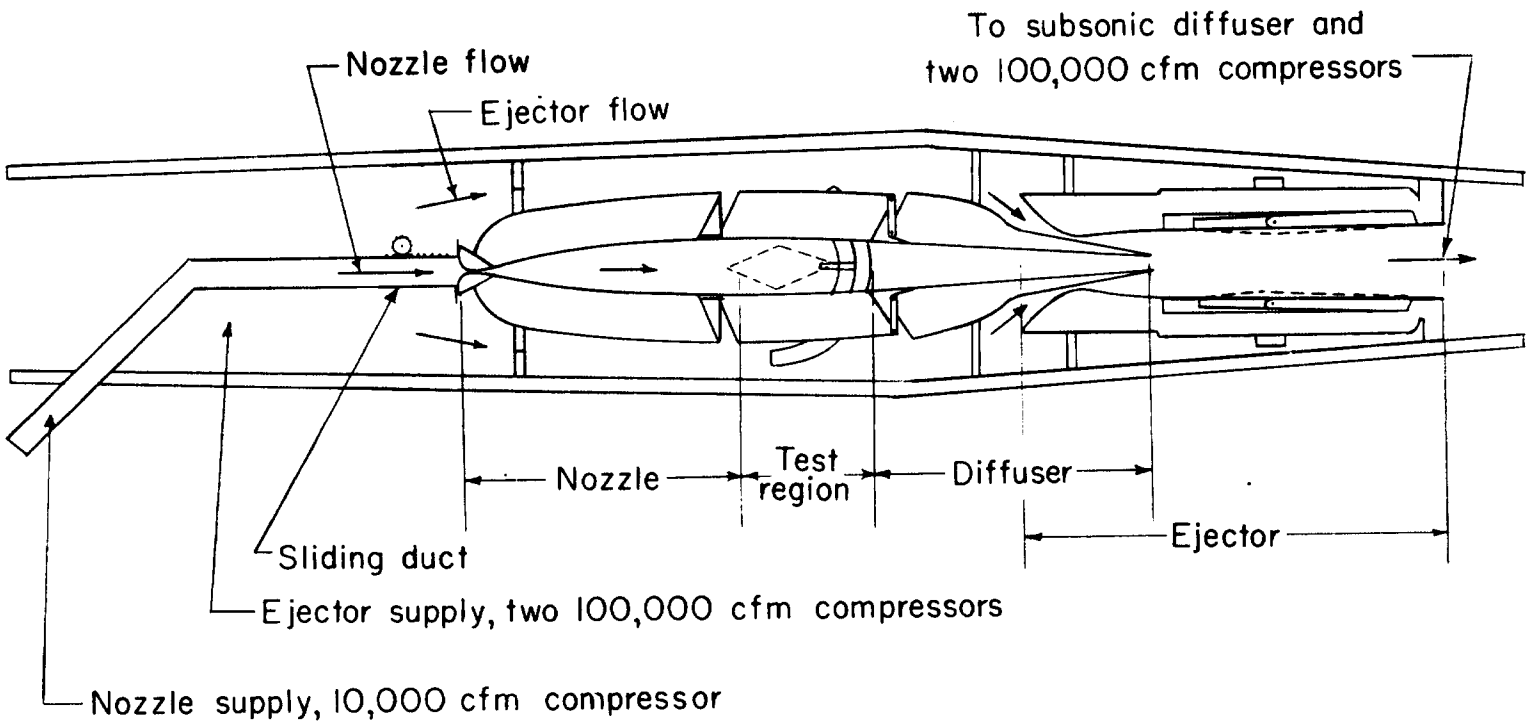

Figure 1.- Schematic of 2-foot hypersonic facility testing section.

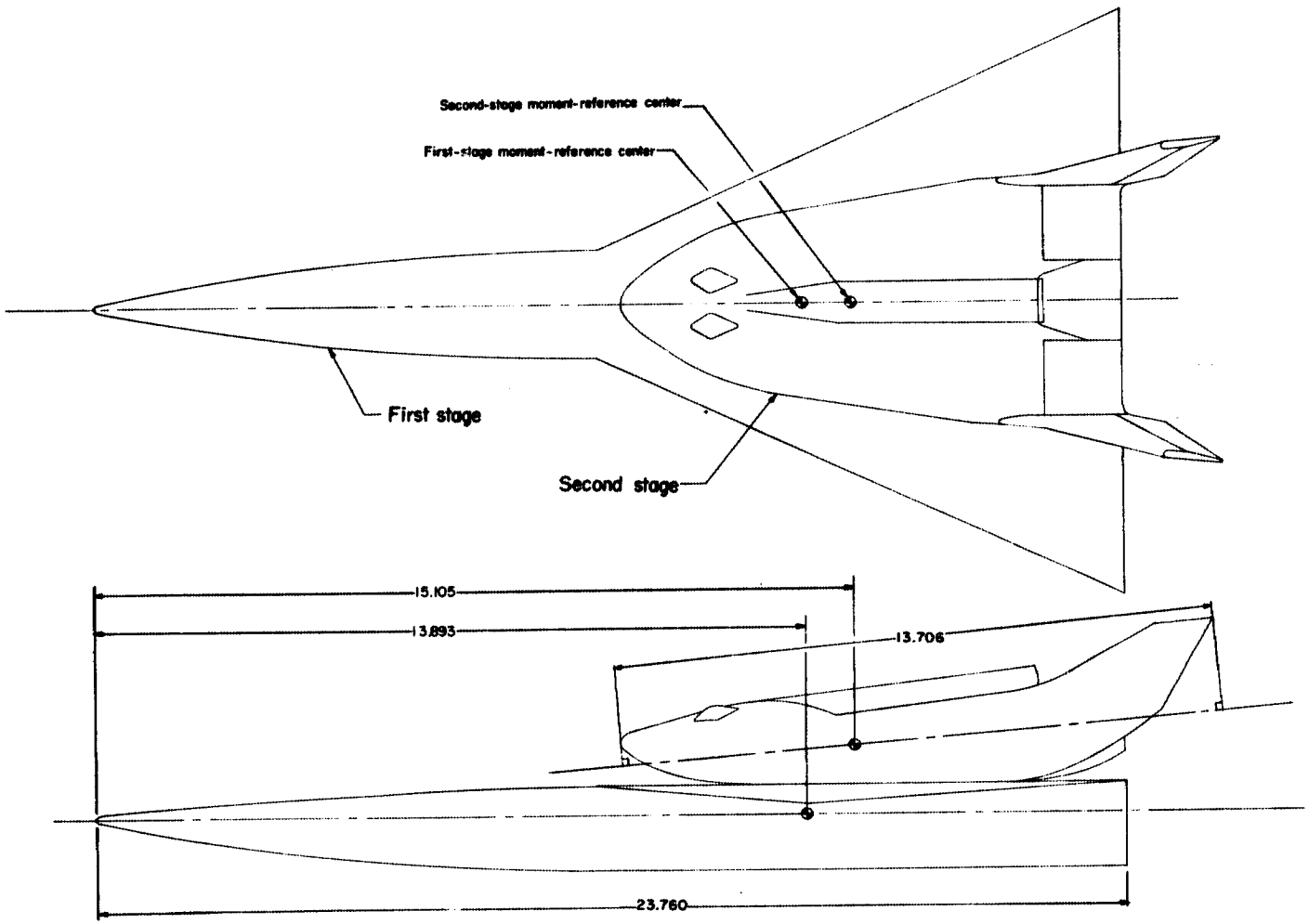

(a) Launch vehicle.

Figure 2.- Details of models. All dimensions are in inches.

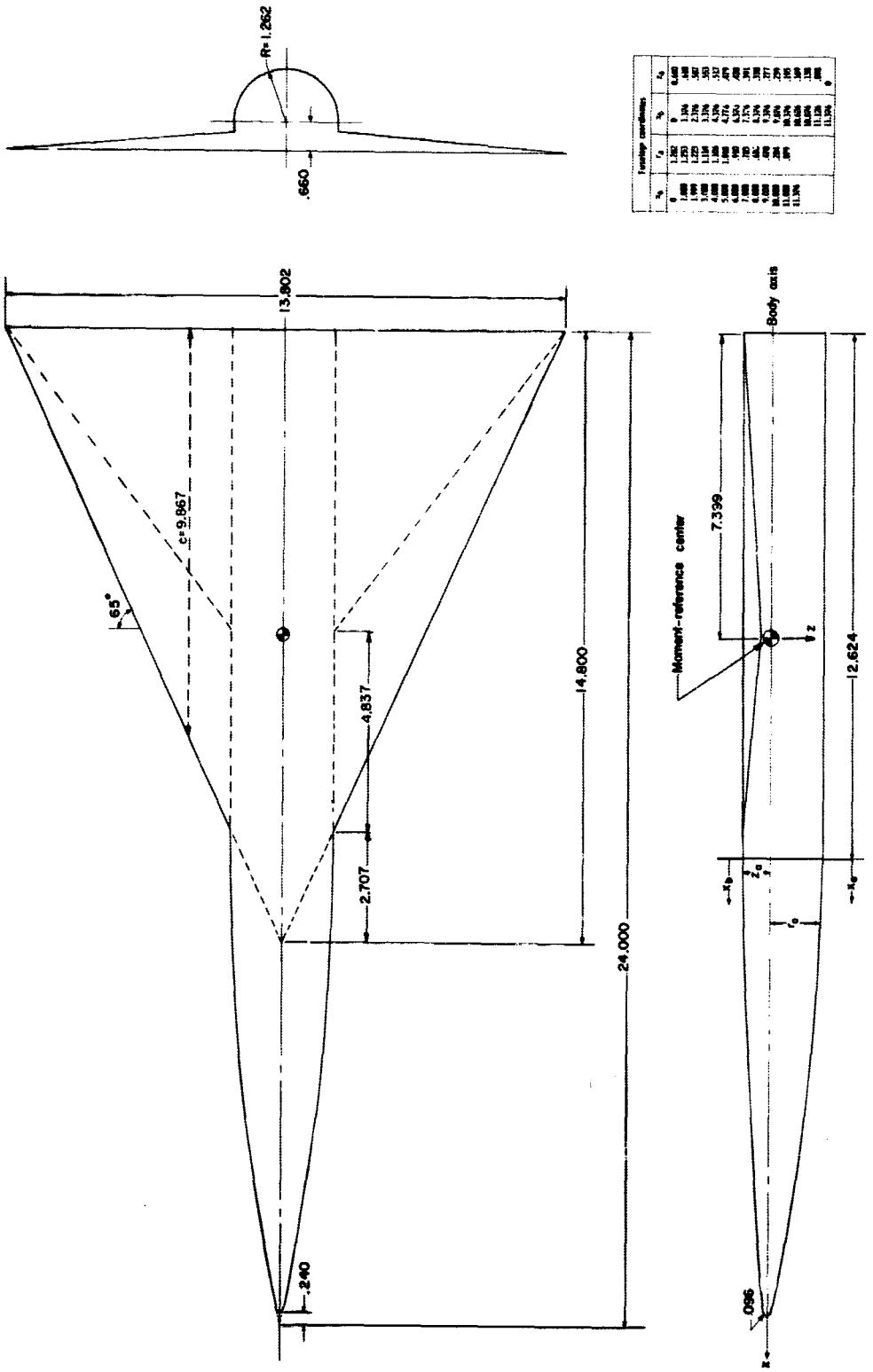

(b) First stage.

Figure 2.- Continued.

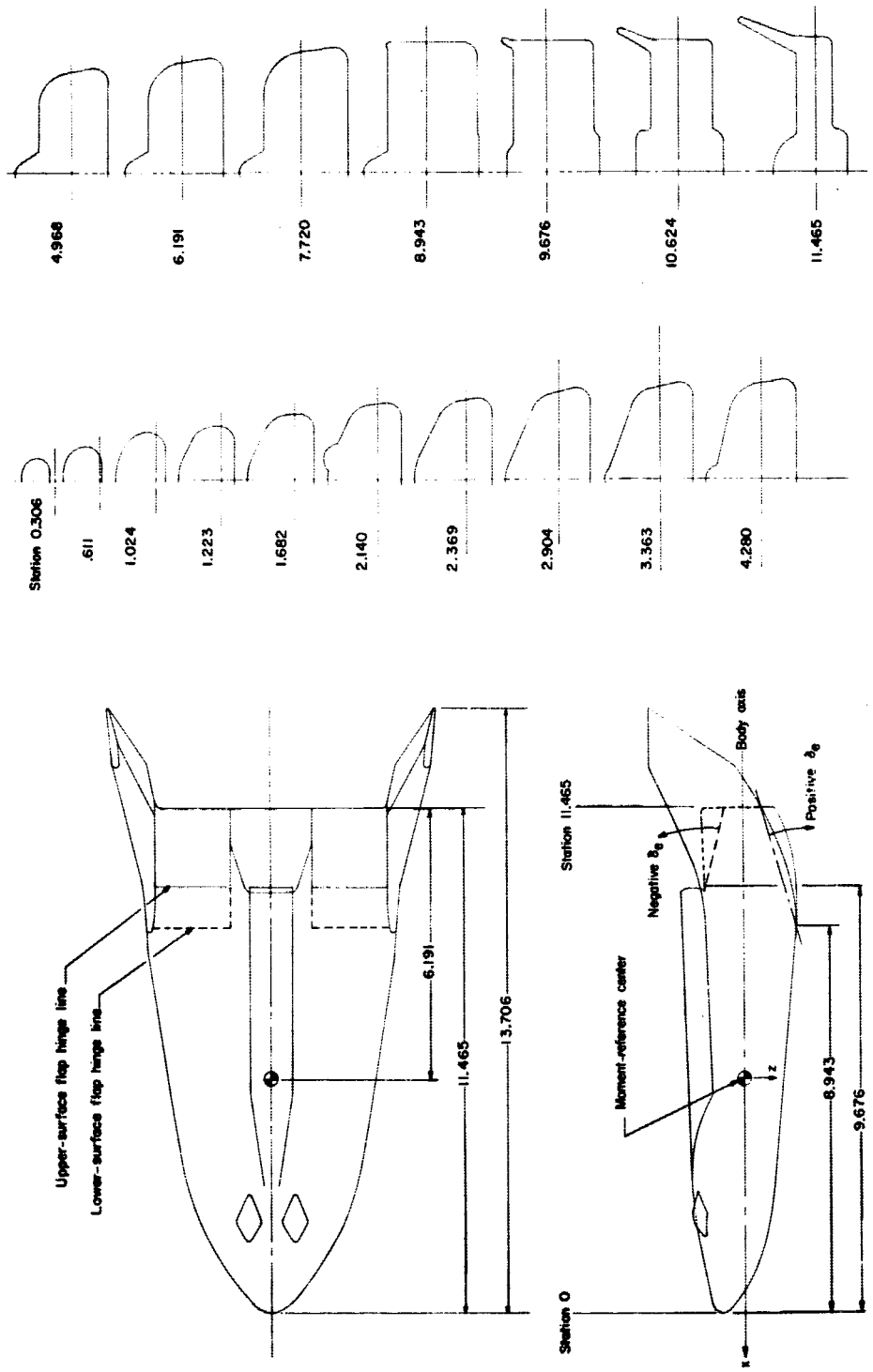

(c) Second stage.

Figure 2.- Concluded.

Figure ...- Photograph of support apparatus.

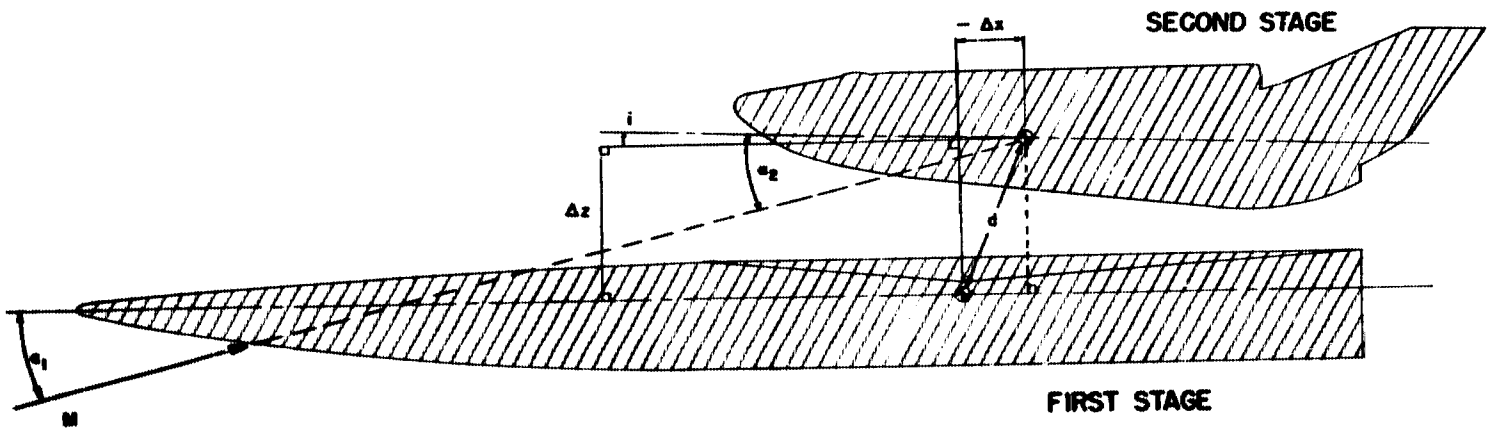

Figure 5.- Staging variables.

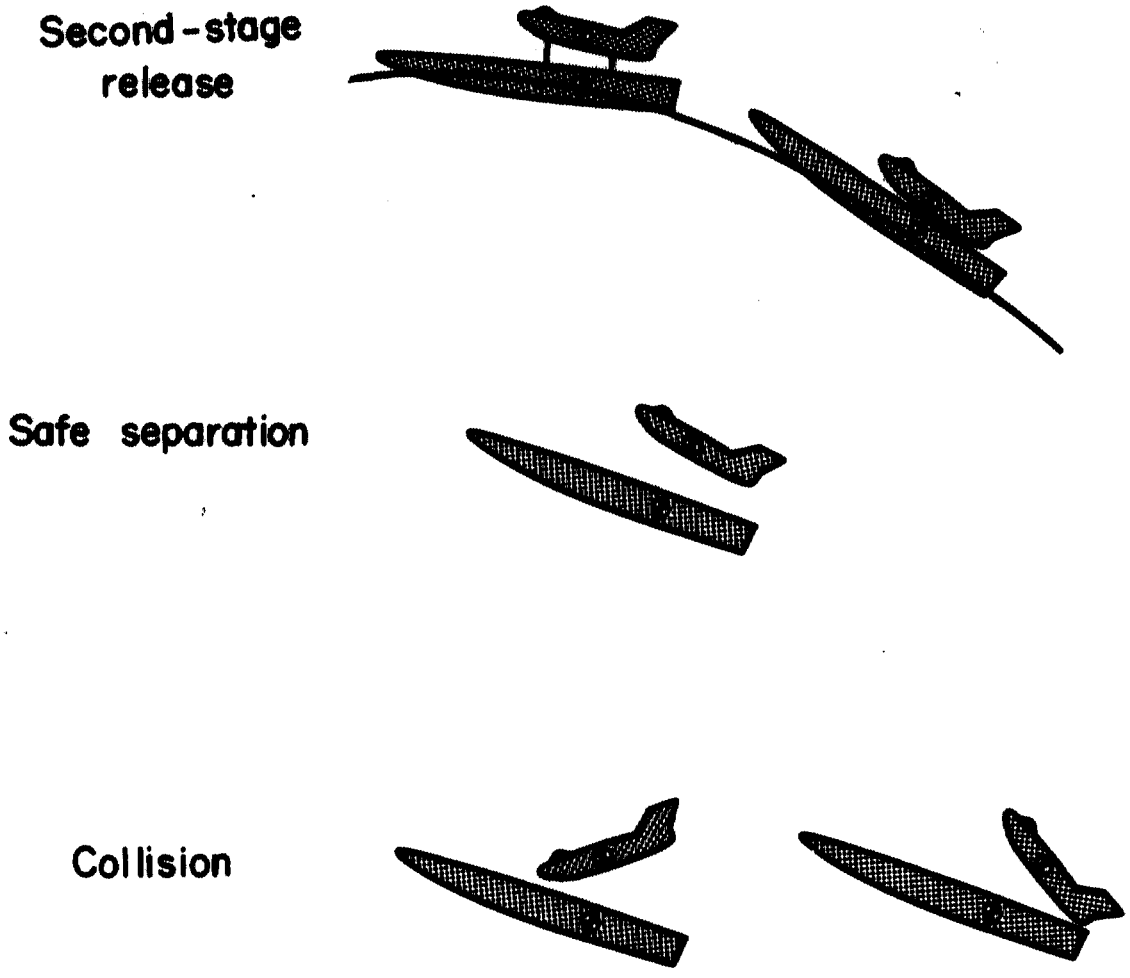

Figure 6.- Staging sequence.

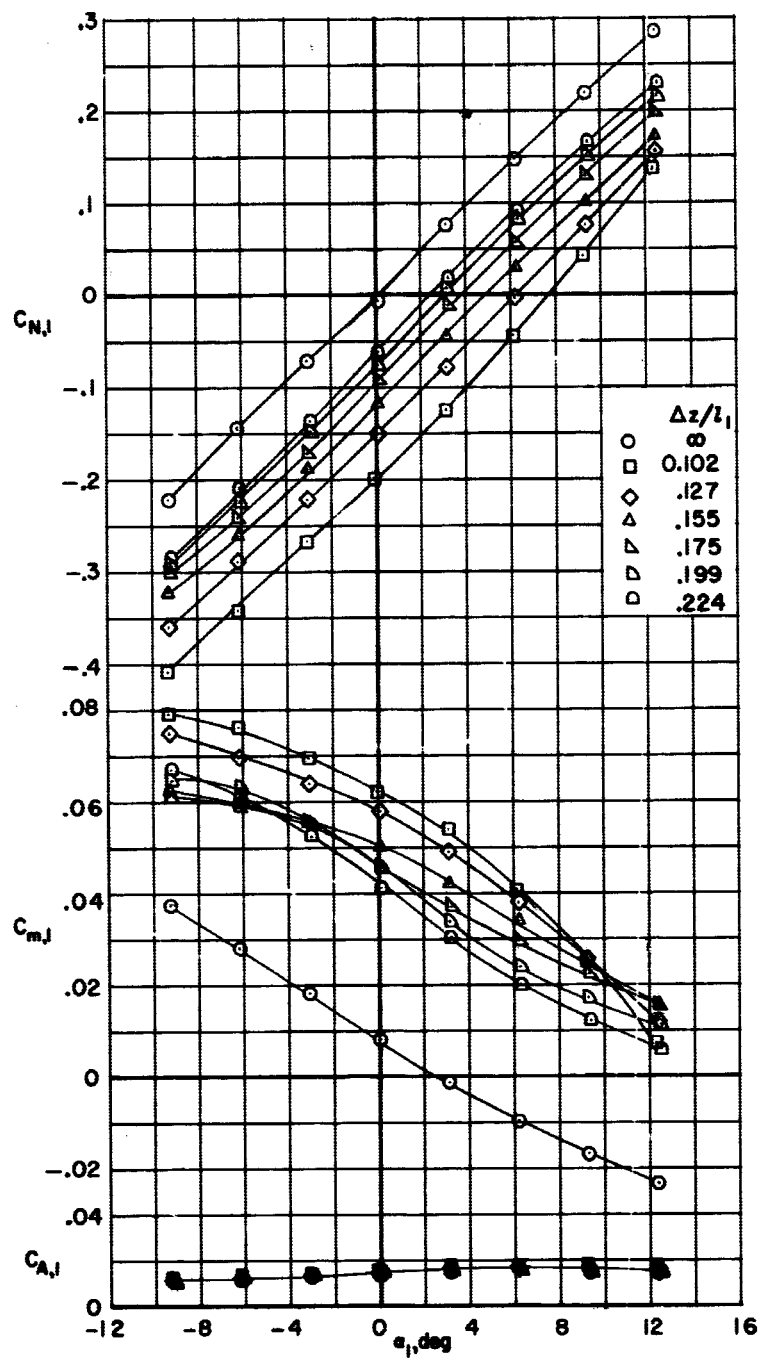

(a) $i = 0^{\circ}$; $\frac{\Delta x}{l_1} = -0.051$.

Figure 7.- Longitudinal aerodynamic characteristics of the first stage at a Mach number of 3.

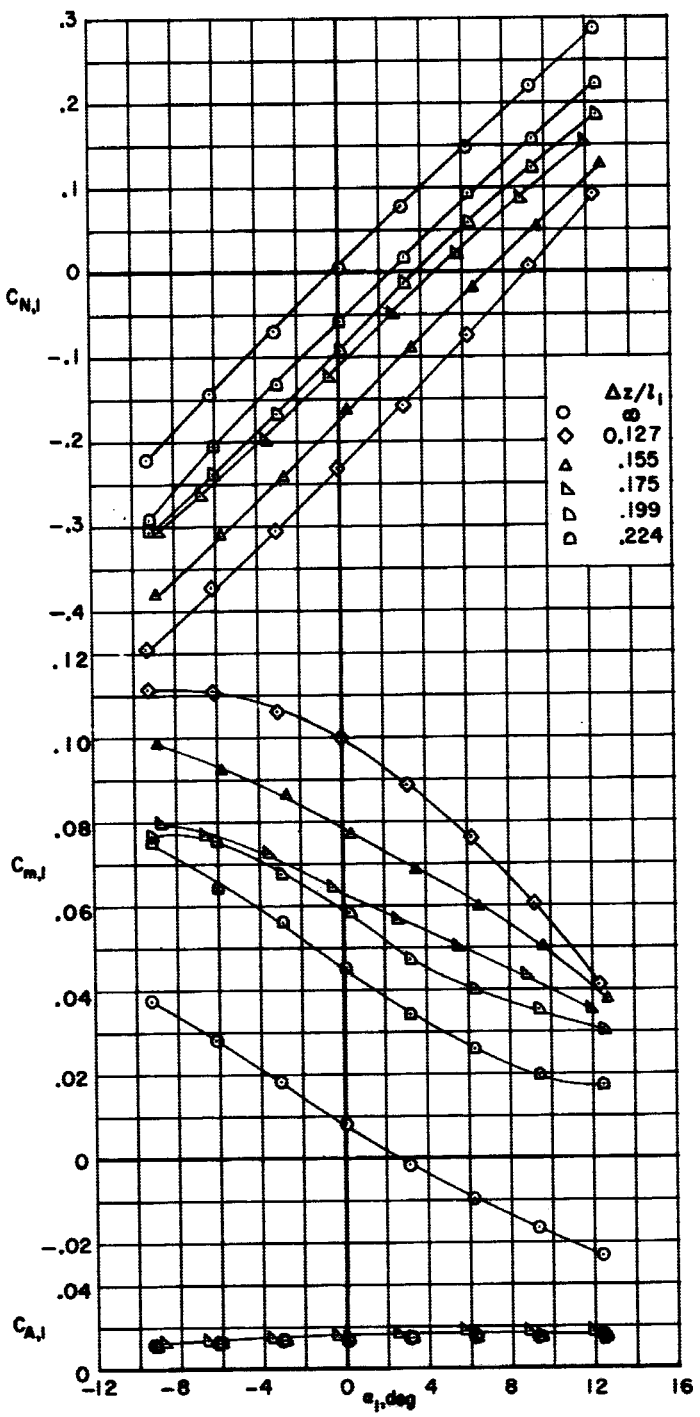

(b) $i = 5^\circ$; $\frac{\Delta x}{l_1} = -0.051$.

Figure 7.- Continued.

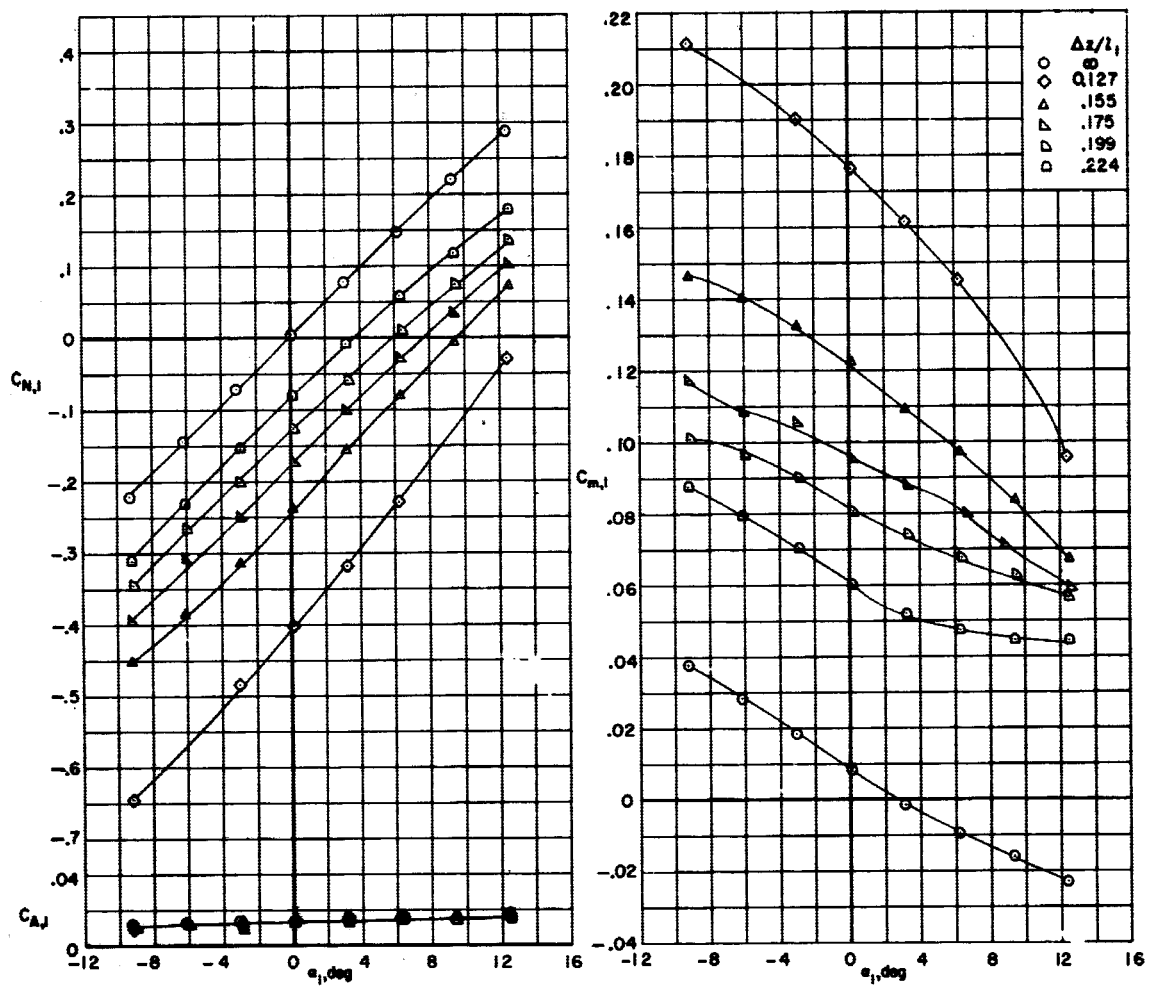

(c) $i = 10^\circ$; $\frac{\overline{\Delta x}}{l_1} = -0.051$.

Figure 7.- Continued.

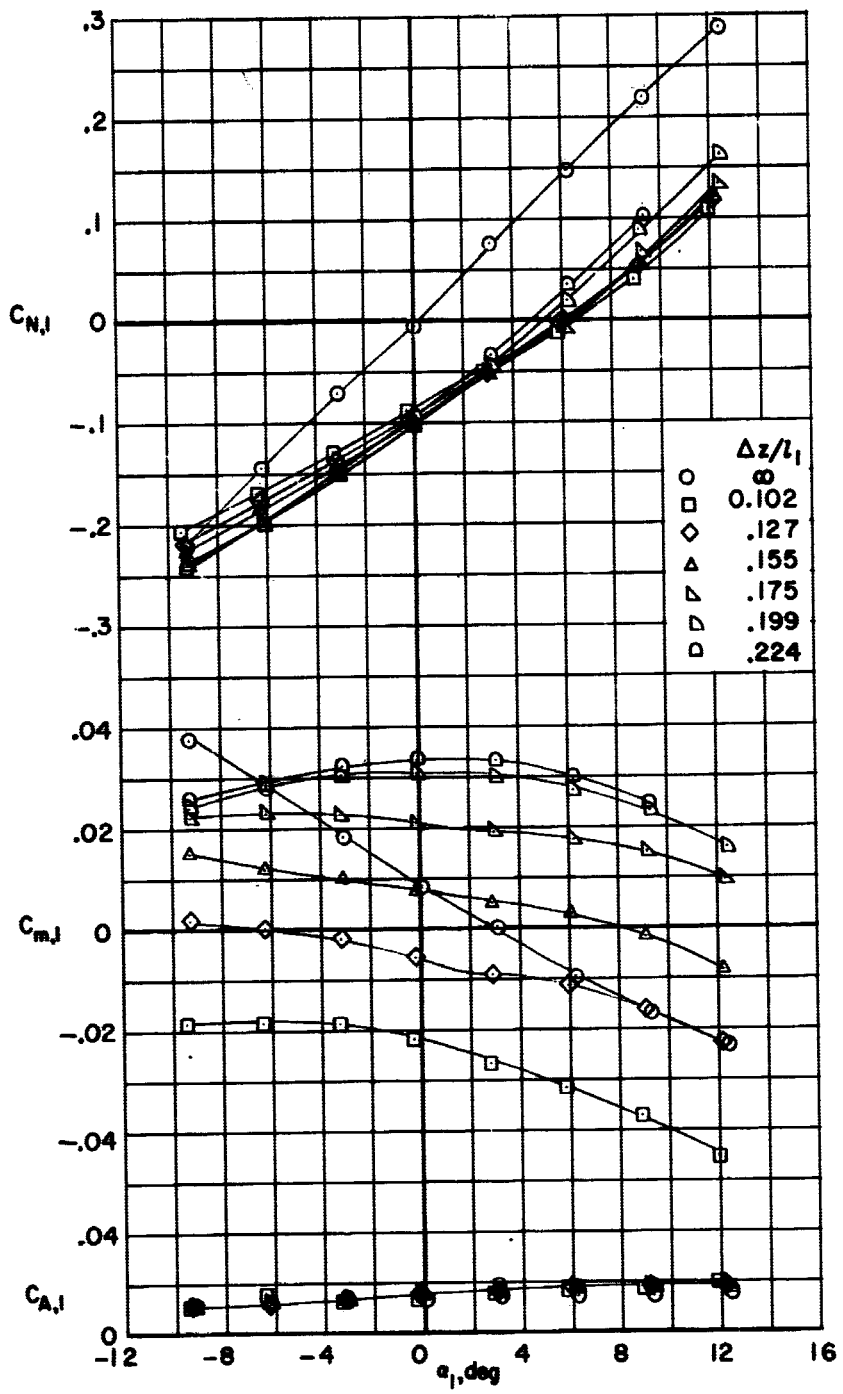

(d) $i = 0^\circ$; $\frac{\Delta x}{l_1} = 0.160$.

Figure 7.- Continued.

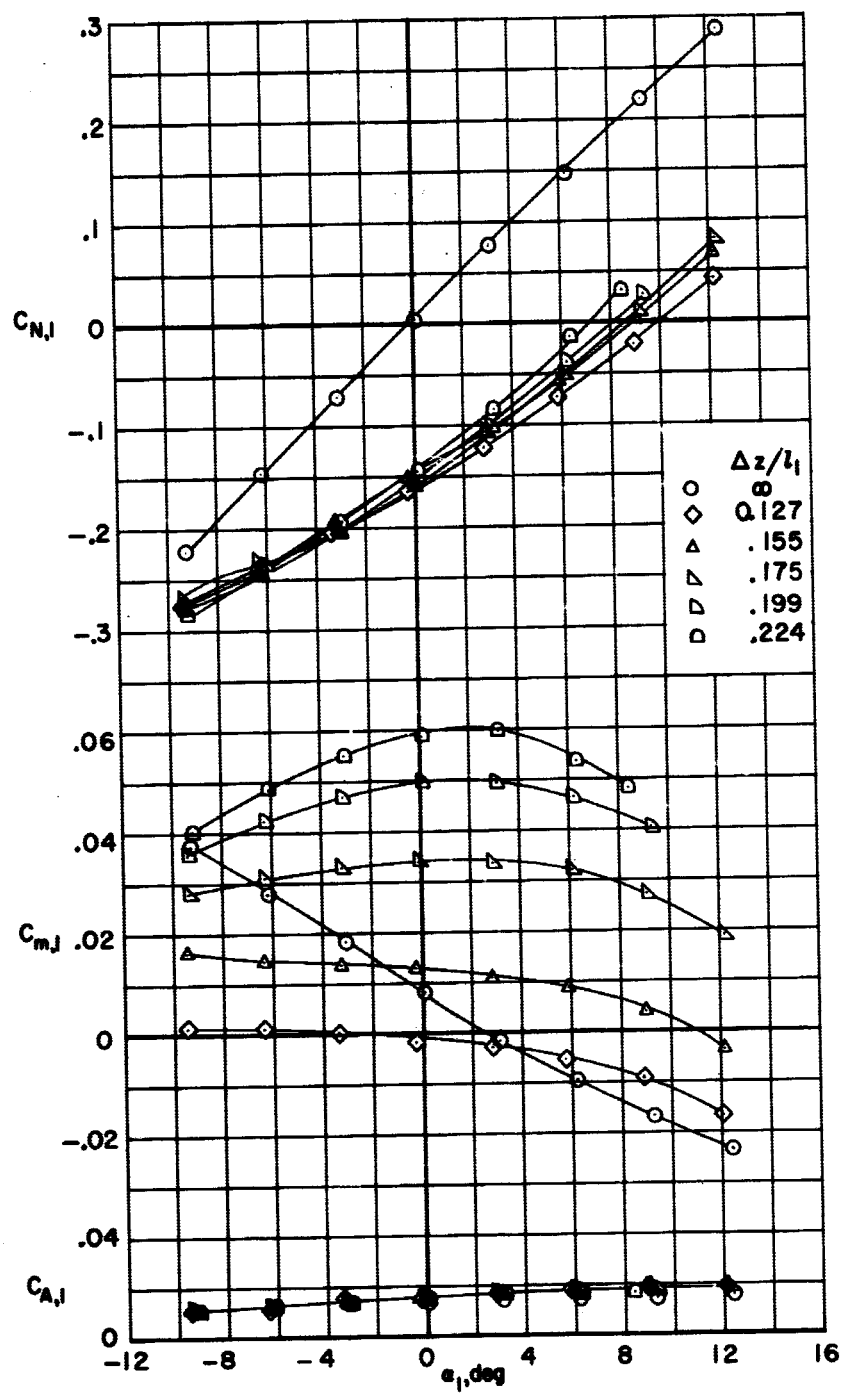

(e) $i = 5^\circ$; $\frac{\Delta x}{l_1} = 0.160$.

Figure 7.- Continued.

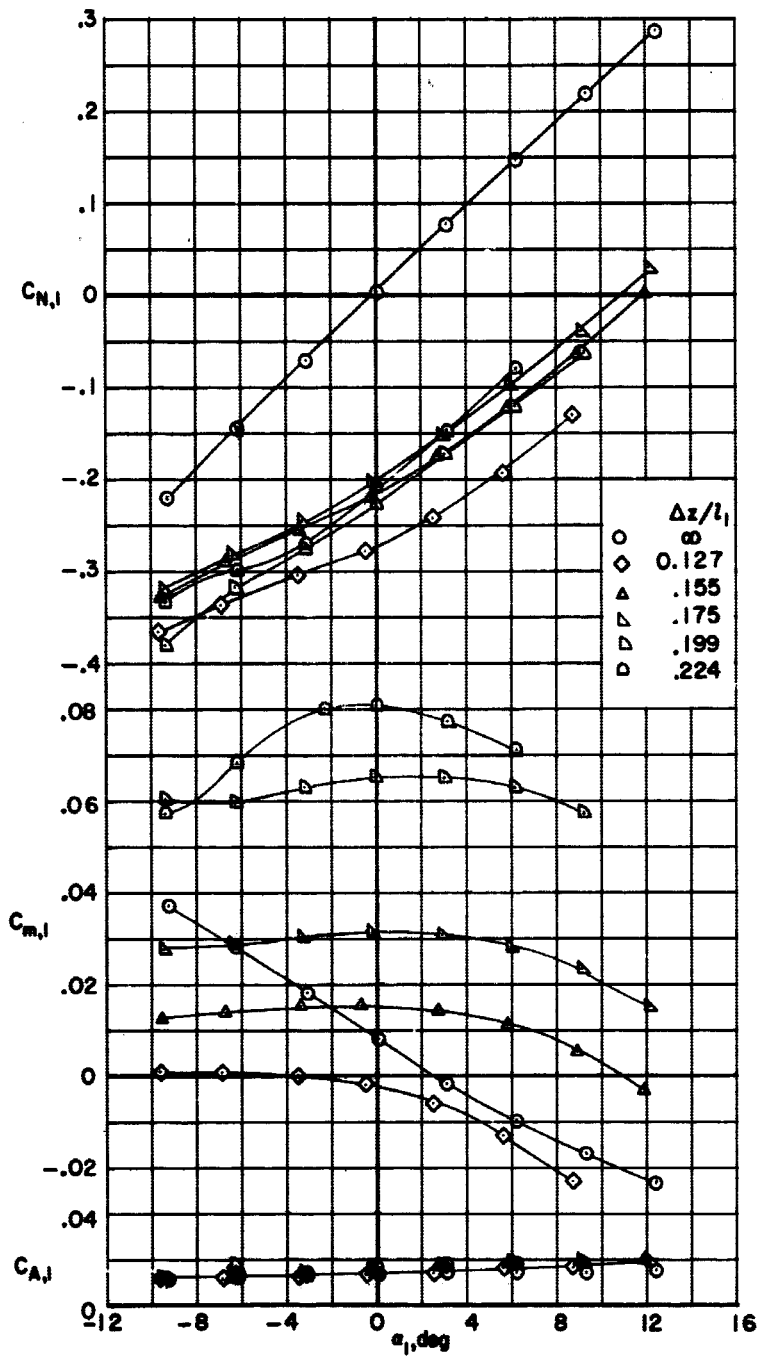

(f) $i = 10^{\circ}$; $\frac{\Delta x}{l_1} = 0.160$.

Figure 7.- Concluded.

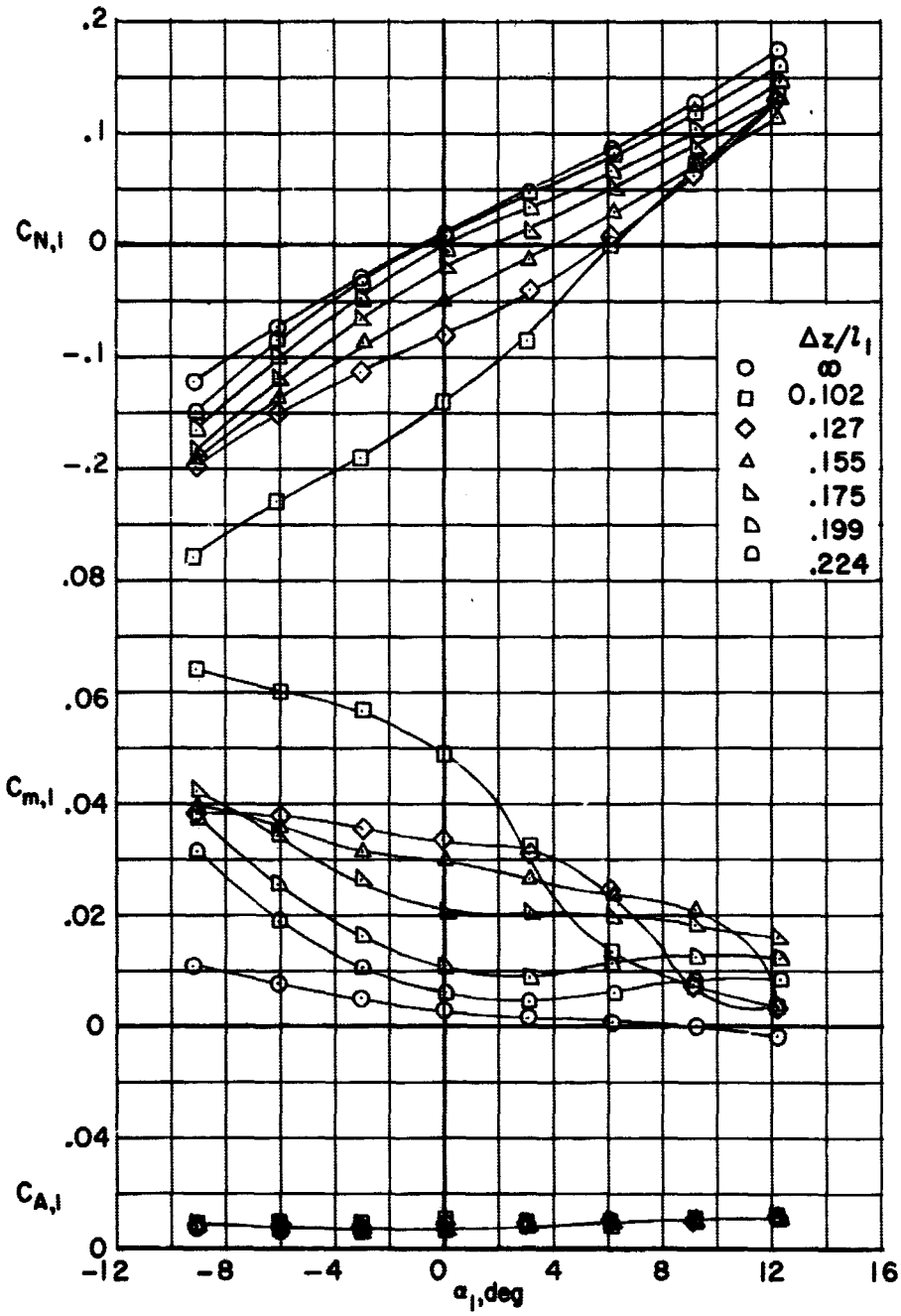

(a) $i = 0^\circ$; $\frac{\Delta x}{l_1} = -0.051$.

Figure 8.- Longitudinal aerodynamic characteristics of the first stage at a Mach number of 6.

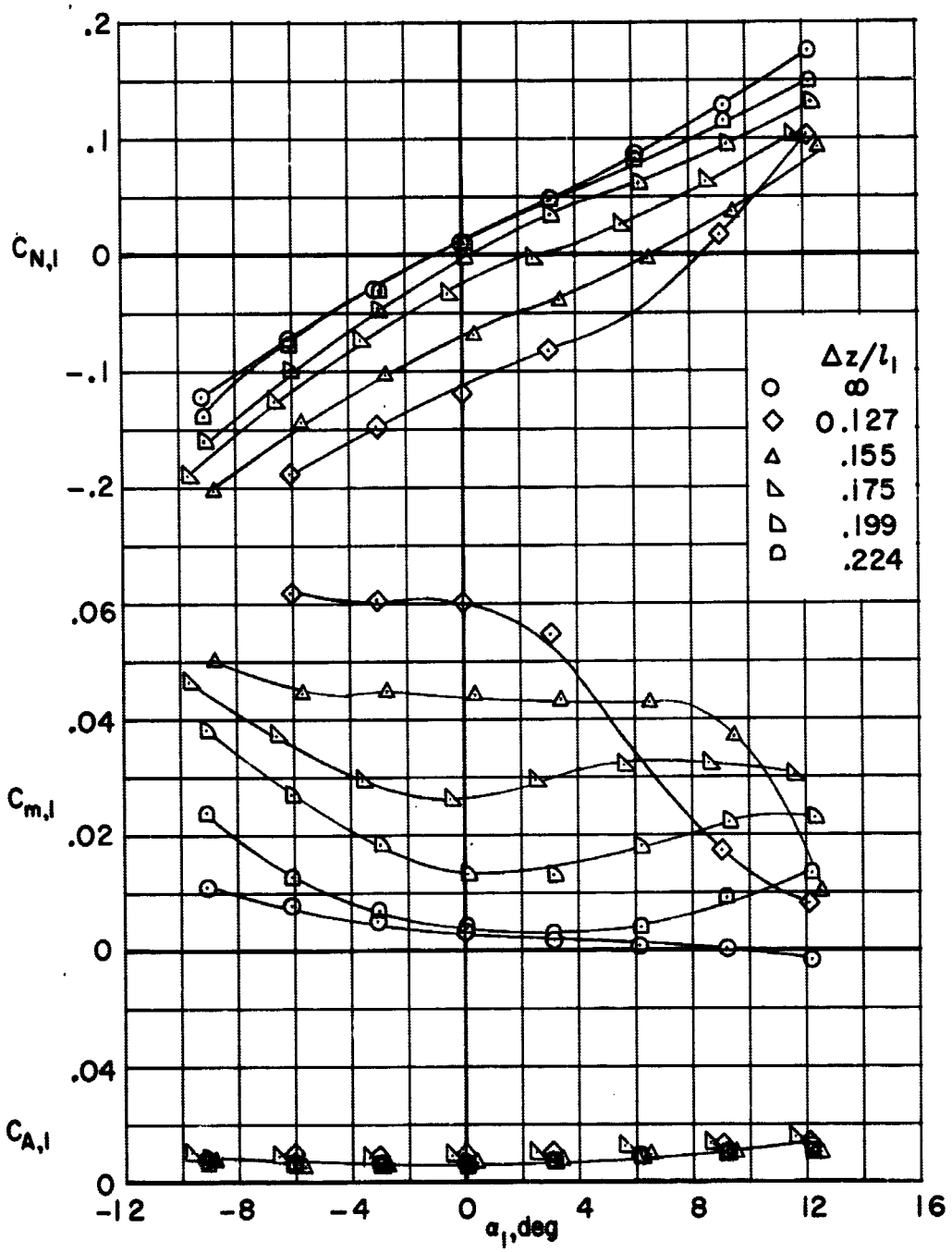

(b) $i = 5°$; $\frac{\Delta z}{l_1} = -0.051$.

Figure 8.- Continued.

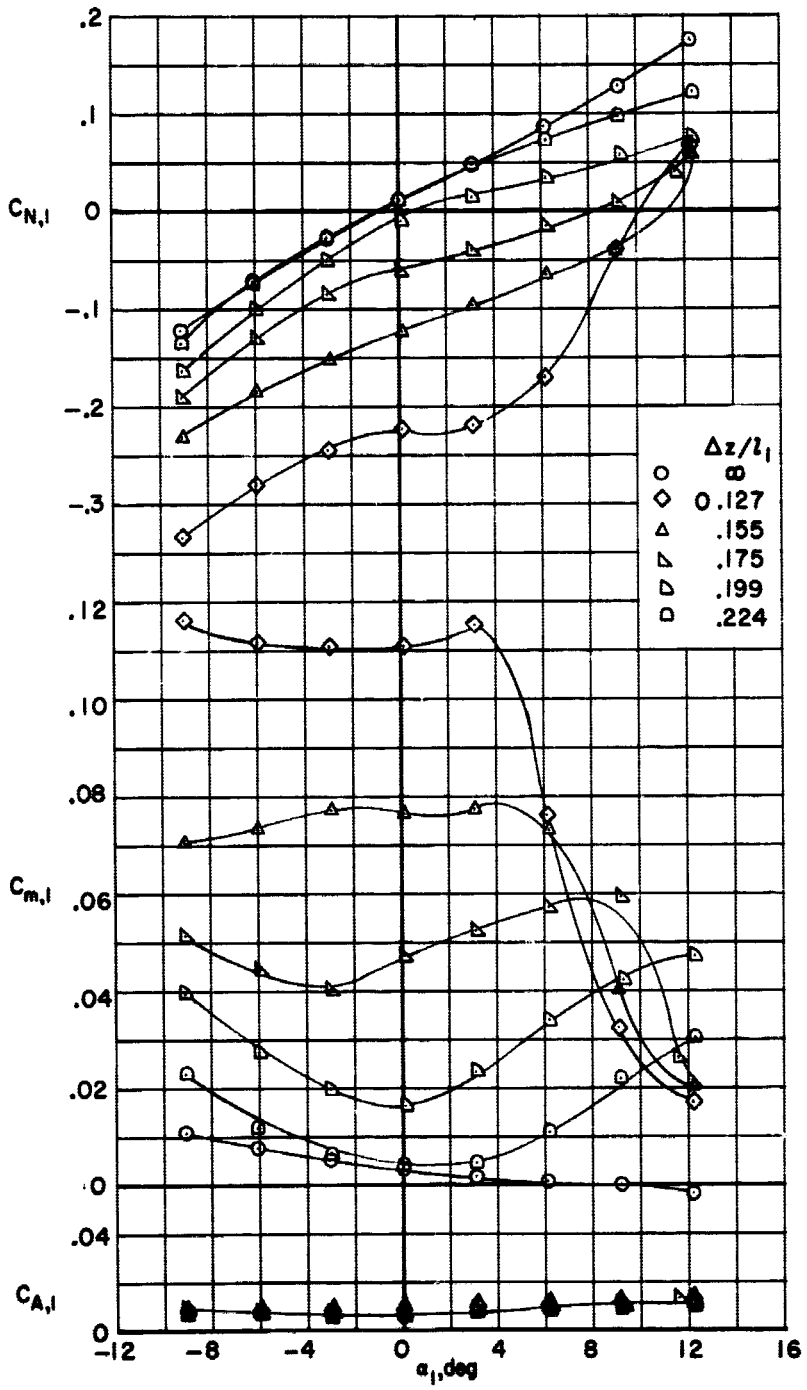

(c) $i = 10^\circ$; $\frac{\Delta x}{l_1} = -0.051$.

Figure 8.- Continued.

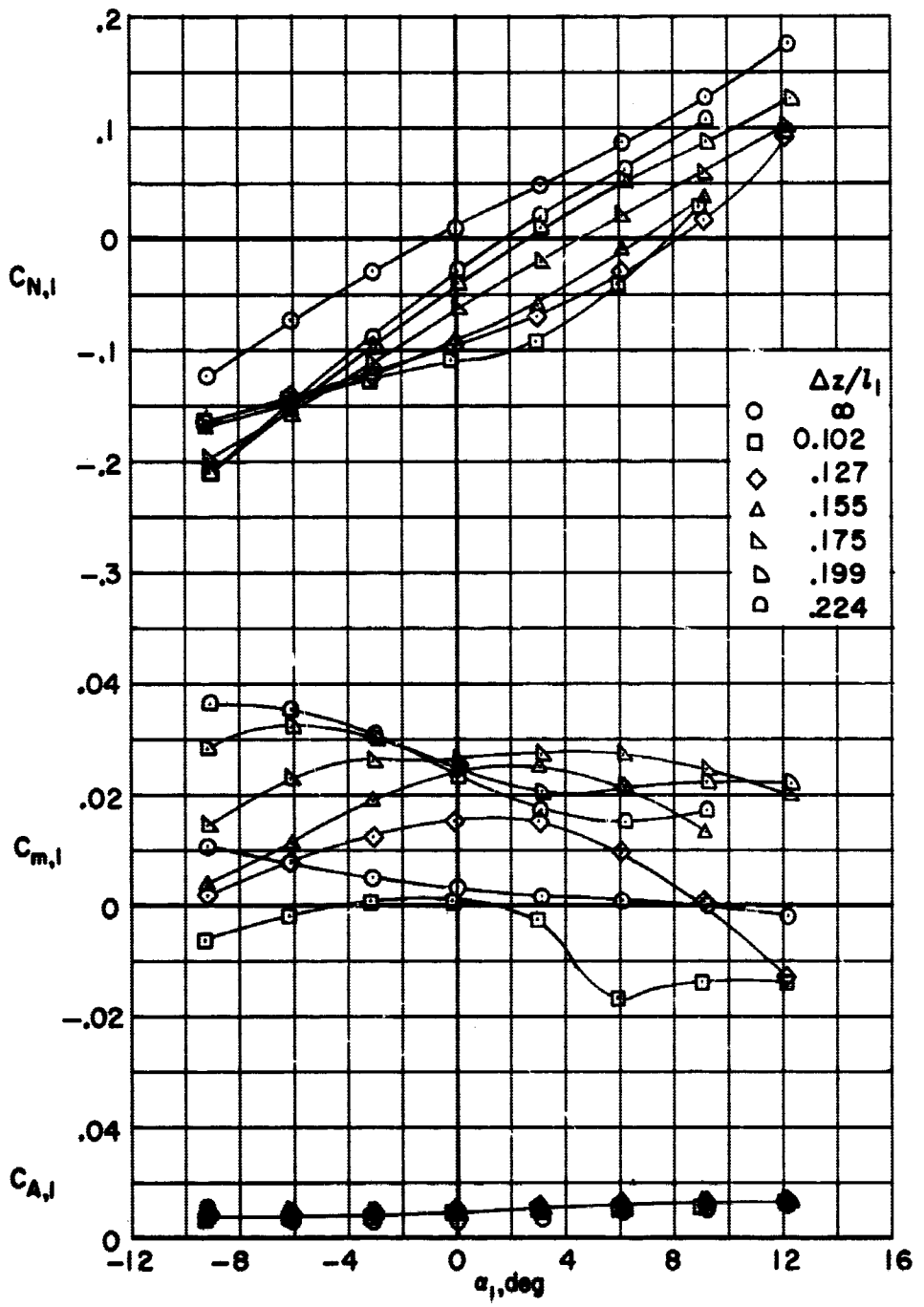

(d) $i = 0°$; $\frac{\Delta x}{l_l} = 0.160$.

Figure 8.- Continued.

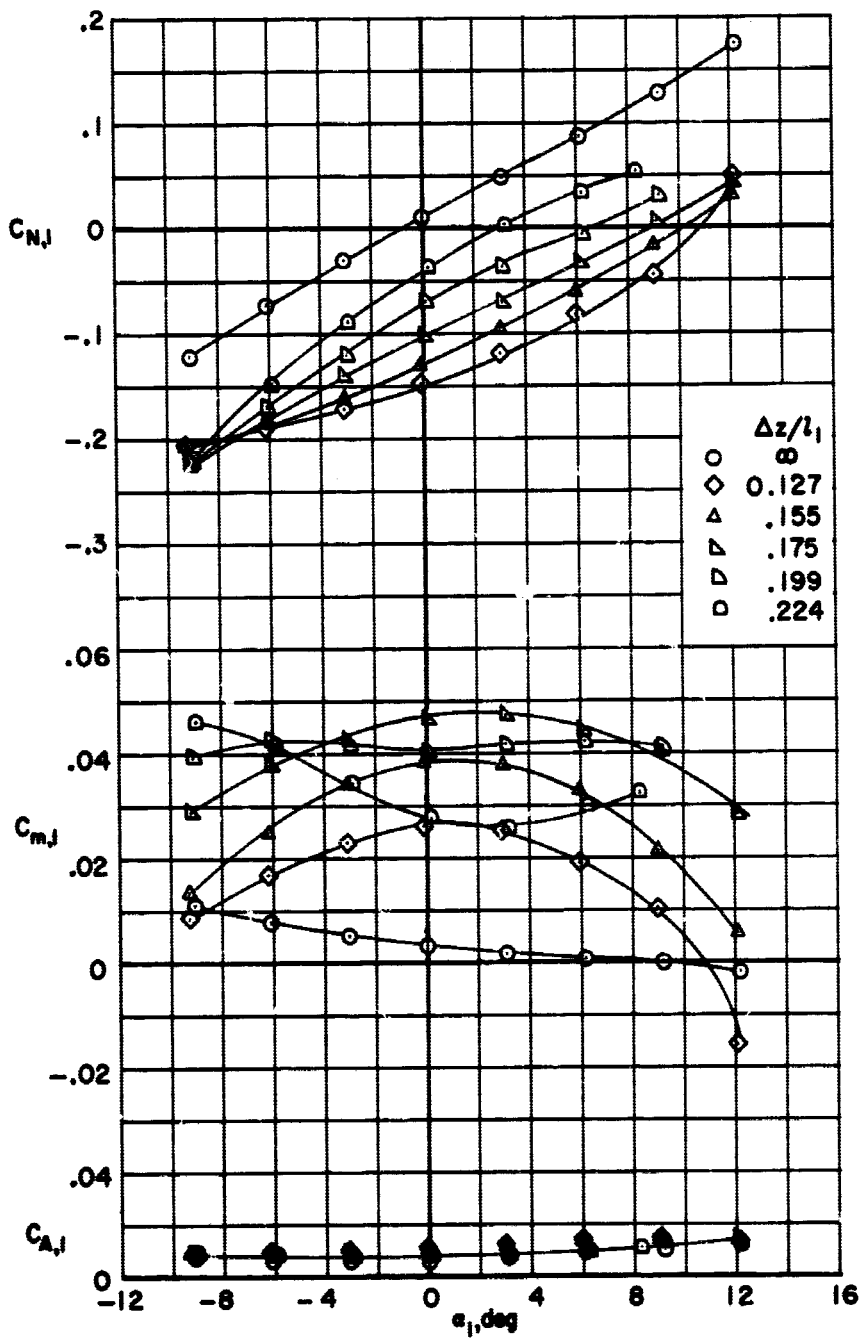

(e) $i = 5°$; $\frac{\Delta x}{l_1} = 0.160$.

Figure 8.- Continued.

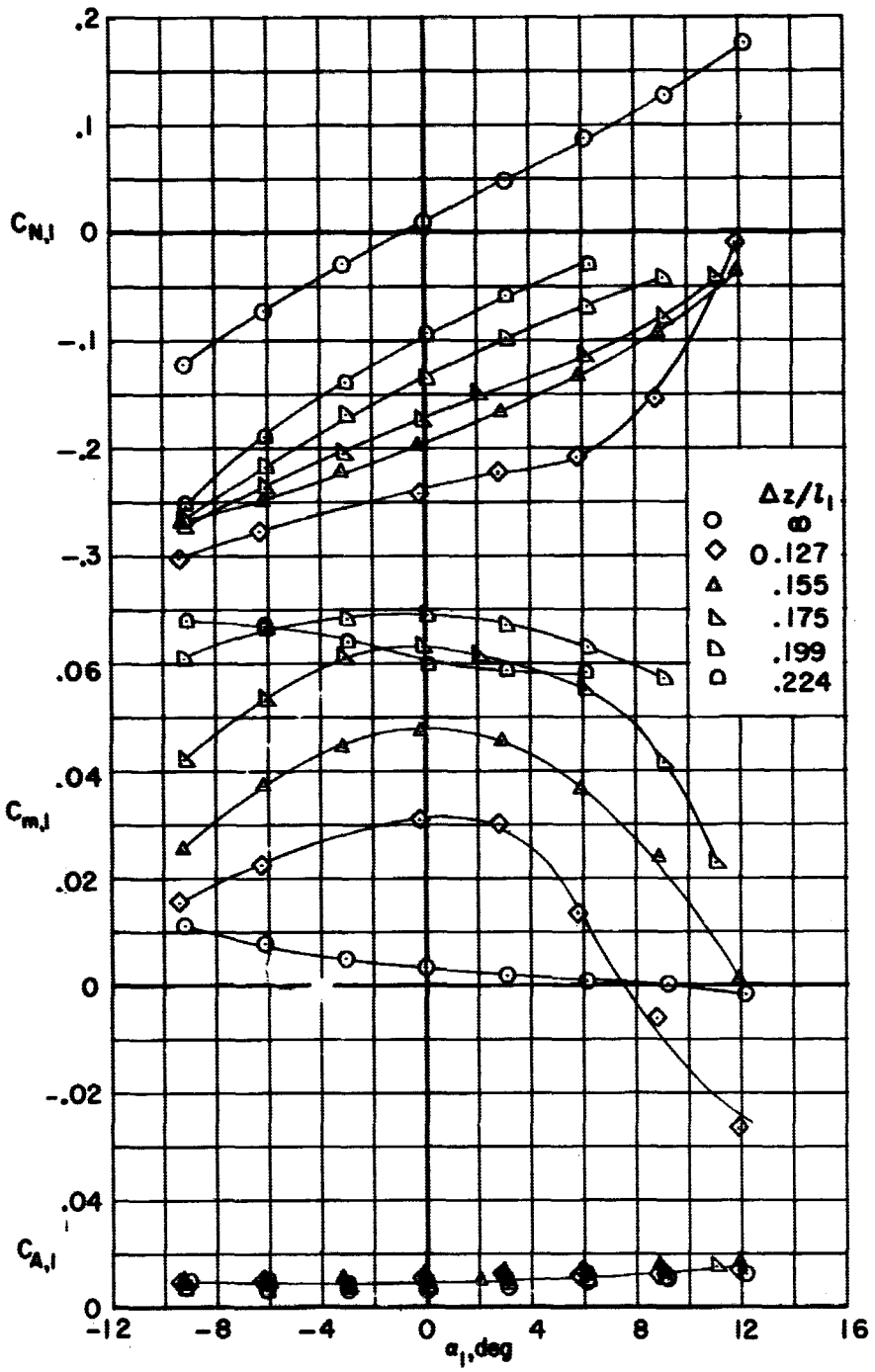

(f) $i = 10^\circ$; $\frac{\Delta x}{l_1} = 0.160$.

Figure 8.- Concluded.

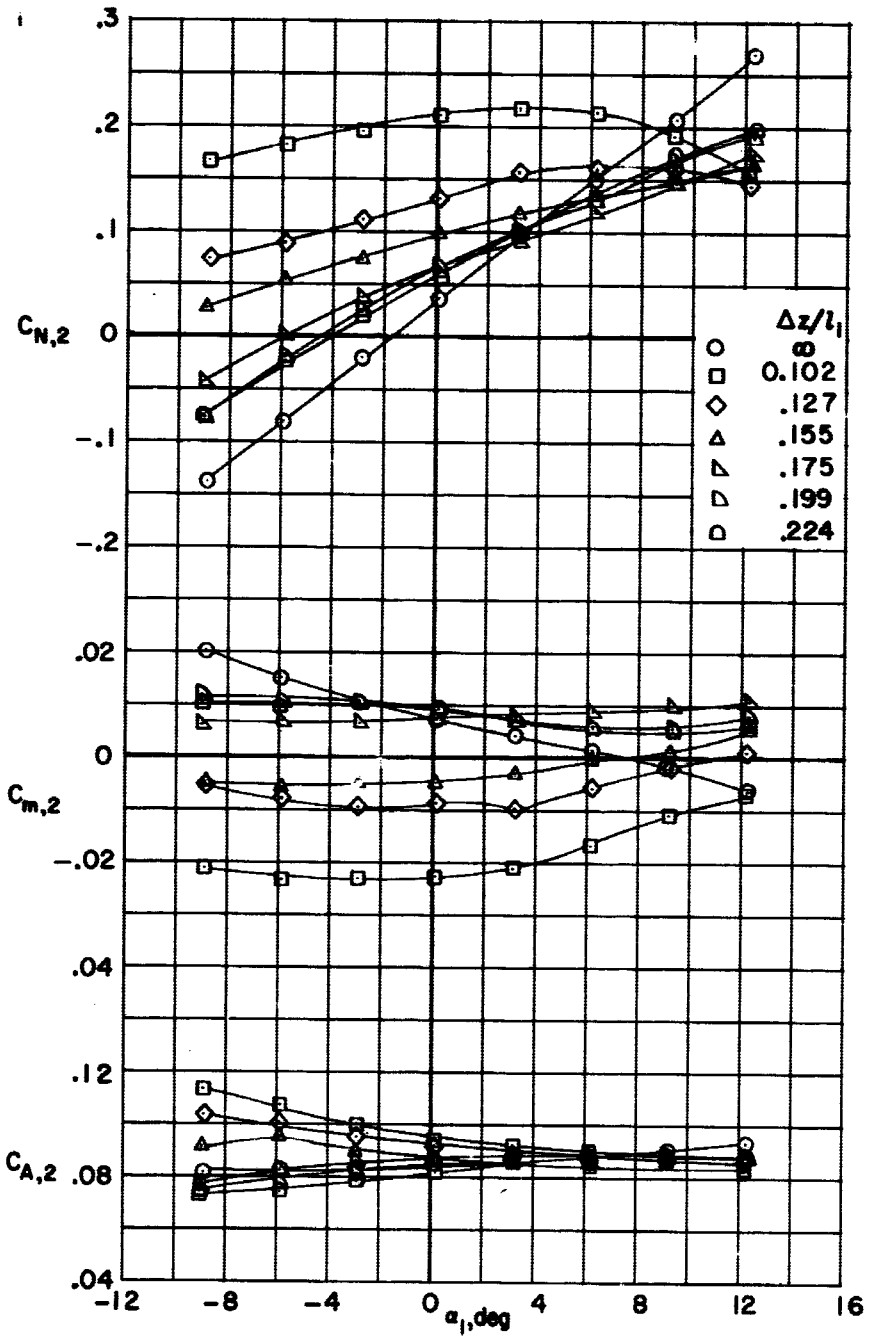

(a) $i = 0^\circ$; $\frac{\Delta x}{l_1} = -0.051$.

Figure 9.- Longitudinal aerodynamic characteristics of the second stage at a Mach number of 3.

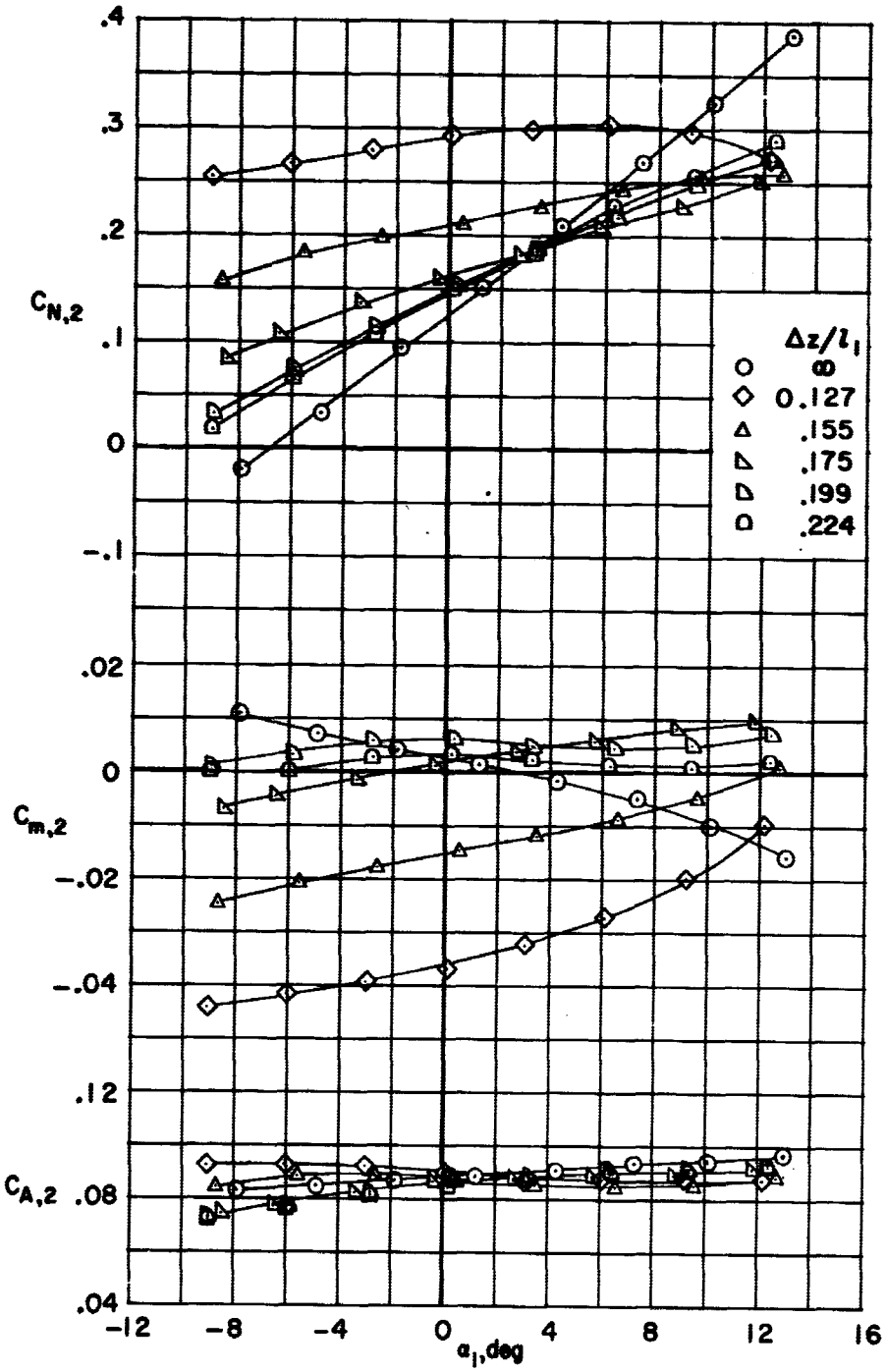

(b) $i = 5°$; $\frac{\Delta x}{l_1} = -0.051$.

Figure 9.- Continued.

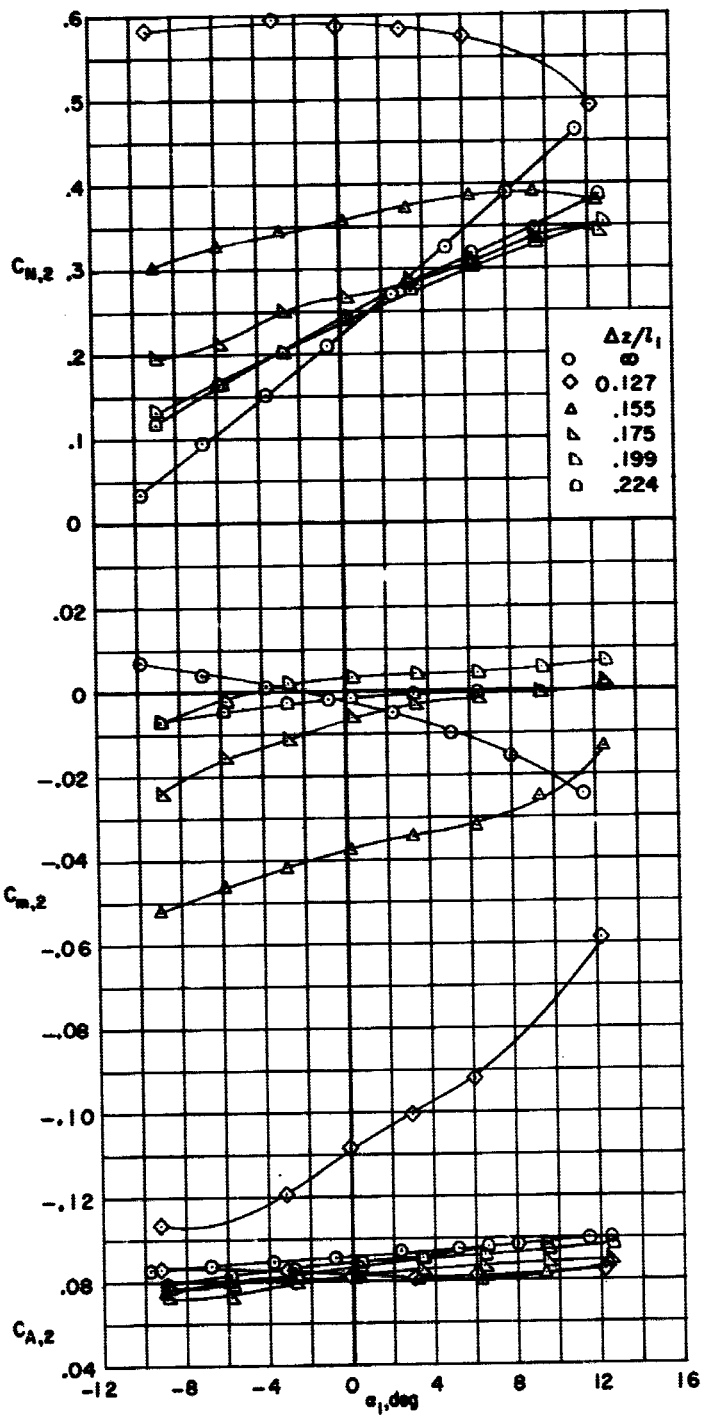

(c) $i = 10^{\circ}$; $\frac{\Delta x}{l_1} = -0.051$.

Figure 9.- Continued.

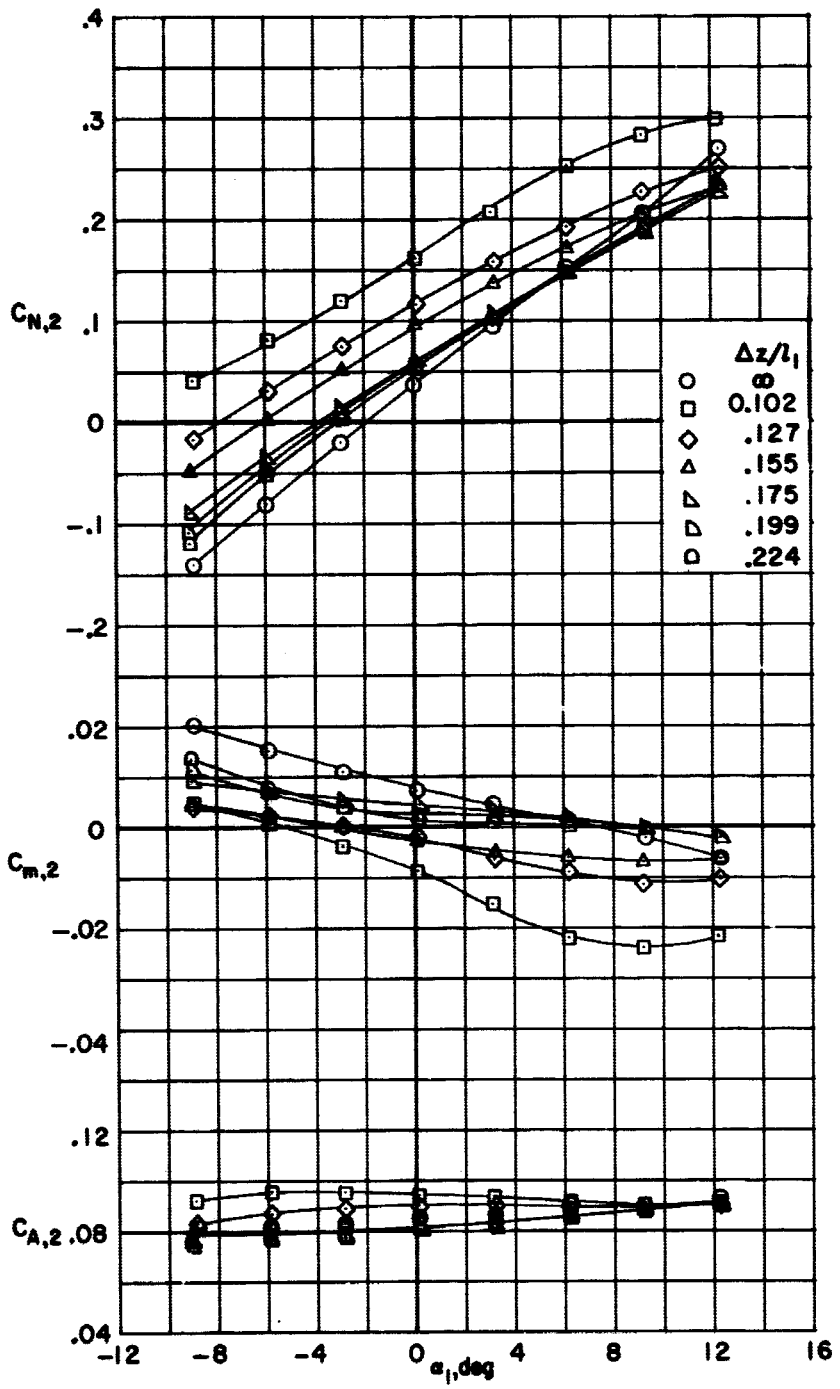

(d) $i = 0°$; $\frac{\Delta x}{l_1} = 0.160$.

Figure 9.- Continued.

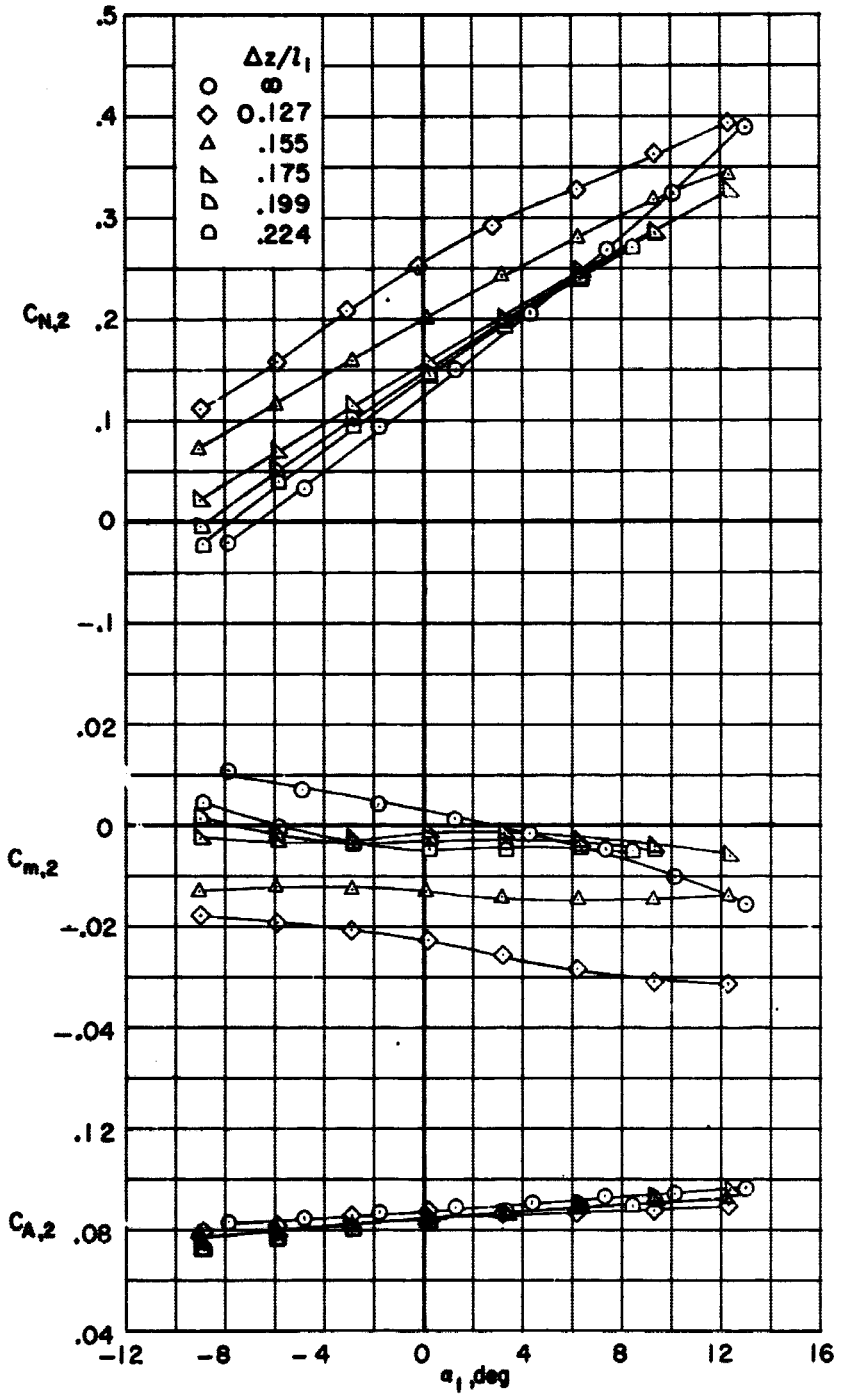

(e) $i = 5°$; $\frac{\Delta x}{l_1} = 0.160$.

Figure 9.- Continued

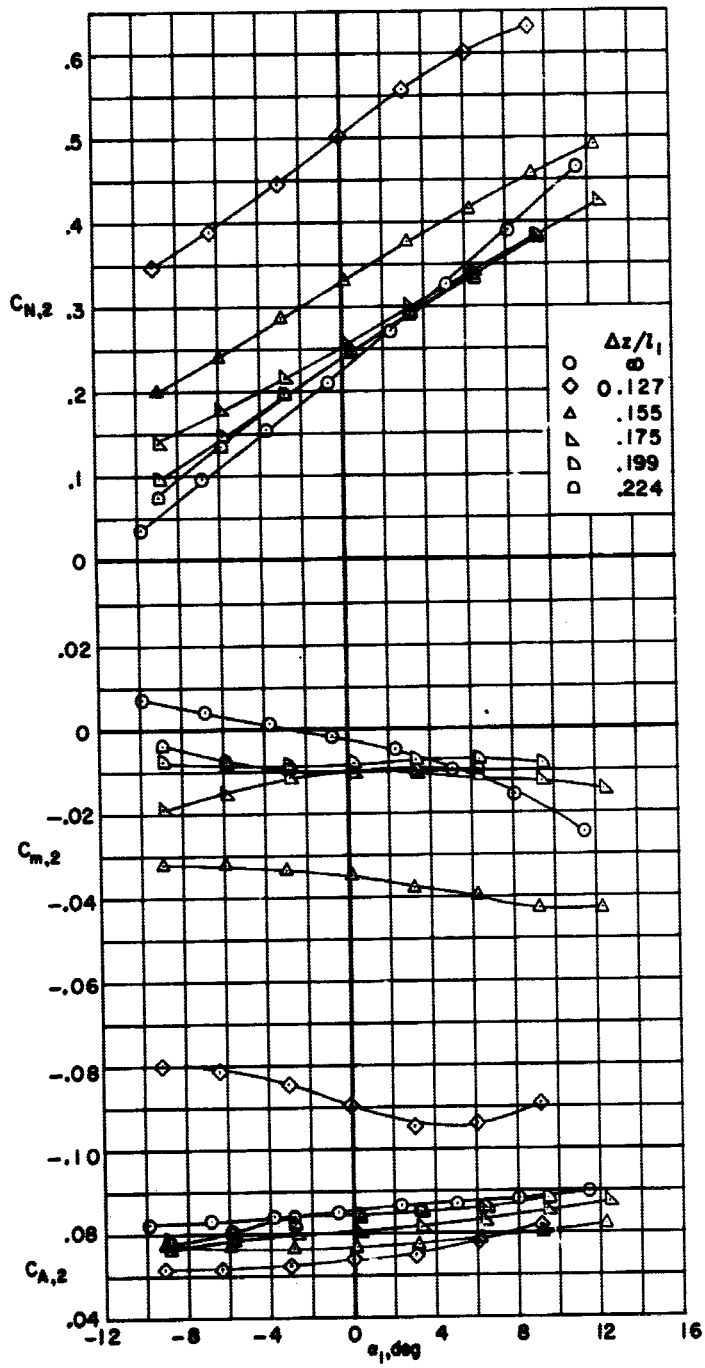

(f) $i = 10°$; $\frac{\Delta x}{l_1} = 0.160$.

Figure 9.- Concluded.

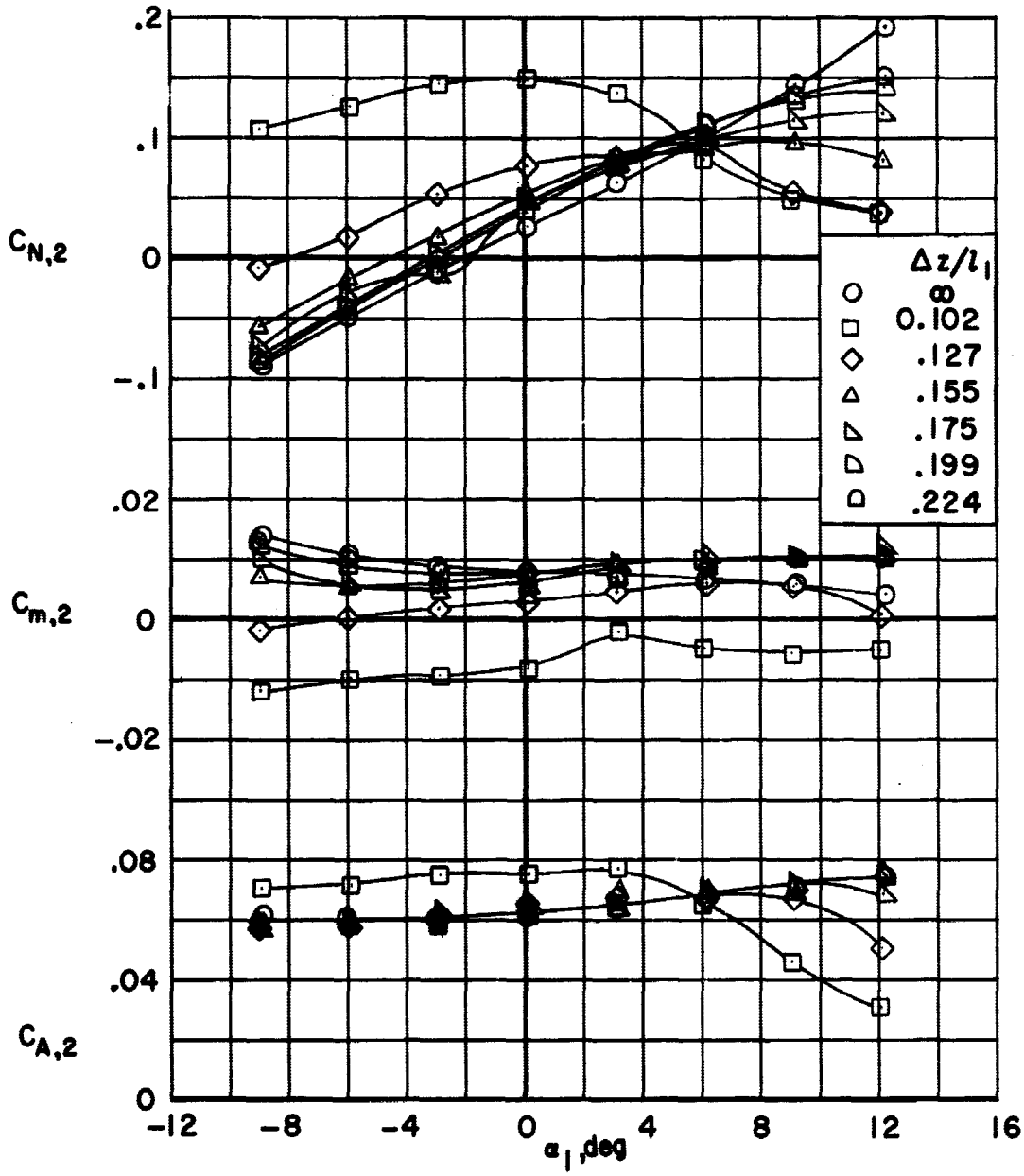

(a) $i = 0°$; $\frac{\Delta x}{l_1} = -0.051$.

Figure 10.- Longitudinal aerodynamic characteristics of the second stage at a Mach number of 6.

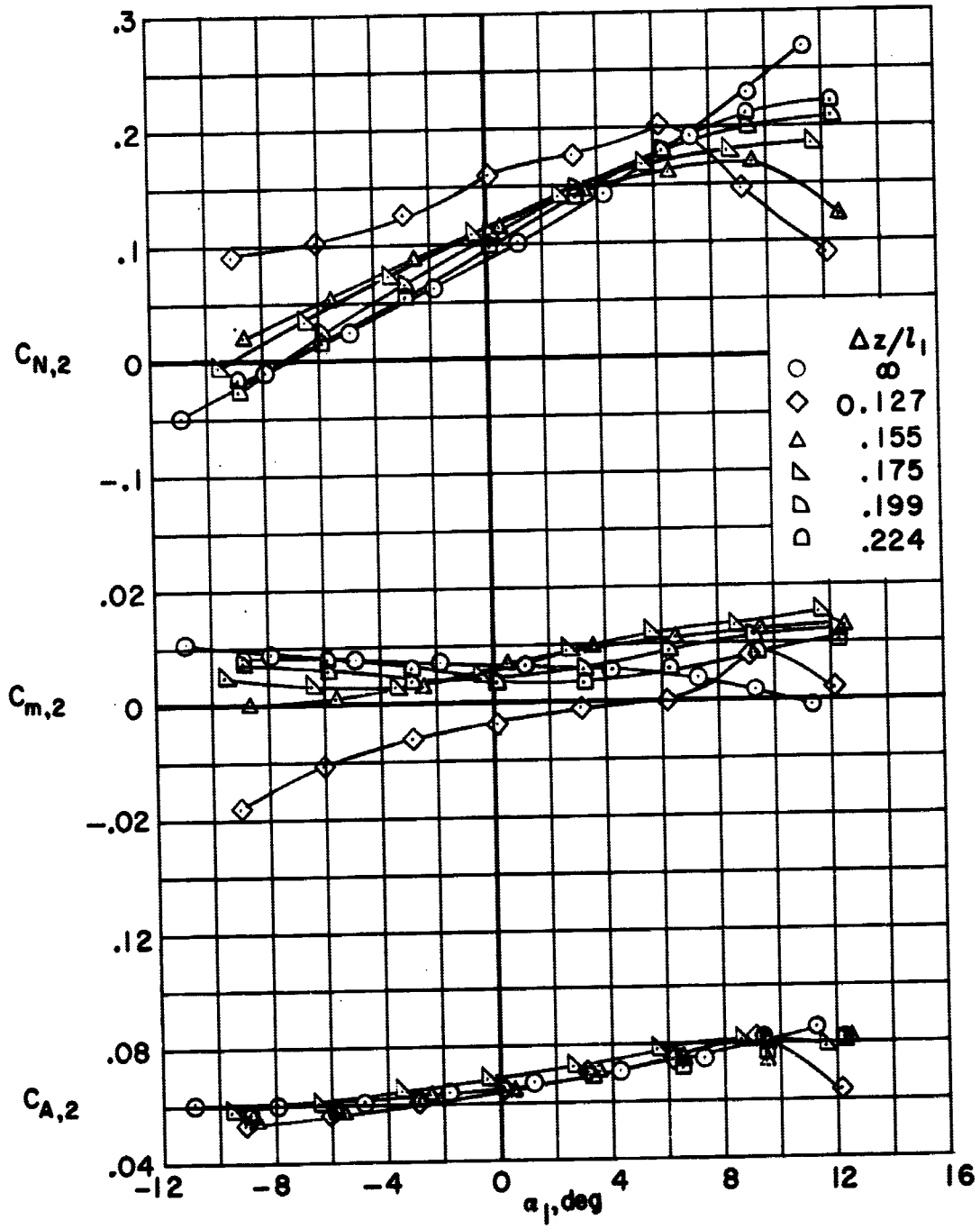

(b) $i = 5°$; $\frac{\Delta x}{l_1} = -0.051$.

Figure 10.- Continued.

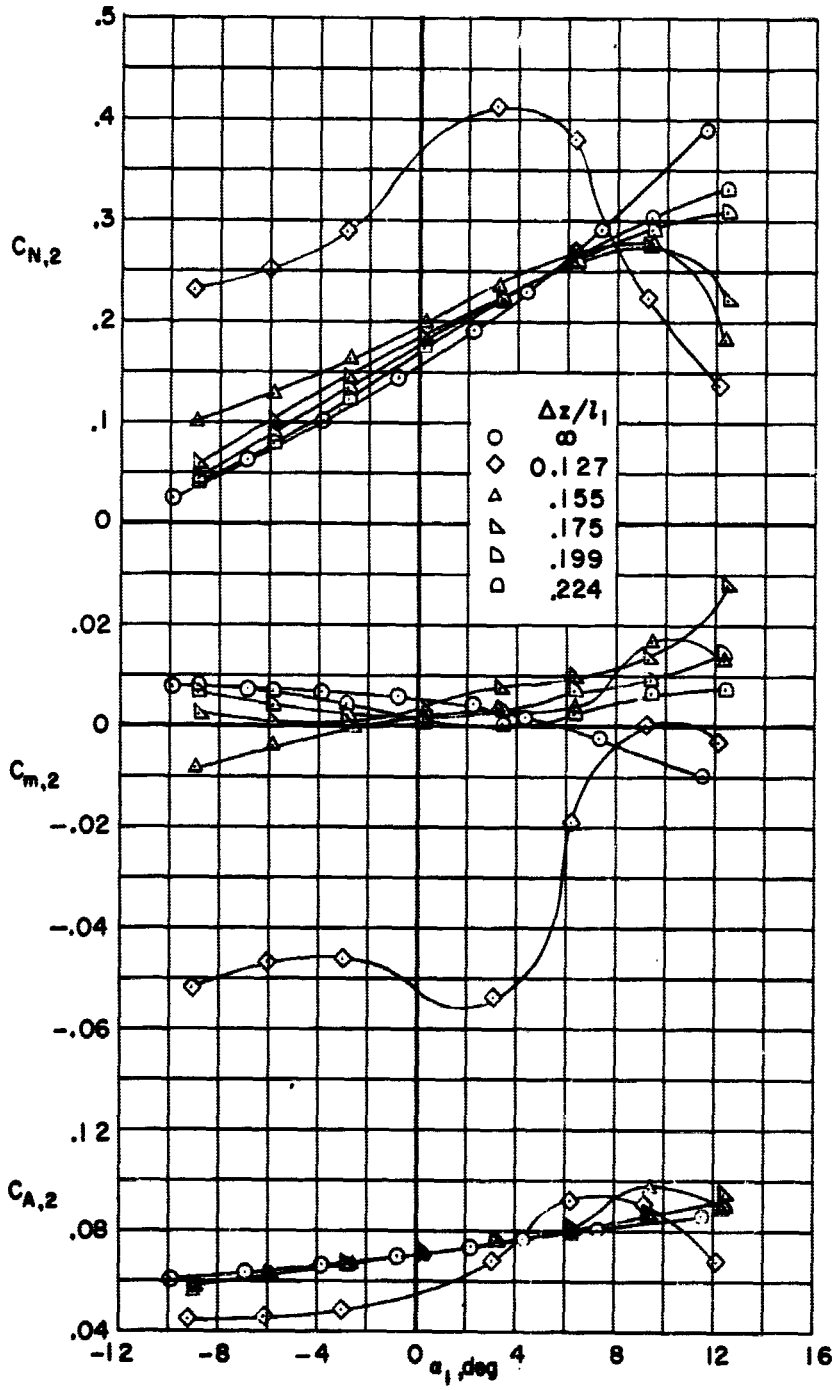

(c) $i = 10^\circ$; $\frac{\Delta x}{l_1} = -0.051$.

Figure 10.- Continued.

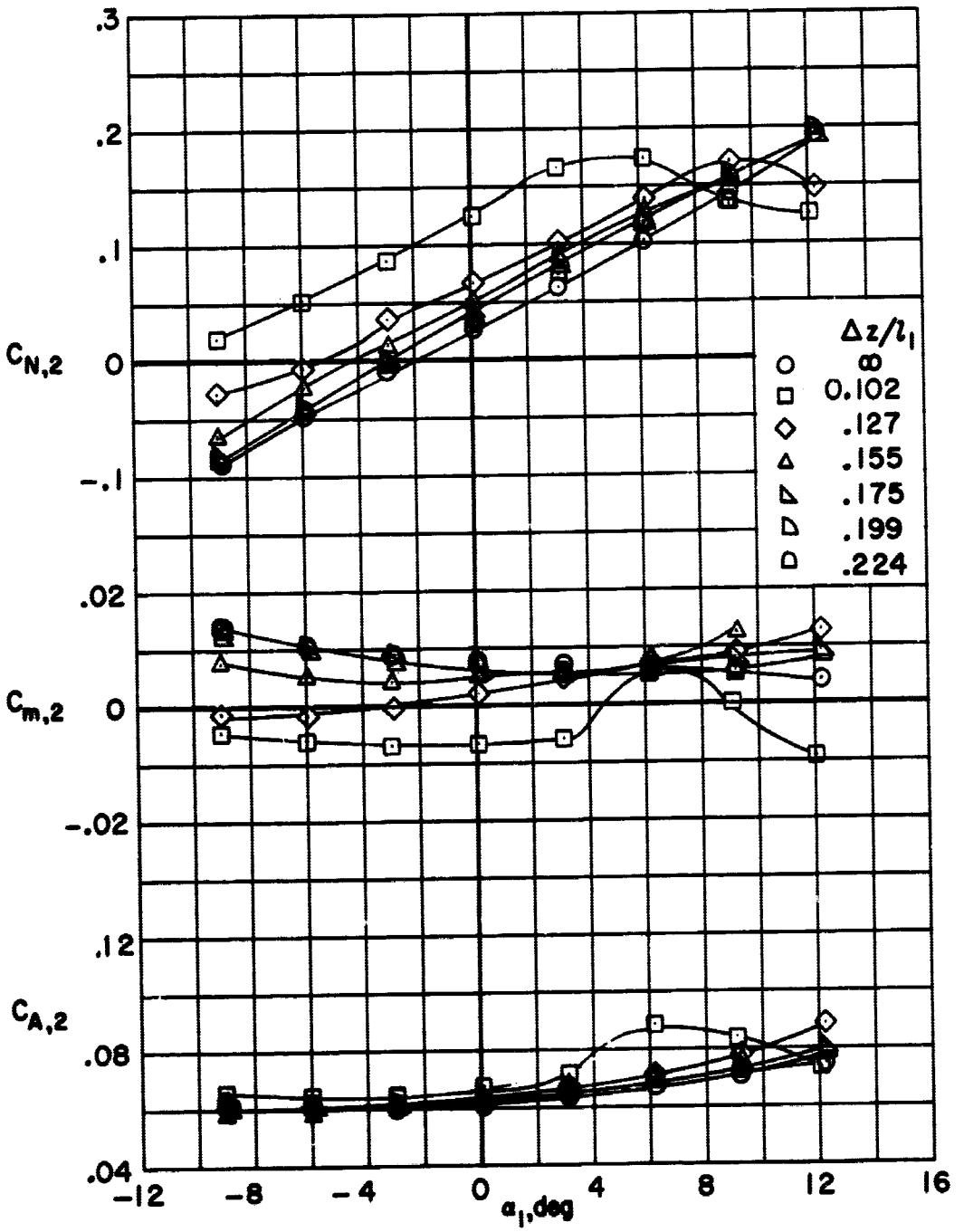

(d) $i = 0^\circ$; $\frac{\Delta x}{l_1} = 0.160$.

Figure 10.- Continued.

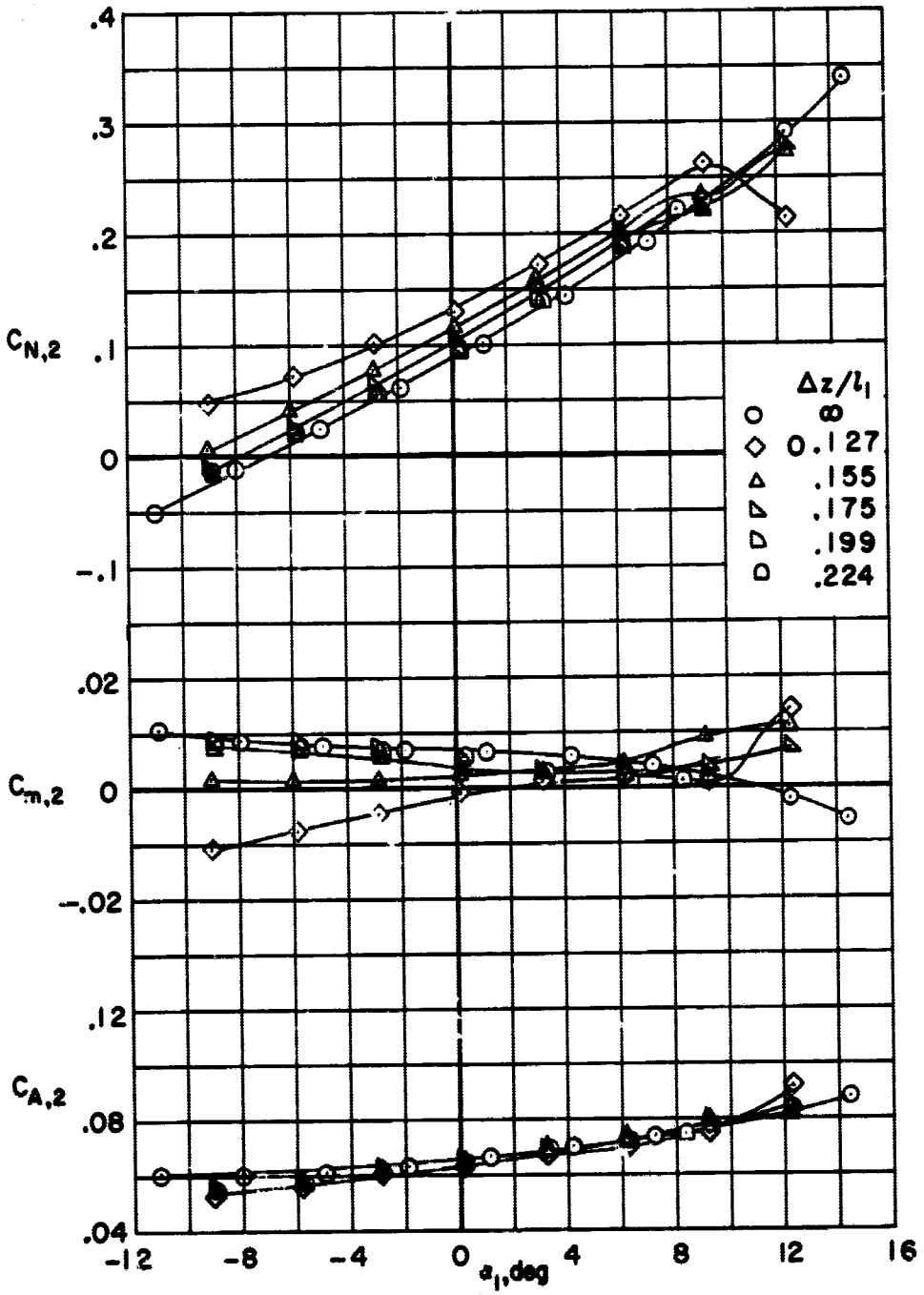

(e) $i = 5°$; $\frac{\Delta x}{l_1} = 0.160$.

Figure 10.- Continued.

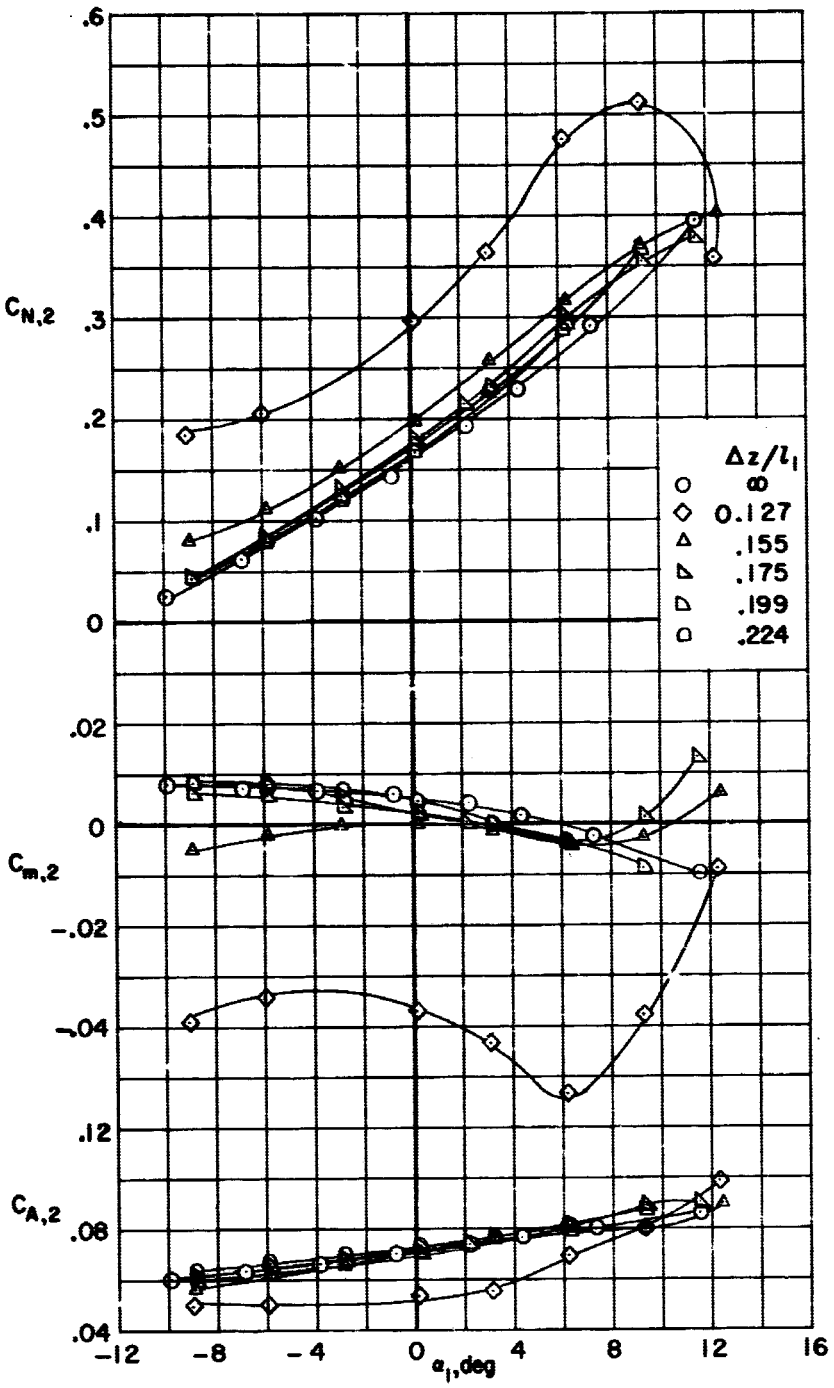

(f) $i = 10^{\circ}$; $\frac{\Delta x}{l_1} = 0.160$.

Figure 10.- Concluded.

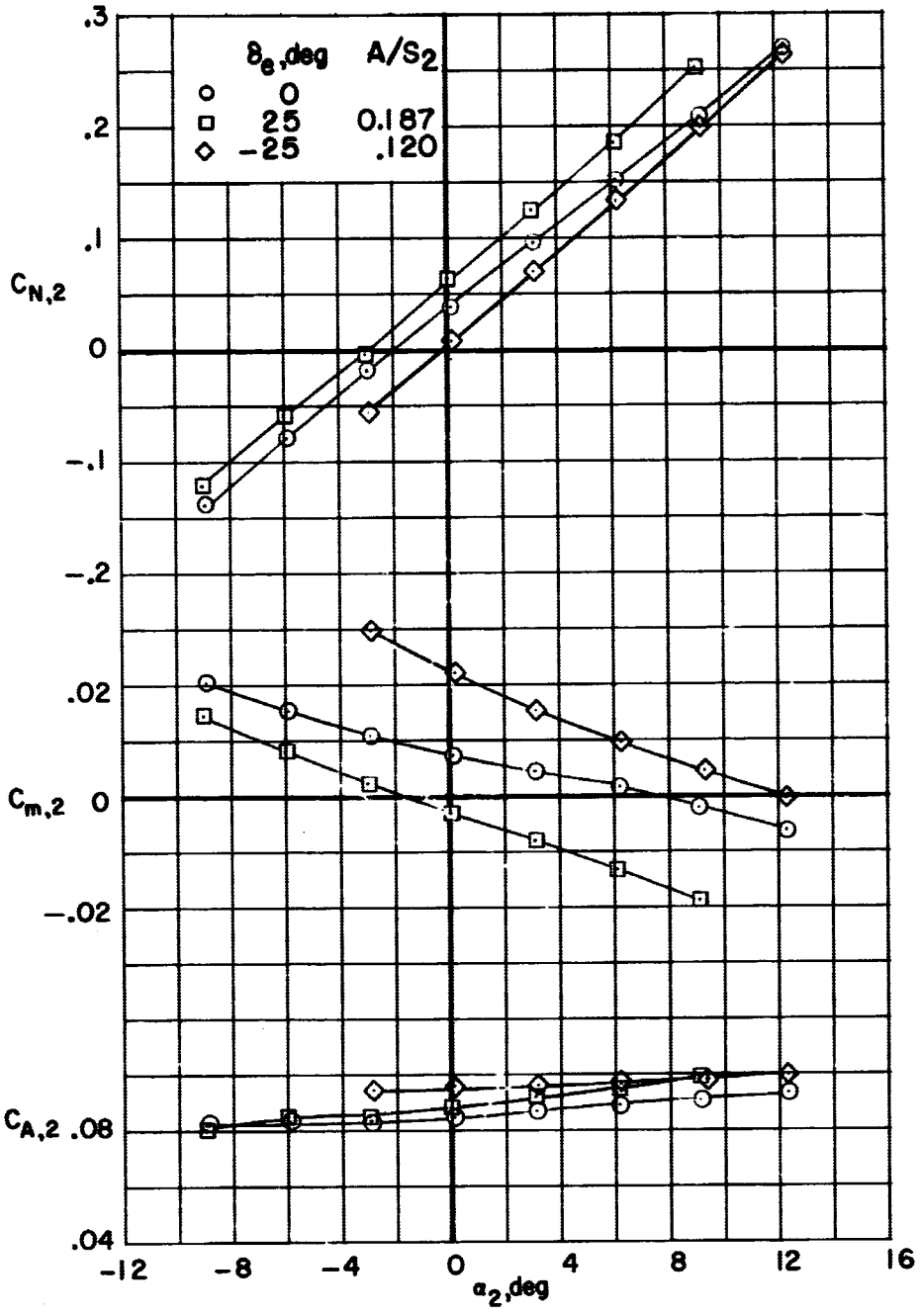

(a) M = 3.

Figure 11.- Control effectiveness of the second stage at interference free conditions.

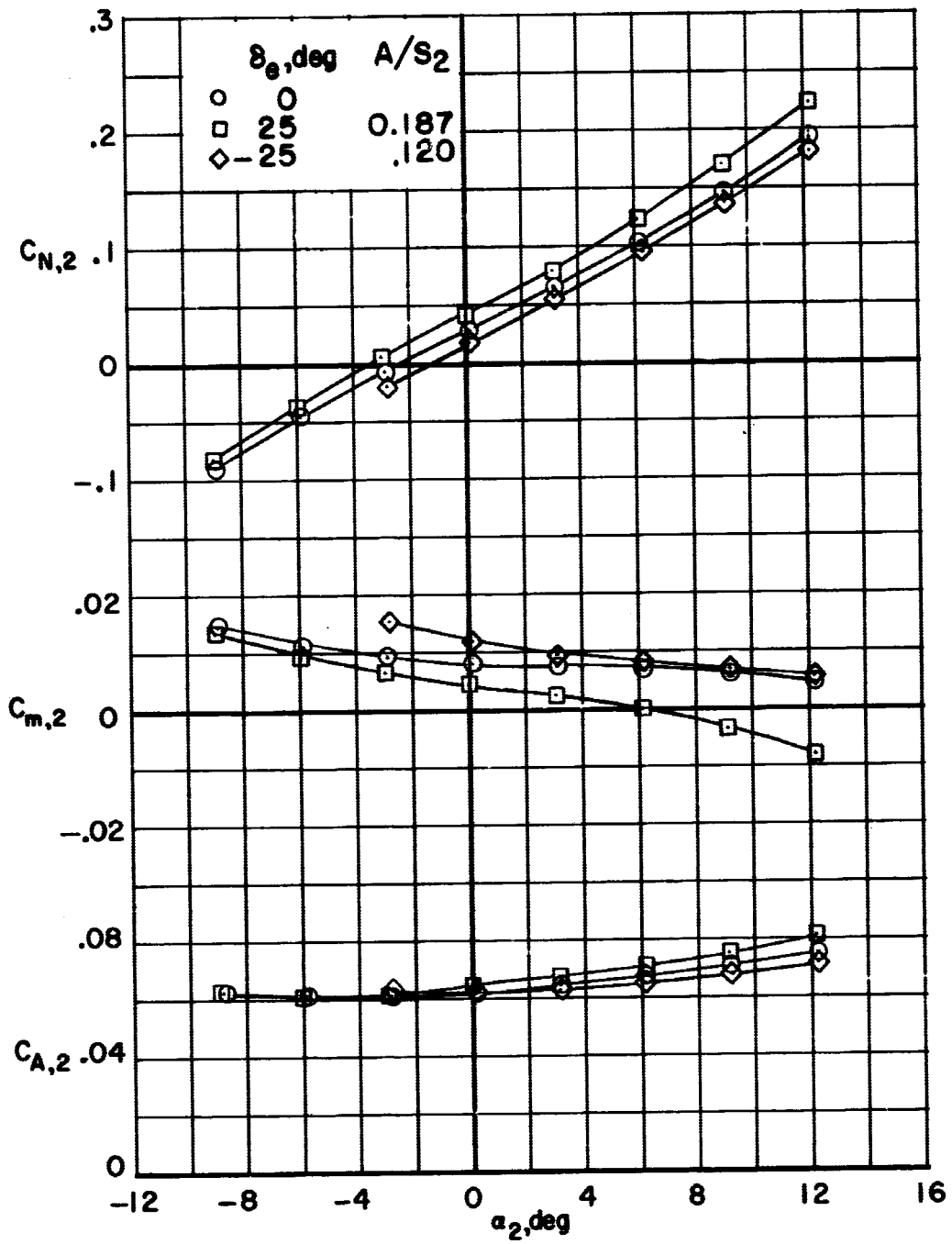

(b) M = 6.

Figure 11.- Concluded.

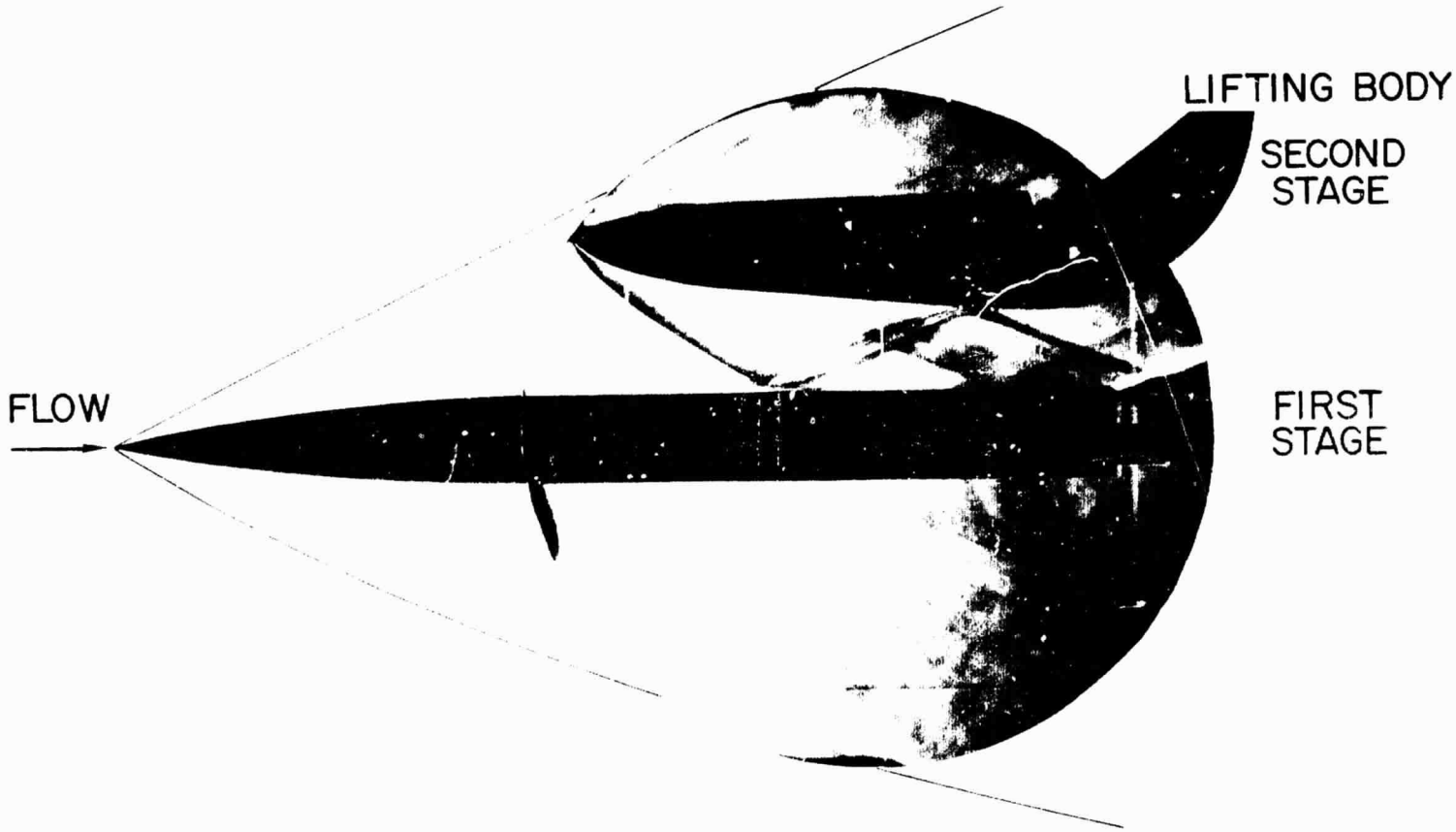

Figure 12.- Schlieren data. $M = 3$; $\alpha_1 = 0^o$; $i = 0^o$; $\frac{\Delta z}{l_1} = 0.199$; $\frac{\Delta x}{l_1} = -0.051$.

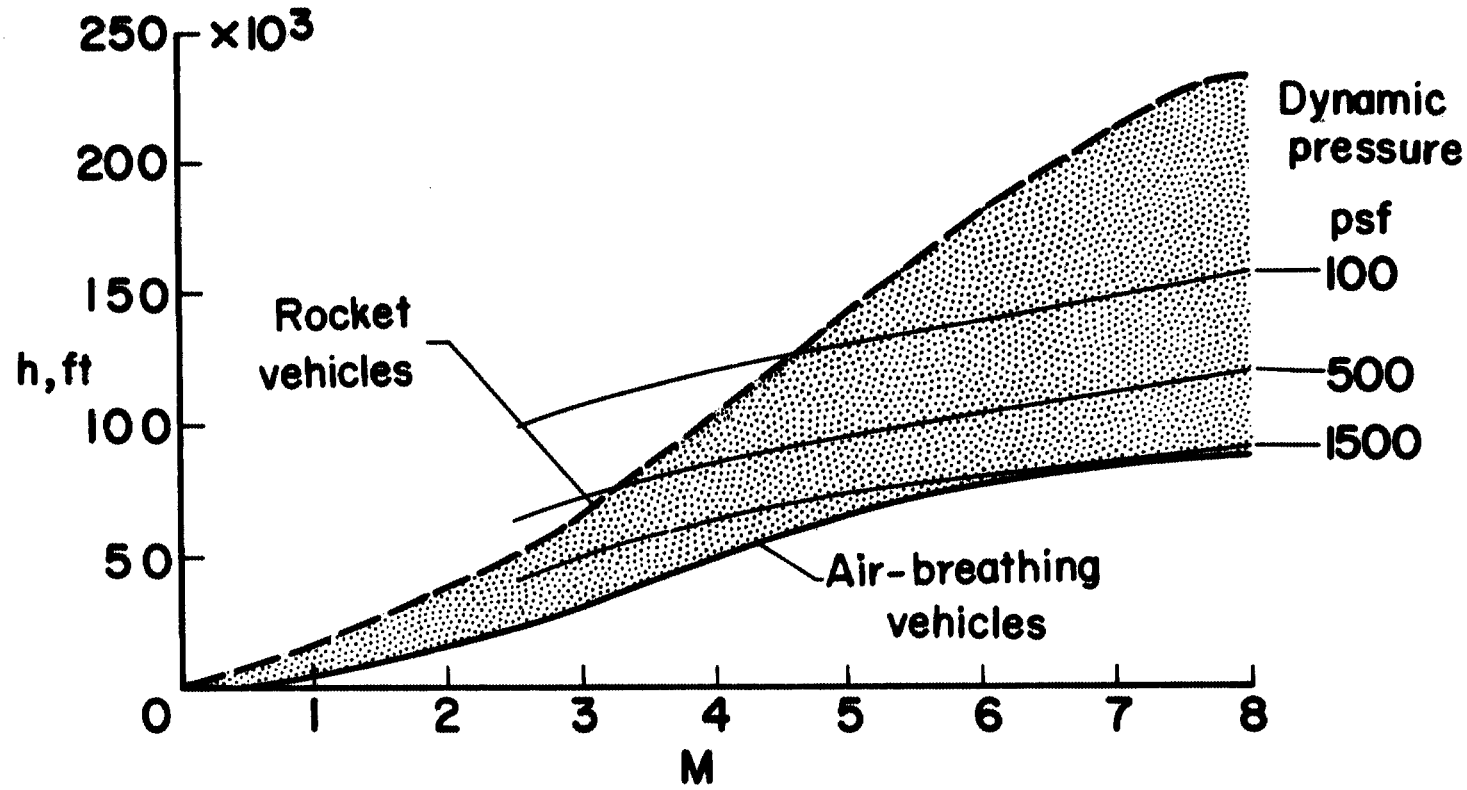

Figure 13.- Staging conditions.

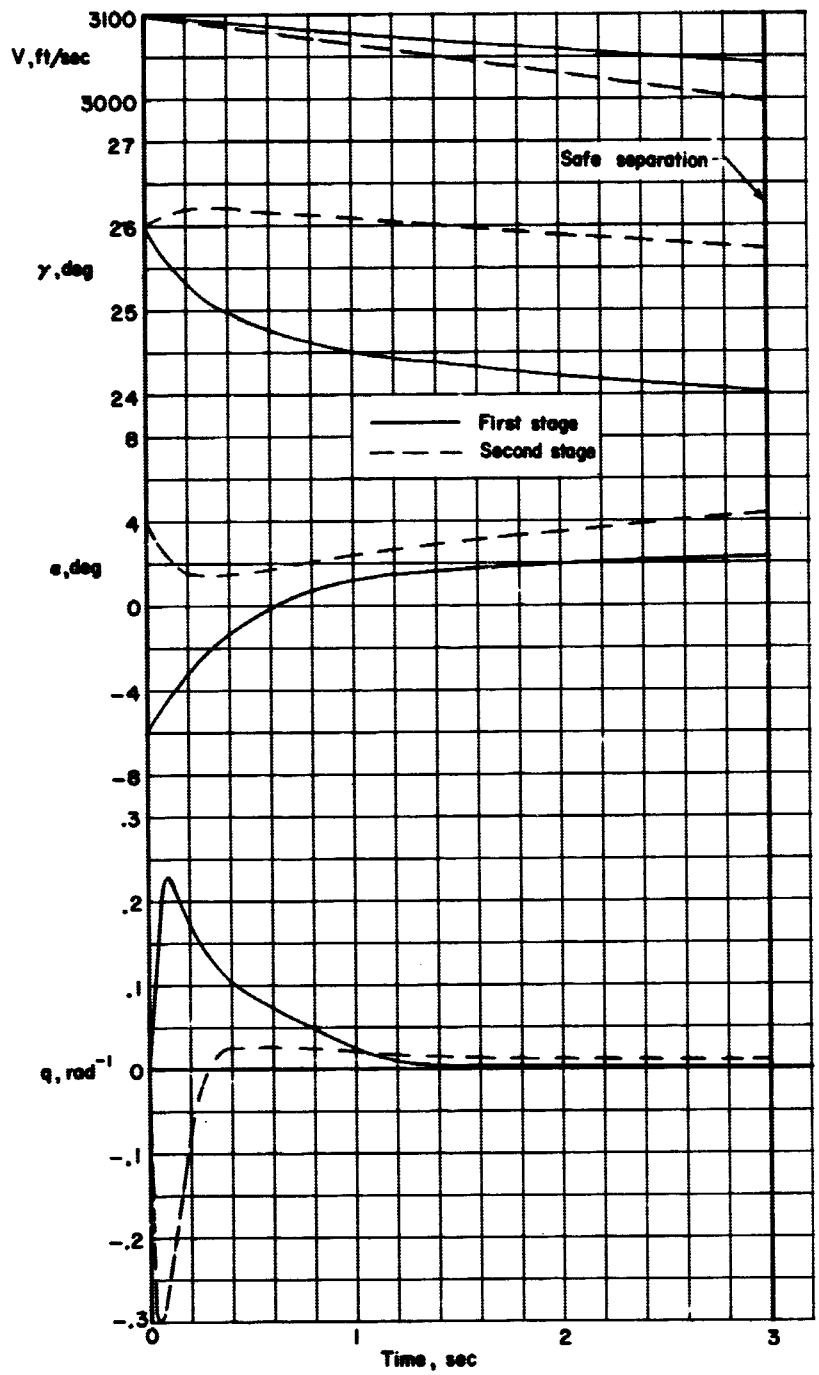

(a) Safe separation case. M = 3; h = 70,000 ft; $(C_{m_q})_1$ = -40 rad^{-1}; $(C_{m_q})_2$ = -20 rad^{-1}.

Figure 14.- Outputs from trajectory program.

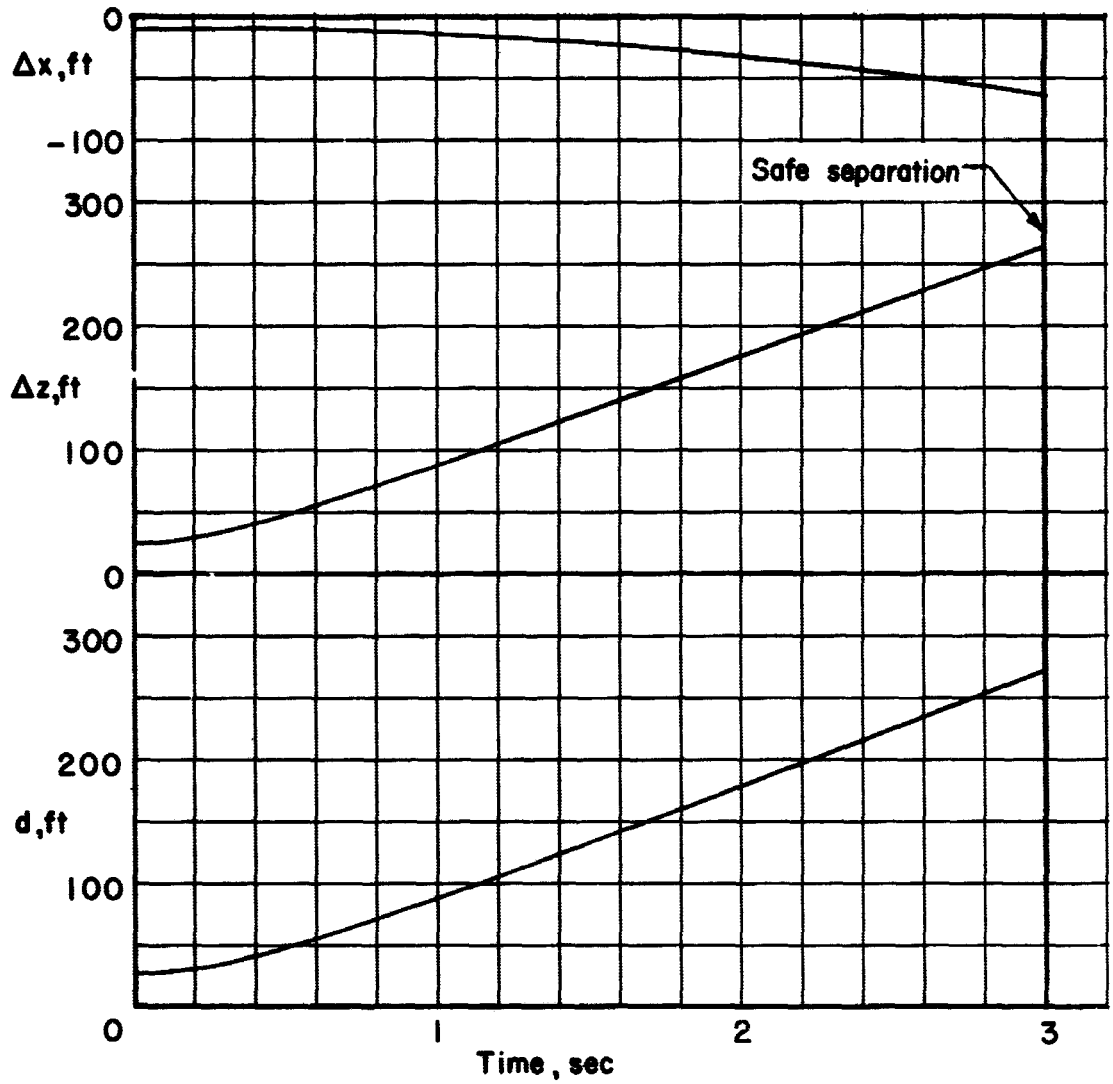

(a) Concluded.

Figure 14.- Continued.

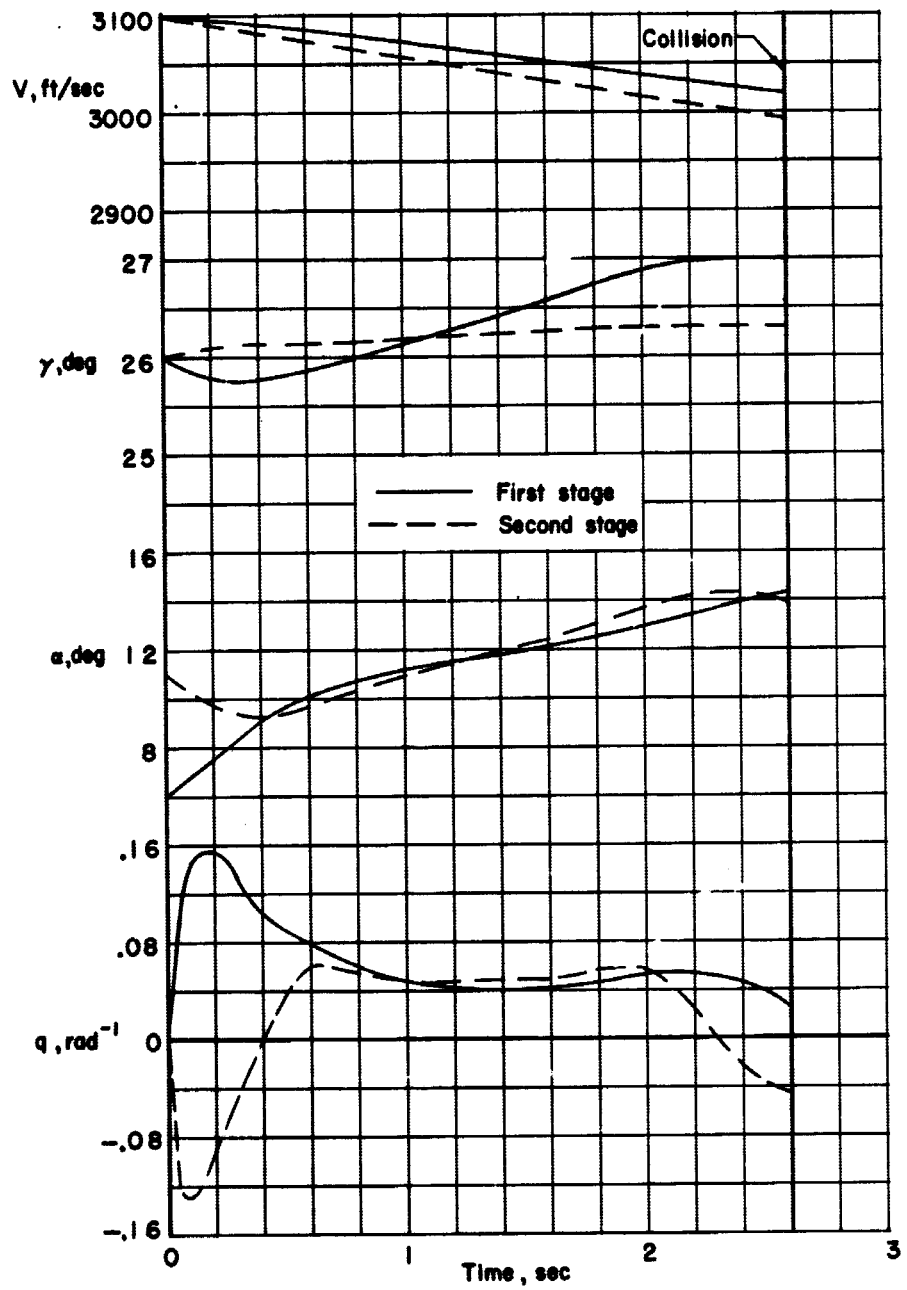

(b) Collision case. $M = 3$; $h = 70{,}000$ ft; $(C_{m_q})_1 = -20$ rad^{-1}; $(C_{m_q})_2 = -10$ rad^{-1}.

Figure 14.- Continued.

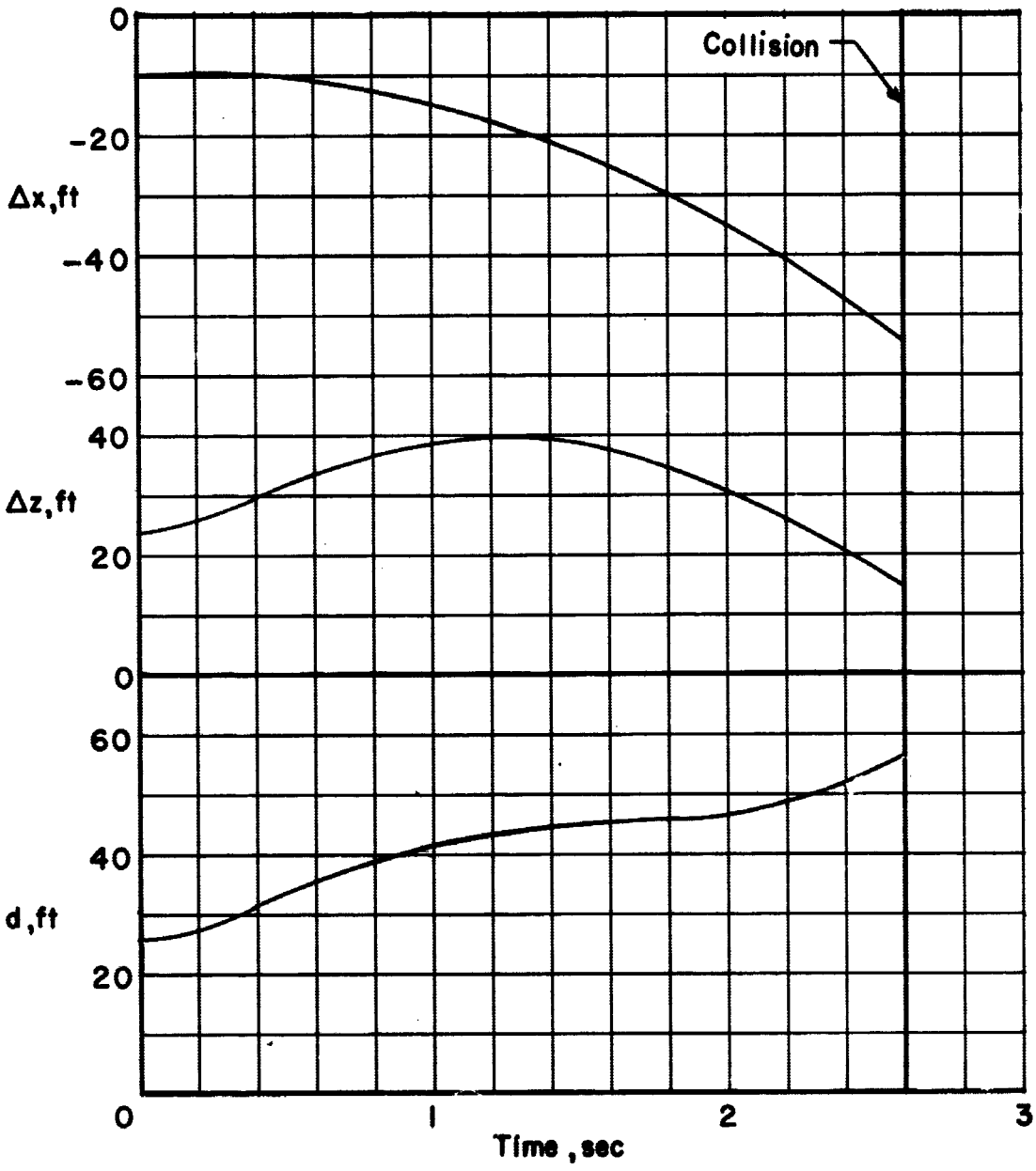

(b) Concluded.

Figure 14.- Concluded.

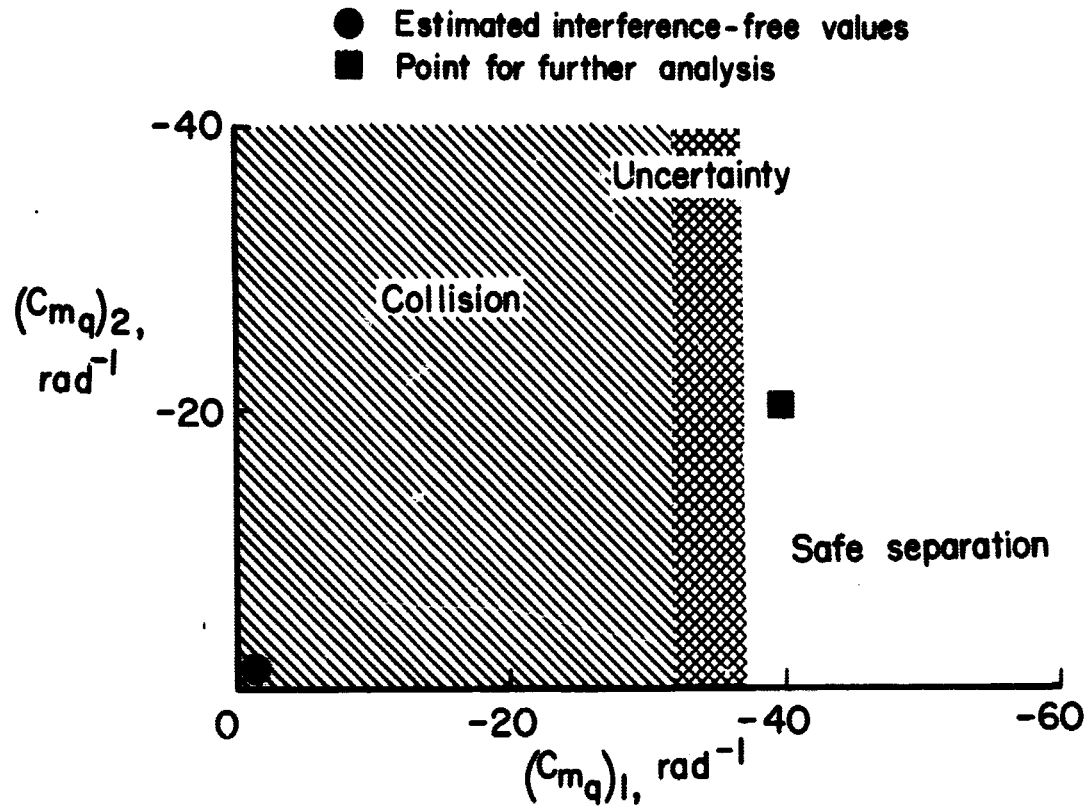

(a) M = 3; h = 70,000 ft; $\alpha_1 = 6^\circ$; $i = 5^\circ$.

Figure 15.- Effect of dynamic derivatives on the separation maneuver.

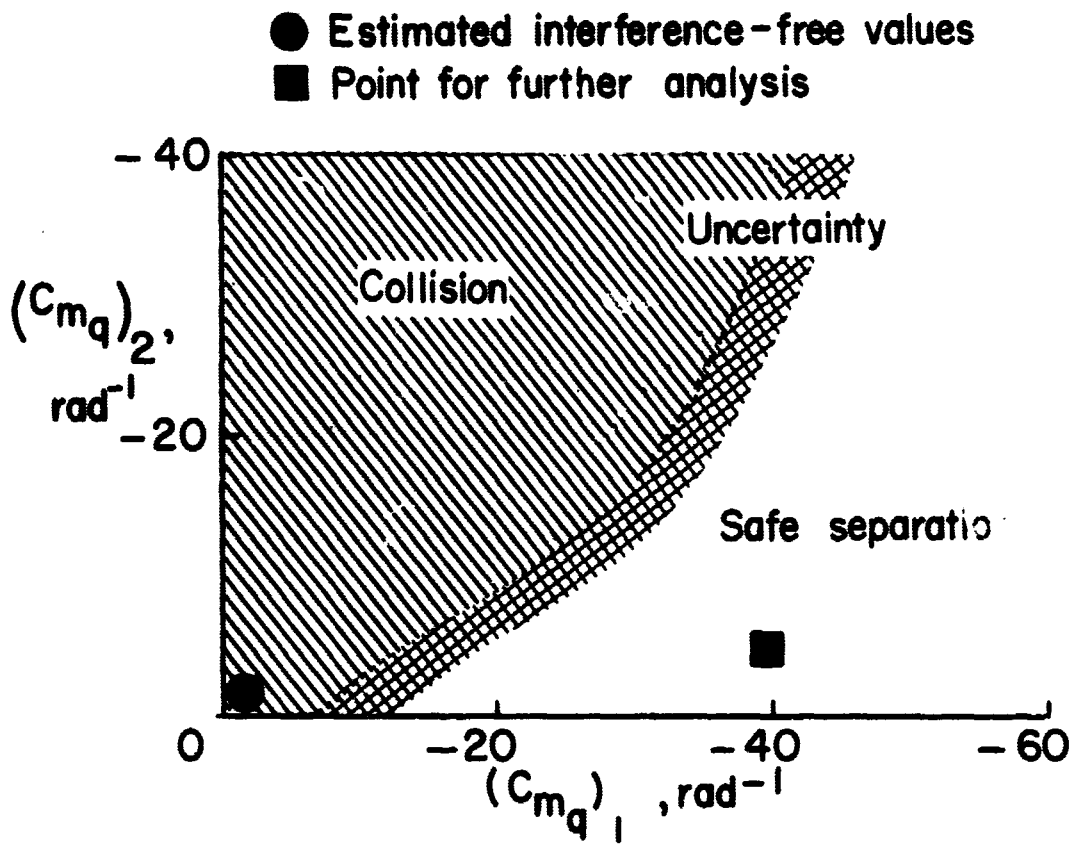

(b) M = 6; h = 110,000 ft; $\alpha_1 = 6^\circ$; $i = 5^\circ$.

Figure 15.- Concluded.

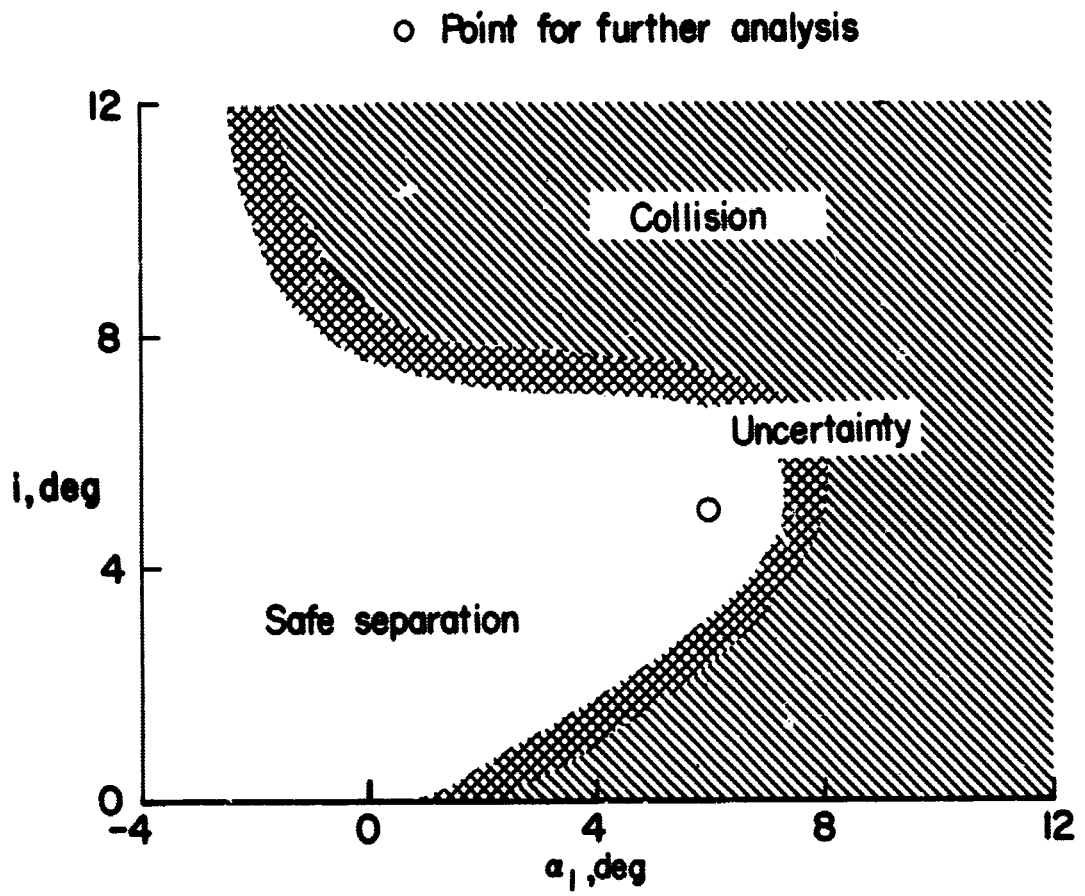

(a) M = 3; h = 70,000 ft; $(C_{m_q})_1$ = -40 rad^{-1}; $(C_{m_q})_2$ = -20 rad^{-1}.

Figure 16.- Effect of initial attitude on the separation maneuver.

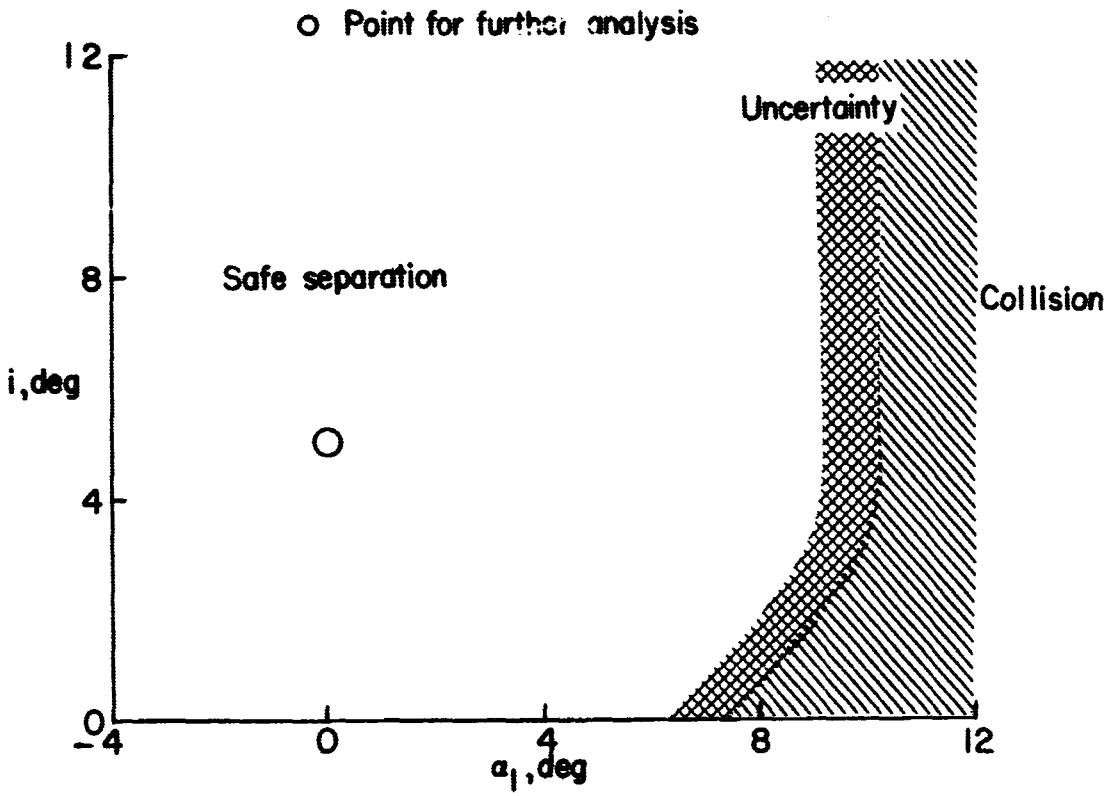

(b) M = 6; h = 110,000 ft; $(C_{m_q})_1 = -40$ rad^{-1}; $(C_{m_q})_2 = -5$ rad^{-1}.

Figure 16.- Concluded.

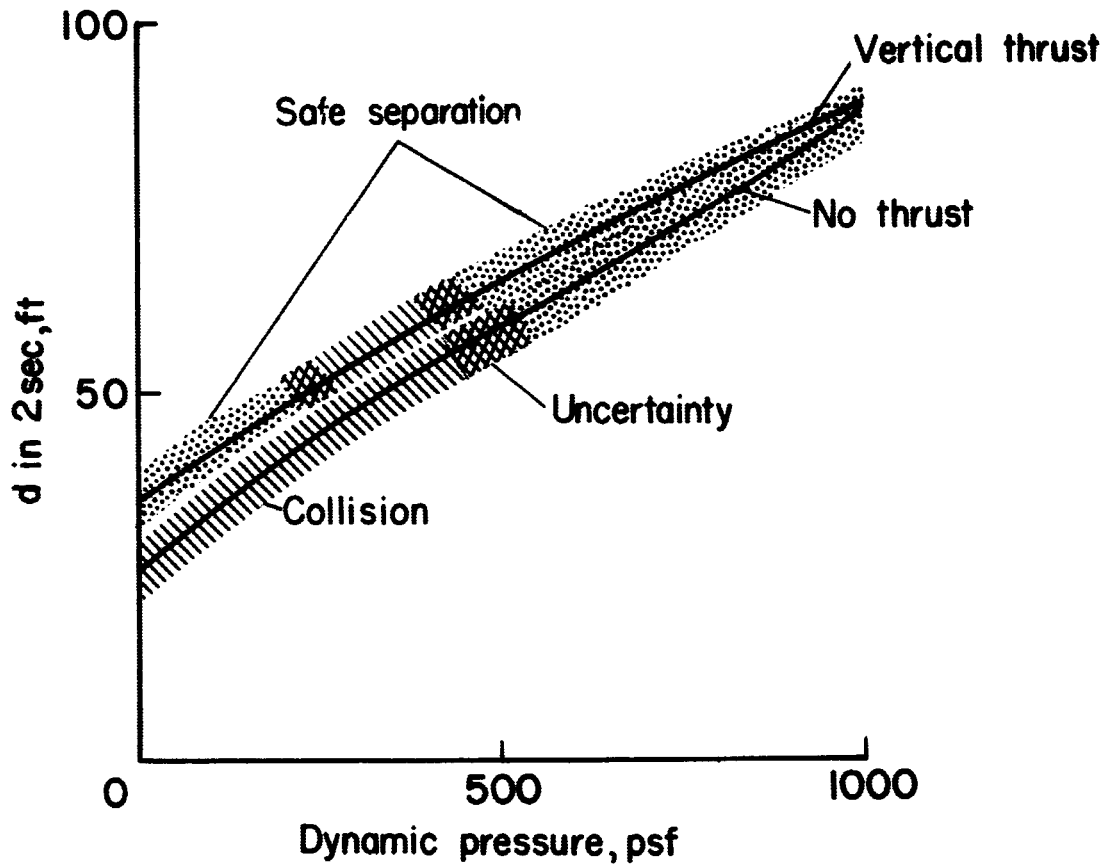

(a) $M = 3$; $\alpha_1 = 6^\circ$; $i = 5^\circ$; $(C_{m_q})_1 = -40$ rad^{-1}; $(C_{m_q})_2 = -20$ rad^{-1}.

Figure 17.- Effect of dynamic pressure on the separation maneuver.

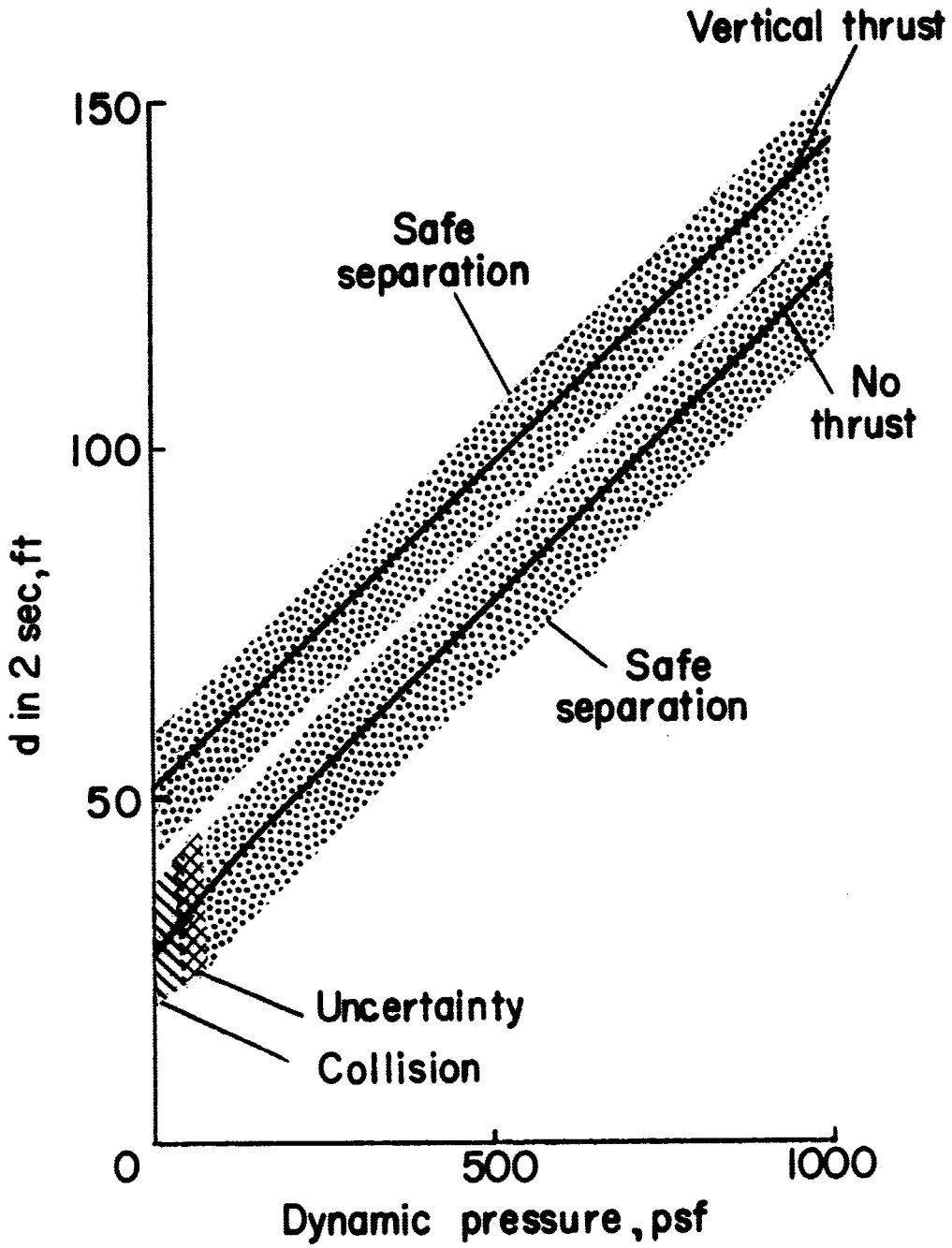

(b) $M = 6$; $\alpha_1 = 0^\circ$; $i = 5^\circ$; $(C_{m_q})_1 = -40$ rad^{-1}; $(C_{m_q})_2 = -5$ rad^{-1}.

Figure 17.- Concluded.